SPRINGER BRIEFS IN
APPLIED SCIENCES AND TECHNOLOGY

Meng Tao

Terawatt Solar Photovoltaics

Roadblocks and Opportunities

Springer

SpringerBriefs in Applied Sciences and Technology

For further volumes:
http://www.springer.com/series/8884

Meng Tao

Terawatt Solar Photovoltaics

Roadblocks and Opportunities

Springer

Meng Tao
Laboratory for Terawatt Photovoltaics
School of Electrical, Computer and Energy Engineering
Arizona State University
Tempe, AZ
USA

ISSN 2191-530X ISSN 2191-5318 (electronic)
ISBN 978-1-4471-5642-0 ISBN 978-1-4471-5643-7 (eBook)
DOI 10.1007/978-1-4471-5643-7
Springer London Heidelberg New York Dordrecht

Library of Congress Control Number: 2014934660

Printed on acid-free paper

Springer is part of Springer Science+Business Media (www.springer.com)

Preface

This book attempts to present a bigger picture of solar photovoltaics. It goes beyond the commonly discussed topics in solar photovoltaics such as solar cell physics, manufacturing, cost, and efficiency. The question it intends to provide some insights into is: what will prevent solar photovoltaics from becoming a noticeable source of energy in the future? In other words, how big a role will solar photovoltaics play in our future energy mix? This is certainly not an easy task, especially for one author. As the reader will find out, the book contains more questions than answers.

The deployment scale of solar photovoltaics has to reach tens to hundreds of peak terawatts for solar electricity to become an important source of energy in our life. The sheer scale required for solar photovoltaics results in many roadblocks and bottlenecks which are unprecedented in other semiconductor technologies. In this book, roadblocks refer to showstoppers which, if not removed, will prevent solar photovoltaics from reaching a terawatt scale. Bottlenecks are difficulties in solar photovoltaics which we prefer to overcome, but can live with if push comes to shove. Efficiency and cost are bottlenecks, and there are more fundamental limitations to terawatt-scale deployment of the current commercial solar cell technologies.

This book reflects the author's view on some of the roadblocks and bottlenecks for terawatt solar photovoltaics. Availability of raw materials, energy input in solar cell manufacturing, storage of solar electricity, and recycling of end-of-life solar modules can all prevent or hinder a tangible impact by solar photovoltaics. After brief discussions on the status, physics, and manufacturing of current solar cell technologies, the book presents analyses, as quantitative as possible, on these roadblocks and bottlenecks to terawatt solar photovoltaics. Thought-provoking ideas to overcoming some of these roadblocks and bottlenecks are discussed.

The author purposely stayed away from many "third-generation concepts" for solar photovoltaics which open up many possibilities for innovative ideas. Instead, the book focuses on demonstrated physics for solar photovoltaics and explores how today's solar photovoltaics can be expanded to a terawatt scale. Predicting the future is always difficult. It becomes practically impossible when there are so many uncertainties at this time for many of the third-generation concepts for solar photovoltaics.

The book is divided into seven chapters. Chapter 1 answers the question: why do we need solar photovoltaics? Chapter 2 reviews the current status of solar photovoltaics including cell technologies and their cost, efficiency, and market. Chapter 3 outlines the physics of solar cells in an across-the-board and less mathematical manner. Chapter 4 focuses on the manufacturing processes, and their costs and energy inputs, for wafer-Si solar cells and modules. Chapter 5 analyzes several roadblocks and bottlenecks for terawatt-scale deployment of current commercial solar cell technologies. Chapter 6 discusses ideas to overcoming some of the roadblocks and bottlenecks in solar cell technologies and in storage of solar electricity. Chapter 7 summarizes the major roadblocks and bottlenecks for potentially terawatt-capable solar cell technologies.

The book is intended for readers with a general interest in energy and a minimal technical background. For this reason, the mathematics required to understand the physics of solar cells is purposely kept to a minimum. Nevertheless, the book involves many disciplines of science and engineering, in particular semiconductor physics, semiconductor processing, and materials chemistry. It is assumed that the reader is technically literate, maybe with a science or engineering bachelor degree, but not necessarily a specialist in the subject of solar photovoltaics. The multidisciplinary nature of solar photovoltaics is illustrated in the book as it requires a broad knowledge base to go through the entire book.

The author got interested in these long-term big-picture issues for solar photovoltaics by accident, which occurred through the establishment of the U.S. Photovoltaic Manufacturing Consortium under SEMATECH in Albany, New York. In summer 2006 when SEMATECH was looking for new research directions, the author made a suggestion for solar photovoltaics. For the next 5 years, the author helped Mr. Dan Holladay, the person in charge of SEMATECH's strategic initiatives at the time, push through the idea. By early 2009, Dan was approaching the U.S. Department of Energy for a nationwide SEMATECH-style industrial consortium for photovoltaic manufacturing technologies. When the initiative became national, it forced the author to think about longer-term, bigger-picture, national, and then global issues in solar photovoltaics. In summer 2009, the author went to Hong Kong University of Science and Technology for a short sabbatical, which provided more free time for the author to ponder through these issues and complete the preliminary analysis on resource limitations to terawatt solar photovoltaics. The first presentation by the author on this analysis was made in January 2010 at the U.S. Photovoltaic Manufacturing Consortium Strategy Workshop in Washington, DC. The first analysis has been revised and expanded multiple times since then, and takes its current form as presented in this book.

There are many people to whom the author is indebted. Mr. Dan Holladay of SEMATECH is the person who got the author into this subject. His determination and dedication to bring industry and academia together for a prosperous U.S. solar cell industry have been a constant inspiration to the author. Prof. Qiming Zhang of the University of Texas at Arlington is a long-time collaborator of the author. His first-principles studies on Earth-abundant solar photovoltaic materials have guided the experiments of the author and his students. Prof. Ellen Stechel

of Arizona State University and the author have had enlightening discussions on solar-powered electrolysis for storage of solar electricity. These discussions led to the idea of metals as solid fuels for a closed, sustainable energy loop. The author would also like to thank the students and postdoctoral fellows who have worked with him over the years. In particular, Dr. Xiaofei Han, who completed his Ph.D. under the author, made several important and original contributions to the research in the author's group on terawatt wafer-Si and post-Si solar photovoltaics. The many graduate and undergraduate students who have taken the author's classes on solar photovoltaics at Arizona State University, the University of Texas at Arlington, and Hong Kong University of Science and Technology have contributed to this book through their intuitive comments and questions. Last but not least are the family members of the author, Lilly, Coby, and Della, for their unconditional love and support. Coby, son of the author, did all the calculations in the first few analyses on resource limitations to terawatt solar photovoltaics between 2009 and 2010, when he was a high-school junior. He now majors in Chemical Engineering in college.

Scottsdale, January 2014 Meng Tao

About the Author

Dr. Meng Tao is currently a Professor in the School of Electrical, Computer, and Energy Engineering at Arizona State University. He received his Ph.D. in Materials Science and Engineering from the University of Illinois at Urbana-Champaign, M.S. in Materials Science and Engineering from Zhejiang University, and B.S. in Metallurgy from Jiangxi Institute of Metallurgy. His career includes 9 years with the State Key Laboratory of Silicon Materials at Zhejiang University and 10 years as a professor of Electrical Engineering at the University of Texas at Arlington. His current research covers a wide range of topics in terawatt solar photovoltaics including Earth-abundant active layer and transparent electrode in thin-film solar cells; substitution of silver electrode in silicon solar cells with Earth-abundant aluminum; energy-efficient electrorefining for solar grade silicon and silicon module recycling; high-temperature silicon power devices for renewable energy systems; and solar-powered electrolysis for solar electricity storage. His research led to the demonstration of a silicon (100) surface free of surface states, enabling record low and record high Schottky barriers on silicon. His research also led to the development of consistent and predictive models for the growth behaviors of many chemical vapor deposition processes. He played a critical role in the establishment of the U.S. Photovoltaic Manufacturing Consortium under SEMATECH in Albany, New York. Since 2006 he has been the lead organizer for the Electrochemical Society symposium series on Photovoltaics for the twenty-first century.

Contents

Chapter 1
The Grand Energy Challenge

The biggest challenge facing mankind in the 21st century is arguably a foundational change we have to undertake to the energy infrastructure we have known for over 200 years. This foundational change is driven by global climate change, which is blamed primarily on emission into the Earth atmosphere of carbon dioxide (CO_2) from combustion of fossil fuels. Coal, oil, and natural gas have been our main sources of energy since the Industrial Revolution. They have to be reduced and supplemented, and sooner or later replaced, by carbon-free energy sources.

The scale of the challenge we are facing is enormous. Figure 1.1 shows a prediction by Hoffert et al. [1] on future global energy demands. The topmost curve indicates that we are currently (2013) consuming energy at an average rate of about 18 terawatts (TW or 10^{12} W) globally. By 2050, the demand is predicted to reach 30 TW and by 2100 46 TW. The different colors in Fig. 1.1 represent contributions from different energy sources over time if we take a business-as-usual approach. The curves labeled "WRE" in Fig. 1.1 are the maximum allowable fossil fuel powers to stabilize the atmospheric CO_2 concentration at 350, 450, 550, 650, and 750 *p*arts *p*er *m*illion (ppm) by atomic ratio, according to a model by Wigley, Richels, and Edmonds [2]. For example, the maximum allowable fossil fuel power for 450 ppm atmospheric CO_2 concentration is roughly 8 TW in 2050, or carbon-free energy sources have to provide 22 TW to meet the total demand of 30 TW.

As shown in Fig. 1.2, the atmospheric CO_2 concentration was stable at about 280 ppm for thousands of years before the Industrial Revolution [3], which started around 1800. In May 2013, it surpassed 400 ppm according to the U.S. National Oceanic and Atmospheric Administration [4]. The rapid rise in atmospheric CO_2 concentration is shifting the delicate energy balance of the Earth between incoming solar radiation and outgoing thermal radiation. One of the CO_2 absorption peaks in the infrared range is around 15 μm. It coincides with the peak of the thermal radiation spectrum of the Earth [5], thus trapping heat in the atmosphere. The result is the rising surface temperature of the Earth, as shown in Fig. 1.3 [6]. The mean surface temperature of the Earth has risen almost 1 °C between 1880 and 2012, with an increased pace of about 0.15 °C/decade in the last 30 years.

M. Tao, *Terawatt Solar Photovoltaics*, SpringerBriefs in Applied Sciences and Technology, DOI: 10.1007/978-1-4471-5643-7_1, © The Author(s) 2014

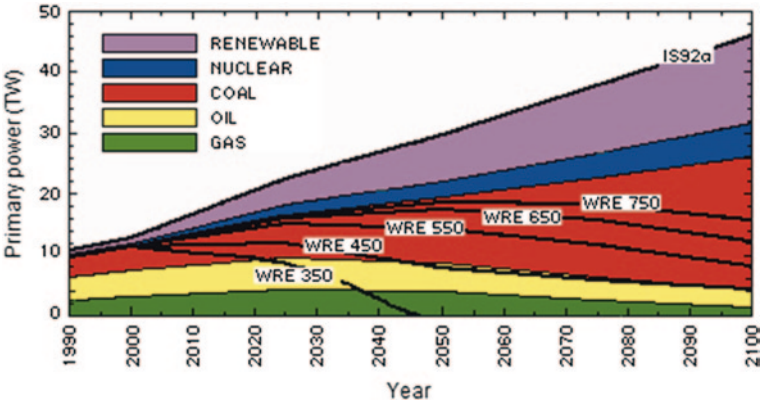

Fig. 1.1 Predicted global energy demands through 2100 [1]. Reprinted with permission of Macmillan Publishers Ltd. The colors represent contributions from different energy sources in a business-as-usual scenario. The curves labeled "WRE" are the maximum allowable fossil fuel powers for target atmospheric CO_2 concentrations in ppm

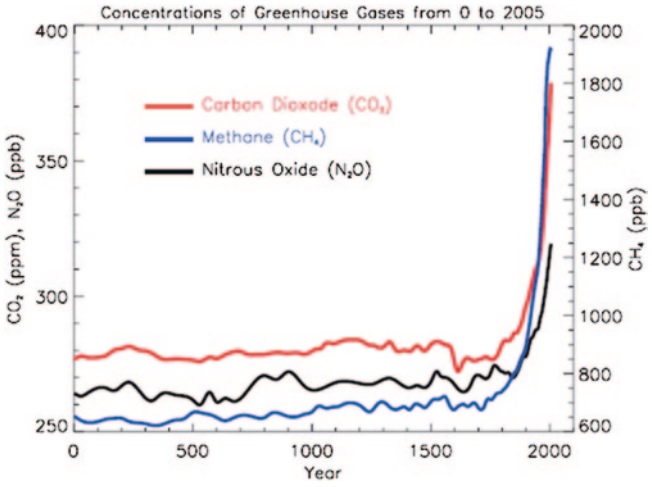

Fig. 1.2 Atmospheric CO_2 concentration over the last 2,000 years [3]. Reprinted with permission of Intergovernmental Panel on Climate Change. Two other greenhouse gases are also included. In May 2013, the atmospheric CO_2 concentration surpassed 400 ppm according to the U.S. National Oceanic and Atmospheric Administration [4]

With the huge inertia of the energy infrastructure, it is probably too late to target 450 ppm for the stabilized atmospheric CO_2 concentration. If we target 750 ppm as the maximum allowable CO_2 concentration in the atmosphere, Fig. 1.1 suggests that carbon-free energy sources have to provide about 11 TW out of the 30 TW total demand by 2050, or about 37 % of the total demand. The capacities

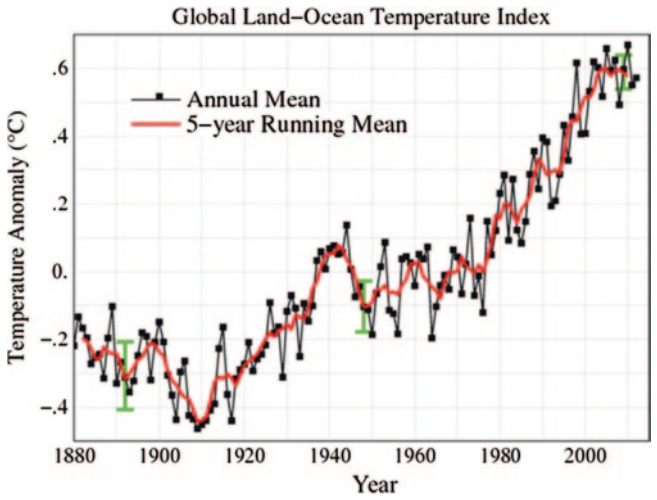

Fig. 1.3 Global mean surface temperature anomalies, from 1880 to 2012, relative to the base period of 1951–1980 [6]. The surface temperature has risen almost 1 °C between 1880 and 2012, with an increased pace of about 0.15 °C/decade in the last 30 years

of today's nuclear or coal-fired power plants are typically around 1 gigawatt (GW or 10^9 W) each. If we were to build carbon-free power plants of 1 GW capacity, we would have to build one power plant each day for the next 37 years in order to accumulate a 11 TW capacity of carbon-free energy generation by 2050. If the price tag for these carbon-free power plants could be reduced to a level similar to that of nuclear power plants, which is roughly \$5/W, a 11 TW capacity would require an investment of about \$55 trillion. The current price tag for solar photovoltaics is, on a time-averaged basis, \$15–30/W depending on the size of the installed system and also the local solar intensity. A 11 TW capacity of solar photovoltaics at the current price would require an investment of \$165–330 trillion. If we look further out to 2100 and our target is still 750 ppm atmospheric CO_2, an additional capacity of 17 TW carbon-free energy generation will have to be added between 2050 and 2100. We would have to build one 1 GW carbon-free power plant each day throughout the end of this century, with a whopping price tag of \$150 trillion at \$5/W, or \$450–900 trillion at \$15–30/W.

These back-of-envelope calculations examine only one aspect of the new energy infrastructure, i.e. energy generation. The new energy infrastructure includes not only generation, but also storage, distribution, and usage. Further complicating the matter is the economic, geopolitical, societal, behavioral, and environmental impacts of a changing energy infrastructure, as cheap and reliable energy has been at the foundation of our modern society. It is impossible for one author to provide a comprehensive analysis of the new energy infrastructure. The intent of the above discussion is to illustrate how daunting our tasks are in our endeavor to end our addiction to fossil fuels and leave behind an inhabitable planet for our children.

1.1 Solar Energy

Before we start building carbon-free power plants, we have to figure out where carbon-free energy sources are. With global energy demands at tens of terawatts, we are limited to only one or possibly two options for carbon-free energy, i.e. solar energy and nuclear fusion. Our planet receives about 1.2×10^{17} W, or 1.2×10^{5} TW, of solar power, which is roughly 7,000 times more than our current consumption rate of energy. The amount of solar energy the Earth receives in 1 h is more than the total energy the whole planet consumes in an entire year. Solar energy alone has the capacity to meet all the planet's energy demands for the foreseeable future. With the exception of nuclear fusion, no other carbon-free energy sources currently known to us have such a capacity, so they can only serve as auxiliary energy sources in our future energy mix. A more detailed analysis on carbon-free energy sources and their capacities by Lewis can be found in reference [7]. Besides solar energy and nuclear fusion, other carbon-free energy sources include wind, hydropower, biomass, ocean currents, tides and waves, geothermal energy, and nuclear fission. It is interesting that many carbon-free energy sources originate from solar energy, except perhaps ocean tides, geothermal energy, and nuclear energy. The land requirement for solar energy utilization is minimal. Covering 1 % of the Earth surface with 10 % efficient solar energy conversion devices would generate about 120 TW of energy [8], much more than the predicted energy demands of the planet through 2100.

Figure 1.4 is the reference solar spectrum at air mass 1.5 (AM 1.5) [9], i.e. when the Sun is about 48° from the zenith. The spectrum is global, which includes both direct-beam and diffuse sunlight, and covers the spectral range of 300–2,500 nm. The total solar intensity at AM 1.5 is roughly 1,000 W/m^2. Solar cell efficiencies are often measured under this spectrum. The data in the figure is converted to photon flux, i.e. the number of photons per unit area per unit time and per unit wavelength. This is more useful in solar photovoltaics than spectral irradiance in watts per unit area per unit wavelength, as it is the number of photons, not necessarily the wattage, which determines the number of charge carriers generated by sunlight.

While nuclear fusion has yet to be demonstrated as a controllable and reliable method to generate energy at this time, several technologies for solar energy utilization are being commercially deployed. A report by the U.S. Department of Energy entitled "Basic Research Needs for Solar Energy Utilization" provides an introduction to various technologies which convert solar energy, in the form of optical energy, into other more readily-exploitable forms of energy [8]. Generally speaking, there are three conversation processes of interest, which transform solar energy directly into another form of energy:

1. Solar-to-electrical conversion;
2. Solar-to-chemical conversion; and
3. Solar-to-thermal conversion.

The two most popular forms of energy in our life today are electricity and gasoline. Solar-to-electrical and solar-to-chemical conversions are intended to provide

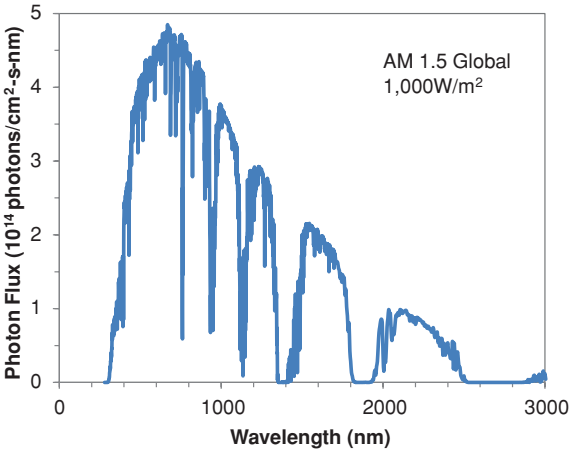

Fig. 1.4 Reference solar spectrum at AM 1.5 [9], i.e. when the Sun is about 48° from the zenith. The spectrum includes both direct-beam and diffuse sunlight, with a total power of roughly 1,000 W/m^2. The data is presented in photon flux, as the number of photons determines the number of charge carriers generated by sunlight

substitutes for fossil fuels and fossil-fuel generated electricity. Although less popular, thermal energy often appears in the form of hot air or hot water for, e.g. centralized heating in cities.

Compared to controlled energy generation such as nuclear and coal-fired power plants, solar energy is a less predictable energy source. The relative position of the Sun with respect to any location on the Earth can be fairly accurately predicted for any given moment, which determines the maximum possible solar intensity at that time for that location. The effects of weather and human activities such as pollution are more difficult to predict. Moreover, our energy demands often mismatch with the production cycle of solar energy, which typically peaks around noon. Once solar energy is converted into electrical, chemical, or thermal energy, storage and distribution are often required to deliver the energy for later demands or to different locations.

Solar-to-electrical conversion employs photovoltaic devices, including photoelectrochemical devices, to generate electricity from sunlight. This book will present an analysis on major roadblocks and several bottlenecks to terawatt-scale deployment of solar photovoltaics. In particular, it will present a quantitative analysis on natural resource limitations to terawatt solar photovoltaics. Solar-to-chemical conversion transforms solar energy and stores it in chemical bonds. The solar fuels produced can be transported in ways similar to gasoline distribution. In order words, solar-to-chemical conversion addresses energy generation and storage in one step, and thus has a perceived advantage over the other two conversion processes. One example of solar-to-chemical conversion is solar water splitting, where solar energy dissociates water molecules (H_2O) into hydrogen (H_2) as a fuel and oxygen (O_2) as a byproduct. Another possibility is solar-driven photochemical reduction of CO_2 to carbon monoxide (CO) which can be used as a feedstock for synthetic fuels. A popular solar-to-thermal conversion technology today is the rooftop solar water heaters which provide hot water of less than 100 °C to millions of families.

More complicated technologies that integrate two conversion processes into one system are also being developed. This is more obvious in concentrated solar power systems, which use mirrors or lenses to focus a large area of sunlight onto a small area. At the focal point of such a system, a liquid is heated up to 1,000 °C. The steam produced can power a conventional turbine for electricity generation. The high temperature can also, in principle, trigger thermochemical reduction of CO_2 to CO for synthetic fuels. Concentrated solar power systems require tracking devices to follow the Sun, and they have to be installed in a dry climate without obstruction to direct-beam sunlight.

1.2 Scope of This Book

The technologies discussed above for solar energy utilization are at various stages of maturity. Commercially the most successful technology today is probably solar water heaters. Although they are technically mature and economically competitive, they are incapable of producing electricity or fuels. Solar photovoltaic modules and concentrated solar power systems are being commercially deployed at gigawatt scales, even though they are still costly compared to fossil fuels or nuclear fission. Solar-to-chemical conversion and photoelectrochemical devices are largely in various stages of laboratory development. This book will focus on a technology which is ready for large-scale commercial deployment, i.e. solar photovoltaics. We will employ the term *solar photovoltaic cells*, or more simply *solar cells*, to reflect the fact that this technology utilizes the photovoltaic effect to convert sunlight into electricity.

There is little doubt in the author's mind that, by the end of this century, sunlight will be a main source of energy in our life. However, how big a role will photovoltaics play in this new energy infrastructure? Besides cost and efficiency, are there other roadblocks and bottlenecks which can prevent solar photovoltaics from reaching its full potential? As implied in Fig. 1.1, solar photovoltaics will have to reach a scale of tens of peak terawatts, or it will not make a noticeable contribution to our future energy mix. There are multiple other roadblocks which, if not removed, will prevent terawatt-scale deployment of the current commercial solar cell technologies. In addition, there are also many bottlenecks which hinder the deployment of the current commercial solar cell technologies.

In this book, we will discuss some of these roadblocks and bottlenecks in more details. We will analyze natural resource limitations to terawatt solar photovoltaics due to limited availability of raw materials and electricity. We will also explain roadblocks in terawatt-scale storage of solar electricity and recycling of terawatt-scale end-of-life solar modules. A discussion on some of the required and desired properties for a terawatt-scale solar cell technology will be presented, which provides guidelines for our efforts to develop a low-cost, high-efficiency, and terawatt-capable solar cell technology. Several strategic research directions will be suggested for the ultimate goal of terawatt solar photovoltaics, which cover terawatt wafer-silicon (Si)

solar photovoltaics, terawatt thin-film Si solar photovoltaics, and terawatt thin-film post-Si solar photovoltaics. Finally a sustainable energy loop for solar electricity storage and distribution will be proposed, which is capable of delivering solar energy on demand.

The analysis in this book may look grim for the future of solar photovoltaics at first glance. The intent of the author is not to scare readers, but to quantify the challenge, no matter how seemingly daunting it is. More importantly, it is the author's hope that we will realize how great an opportunity this grand challenge presents to scientists and engineers. This is an once-in-a-lifetime opportunity for all of us who want our research to make a long-lasting impact. It is also our responsibility to our civilization, our planet, and our children.

References

1. Hoffert MI, Caldeira K, Jain AK, Haites EF, Harvey LDD, Potter SD, Schlesinger ME, Schneider SH, Watts RG, Wigley TML, Wuebbles DJ (1998) Energy implications of future stabilization of atmospheric CO_2 content. Nature 395:881–884
2. Wigley TML, Richels R, Edmonds JA (1996) Economic and environmental choices in the stabilization of atmospheric CO_2 concentration. Nature 379:240–243
3. Intergovernmental Panel on Climate Change (2007) Climate change 2007—the physical science basis. Cambridge University Press, Cambridge
4. U.S. National Oceanic and Atmospheric Administration, Trends in atmospheric carbon dioxide. Available at http://www.esrl.noaa.gov/gmd/ccgg/trends/
5. Mitchell JFB (1989) The 'greenhouse' effect and climate change. Rev Geophys 27:115–139
6. U.S. National Aeronautics and Space Administration, GISS surface temperature analysis. Available at http://data.giss.nasa.gov/gistemp/
7. Lewis NS (2007) Powering the planet. MRS Bull 32:808–820
8. U.S. Department of Energy (2005) Basic research needs for solar energy utilization. Available at http://science.energy.gov/~/media/bes/pdf/reports/files/seu_rpt.pdf
9. U.S. National Renewable Energy Laboratory, Reference solar spectral irradiance—air mass 1.5. Available at http://rredc.nrel.gov/solar/spectra/am1.5/

Chapter 2
Status of Solar Photovoltaics

Before our discussions on the technical aspects of solar photovoltaics, we will first review the status of solar photovoltaics. This chapter begins with a review on current solar cell technologies and their efficiencies. It is followed by a discussion on solar cell cost, a well-known barrier to large-scale deployment of solar photovoltaics. The third section will discuss the market for solar photovoltaics, including annual and cumulative installations, market shares by different cell technologies, and their historical trends. The chapter ends on a high note that both the potential and gap in solar energy utilization by photovoltaics are enormous.

2.1 The Efficiency

Photovoltaics stands for *light-induced voltage*. It was discovered by French physicist Becquerel in 1839 [1]. His experiment involved an electrochemical cell with a silver chloride (AgCl) electrode and a platinum (Pt) electrode in an acidic solution. When light was shed on the AgCl electrode, a voltage was observed between the two electrodes. American inventor Fritts [2] demonstrated an all solid-state photovoltaic device in 1883. He deposited an extremely thin layer of gold (Au) on semiconductor selenium (Se), so it was transparent to incident light. The energy conversion efficiency of the device was less than 1 %. Modern solar cells, in which a semiconductor p-n junction is employed, were conceived by Ohl [3] of Bell Laboratories in 1946. Chapin et al. [4] of Bell Laboratories demonstrated the first modern Si solar cell in 1954. Their cell employed a monocrystalline-Si wafer with a 2.5-μm p-type layer formed over the n-type wafer, resulting in an efficiency of about 6 %. Although modern Si solar cells have achieved 25 % efficiency [5], they all resemble the first Si cell in several key aspects, i.e. they all employ a Si wafer, either monocrystalline or multicrystalline, for sunlight absorption and a p-n junction for charge separation.

Steady progress has been made since the first wafer-Si solar cell in 1954. Figure 2.1 displays the evolution of best laboratory efficiencies for various solar cell technologies

M. Tao, *Terawatt Solar Photovoltaics*, SpringerBriefs in Applied Sciences and Technology, DOI: 10.1007/978-1-4471-5643-7_2, © The Author(s) 2014

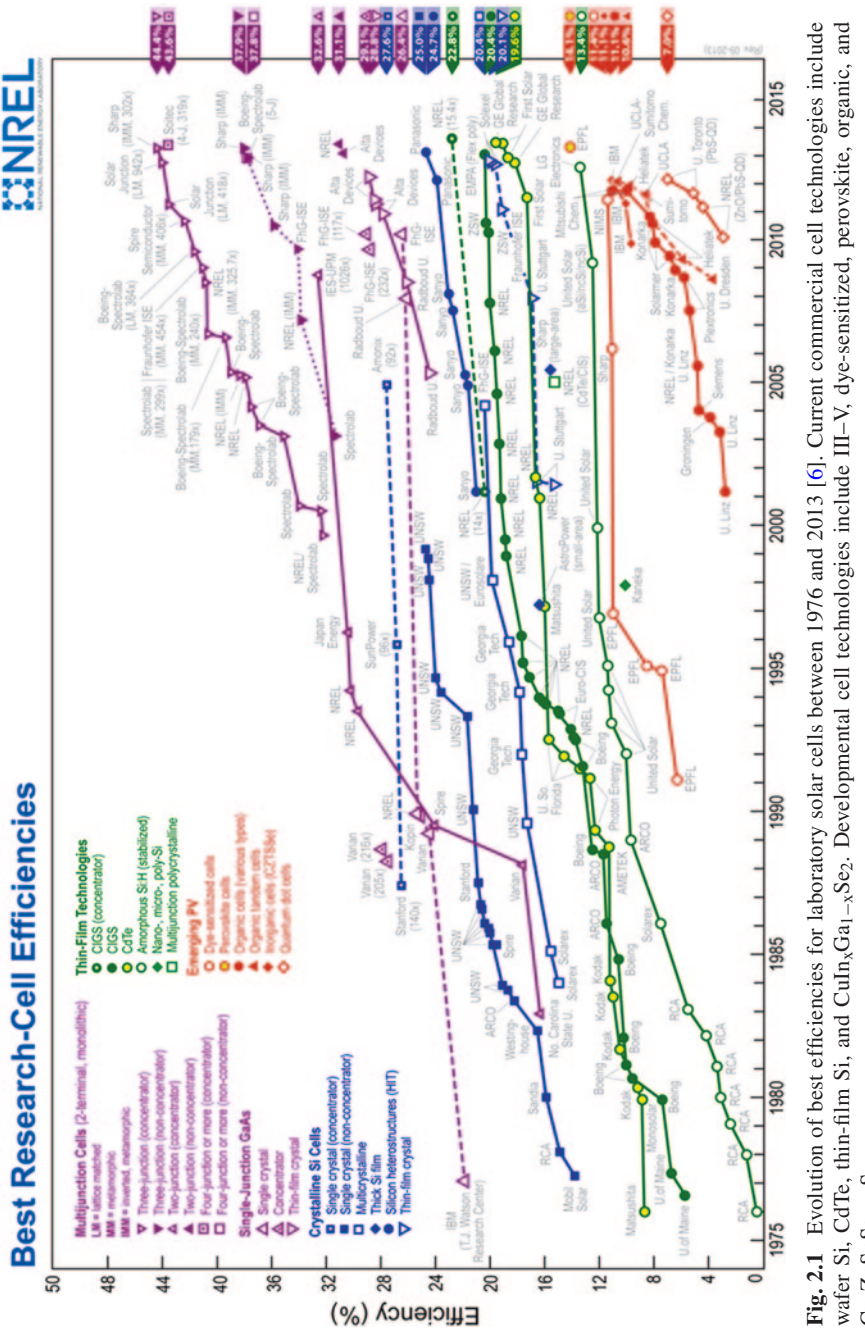

Fig. 2.1 Evolution of best efficiencies for laboratory solar cells between 1976 and 2013 [6]. Current commercial cell technologies include wafer Si, CdTe, thin-film Si, and $CuIn_xGa_{1-x}Se_2$. Developmental cell technologies include III–V, dye-sensitized, perovskite, organic, and $Cu_2ZnSnSe_{4-x}S_x$

over the last 37 years, which is compiled by the U.S. National Renewable Energy Laboratory in 2013 [6]. The energy conversion efficiency of a solar cell, η, is the ratio of the maximum electric power output and the incident solar power:

$$\eta(\%) = \frac{Maximum\ Electric\ Power\ Output}{Incident\ Solar\ Power}$$

The various commercial solar cell technologies in Fig. 2.1 include:

1. Wafer-Si solar cells, either monocrystalline or multicrystalline;
2. Thin-film cadmium telluride (CdTe) cells;
3. Thin-film Si cells, either amorphous or microcrystalline; and
4. Thin-film *c*opper *i*ndium *g*allium *s*elenide ($CuIn_xGa_{1-x}Se_2$ or CIGS) cells.

Current developmental solar cell technologies include:

1. III–V compound semiconductor multiple-junction tandem cells;
2. Dye-sensitized cells;
3. Perovskite cells;
4. Organic cells;
5. Thin-film *c*opper *z*inc *t*in *s*elenide *s*ulfide ($Cu_2ZnSnSe_{4-x}S_x$ or CZTSS) cells; and
6. Gallium arsenide (GaAs) single-junction cells.

The efficiency of monocrystalline-Si solar cells has reached 25.0 %, while that of multicrystalline-Si cells is 20.4 %. The record efficiency for all solar cell technologies is held at 44.4 % by a triple-junction tandem cell. This cell stacks three p-n junctions made of gallium indium arsenide ($Ga_xIn_{1-x}As$), gallium arsenide, and gallium indium phosphide ($Ga_yIn_{1-y}P$). Each junction has a different bandgap and is responsible for light absorption in a certain portion of the solar spectrum. The efficiency is measured with a concentrator under 302 suns. It is interesting that sunlight concentration adds 6–7 % in absolute efficiency for III–V tandem cells, from around 37 % to over 44 % by going from 1 sun to 300+ suns. The efficiency gain by concentration is less noticeable for wafer-Si solar cells with only 2–3 % gain in absolute efficiency, from 25 % at 1 sun to less than 28 % at about 100 suns.

Besides wafer Si, several thin-film solar cell technologies have been commercialized, including Si in either amorphous or microcrystalline form and two metal chalcogenides, CdTe and CIGS. Their record efficiencies are 20.4, 19.6, and 13.4 % for CIGS, CdTe, and thin-film Si cells, respectively. Several developmental solar cell technologies are also included in Fig. 2.1 including dye-sensitized cells, perovskite cells, organic cells, and CTZSS cells. Their efficiencies are between 7 and 11 %, with one exception. Within just a few years, perovskite cells have come out of obscurity with an efficiency of 14.1 % [7], a much faster pace than other developmental cell technologies.

While the accumulated progress in efficiencies of these laboratory solar cells over the years is remarkable, commercial cells are typically about two thirds of these laboratory efficiencies. This is partially due to non-uniformities in materials and processing over commercial-size cells, which are usually much larger than laboratory

cells. Laboratory cells are often about a few square centimeters in size. Commercial multicrystalline-Si cells are manufactured on 156 × 156 mm^2 square wafers, while commercial thin-film cells can be even bigger. Another reason is that laboratory cells can be fabricated with more sophisticated, thus more costly, processes, while commercial cells have to strike a balance between process cost and cell efficiency. For example, vacuum-based metallization such as evaporation and sputter deposition is used in the fabrication of laboratory cells but seldom in commercial cells.

There is also 1–2 % loss in absolute efficiency from cells to modules. Several factors contribute to the efficiency loss in modules. One is the optical losses such as absorption and reflection in the front glass sheet and laminating material, which is commonly ethylene vinyl acetate (EVA). Although only matched cells with similar efficiencies are used in a module, the small dispersion in efficiency leads to a mismatch loss. There are also resistive losses in module interconnects. In general, monocrystalline-Si modules can reach over 20 % efficiency, multicrystalline-Si and CIGS modules around 15 %, CdTe modules around 13 %, and thin-film Si modules around 10 %.

2.2 The Cost

Cost is the most well-known bottleneck to large-scale deployment of solar photovoltaics. The cost of solar electricity varies widely depending on many factors such as the size of the installed system, with lower costs for larger systems. Since our target for solar photovoltaics should be terawatt-scale deployment, we will focus on the cost of the largest utility-scale systems whose size is currently in the peak megawatt range (MW_p). The cost of the smallest residential rooftop systems, which are a few peak kilowatts (kW_p), can be twice as much as utility-scale systems on the basis of dollars per peak watt ($/$W_p$). The third category in system size is commercial systems, which are nowadays in tens to hundreds of peak kilowatts. The typical sizes of today's solar photovoltaic systems are listed in Table 2.1.

There are several methods to account for the cost of solar electricity. For manufacturers of solar cells and modules, the sale price of modules in $/$W_p$ is the most convenient method. In 2012, the prices for wafer-Si and thin-film CdTe modules were about $0.85/$W_p$. This represents a sharp decline in price, as the prices in 2011 were about $1.5/$W_p$. A better measure of the upfront cost of solar photovoltaics is the cost of installed systems, also in $/$W_p$, which includes the cost of solar modules and the cost of installation. Installation costs include mounting materials (racks and wires), inverters, labor, permits and fees, financing, and installer's expenses (overhead, taxes, marketing, and profit). These costs, especially the non-hardware costs, vary widely from one region to another and are more difficult to summarize. In 2012, the installation cost for utility-scale systems was on average about $2.5/$W_p$. For utility companies and consumers, the *l*evelized *c*ost *o*f *e*lectricity (LCOE) for solar photovoltaics is more important, which is defined as:

$$LCOE\ (¢/kWh) = \frac{Lifetime\ Cost}{Lifetime\ Electric\ Power\ Output}$$

Table 2.1 Typical sizes of today's solar photovoltaic systems and their expected future sizes

Classification	Current size	Future size
Residential system	Up to 10 kW_p	Up to 10 kW_p
Commercial system	10 kW_p–1 MW_p	10 kW_p–1 GW_p
Utility-scale system	1 MW_p and above	1 GW_p and above

Utility-scale systems have to reach peak gigawatt scales for a noticeable contribution to our future energy mix

Table 2.2 Comparison of three cost calculation methods for solar photovoltaics

Method	Unit	Pro	Con
Cost of solar module	$/$W_p$	A simple method to calculate module cost	Failure to count installation, operation and maintenance costs
Cost of installed system	$/$W_p$	A good method to calculate upfront cost	Failure to count operation and maintenance costs
Levelized cost of electricity	¢/kWh	A good method to compare with other electricity sources	Difficulty in estimating future labor and fuel costs

Each method has its pros and cons, but ultimately the levelized cost of solar electricity has to be competitive with other electricity sources

The lifetime cost includes not only the cost of installing solar systems, but also the cost for operating and maintaining solar systems. This method is useful in comparing the cost of solar electricity to electricity generated by other sources such as coal, oil, natural gas, hydropower, nuclear power, or wind. Solar photovoltaic systems have the advantage of little operation and maintenance costs, as they require no fuels and no constant labor. Occasional labor is needed for repair and cleaning, as modules accumulate dust over time which reduces the electric power output. Table 2.2 compares different cost calculation methods.

The second method in Table 2.2, the cost of installed systems, can be used to compare the upfront costs of various electricity generation technologies. For utility-scale solar systems, it is about $\$3.3/W_p$ in 2012. Solar systems produce no power at nights and little in early mornings and late afternoons. The time-averaged output of a solar system is somewhere between 10–20 % of its peak output, depending on several factors such as local solar intensity, weather, air quality, and landscape. For comparison purposes, the cost of installed solar systems needs to be converted from dollars per peak watt to dollars per watt. A $\$3/W_p$ solar system with 10–20 % time-averaged output is equivalent to \$15–30/W, several times higher than the upfront costs of nuclear or coal-fired power plants.

Figure 2.2 illustrates the average annual factory-gate price for solar modules between 2005 and 2012 [8]. Figure 2.3 shows the cost of installed residential (less than 10 kW_p) and commercial (larger than 100 kW_p) solar systems in the U.S. between 1998 and 2012 [9]. The module price has dropped by a factor of 4 from $\$3.8/W_p$ in 2005 to $\$0.85/W_p$ in 2012. Meanwhile the cost of installed residential systems has come down by a factor of about 1.7 from $\$8.8/W_p$ in 2005 to $\$5.3/W_p$

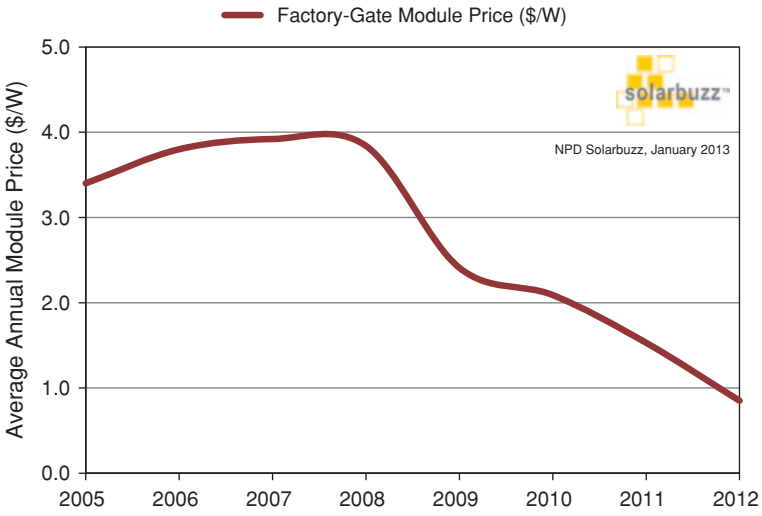

Fig. 2.2 Average annual factory-gate price for solar modules between 2005 and 2012 [8]. Reprinted with permission of NPD Solarbuzz. The module price has dropped by a factor of 4 between 2005 and 2012. The bounce-back between 2005 and 2008 was due to high demands and limited production capacities

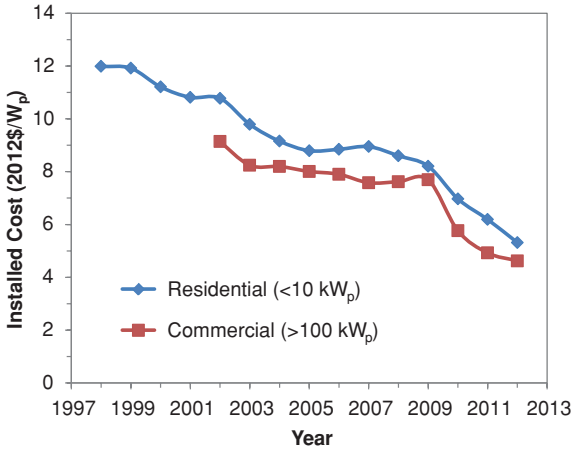

Fig. 2.3 Cost of installed solar systems in the U.S. between 1998 and 2012 for residential (less than 10 kW_p) and commercial (larger than 100 kW_p) systems [9]. The cost of residential systems has dropped from \$8.8/W_p in 2005 to \$5.3/W_p in 2012

in 2012, indicating a much slower pace in reducing installation costs for solar systems. There was a short-lived price bounce-back between 2005 and 2008. At the time the oil price was flying high, resulting in high demands for solar modules. The solar cell industry could not expand fast enough to keep up with the demands, leading to a price hike for solar modules.

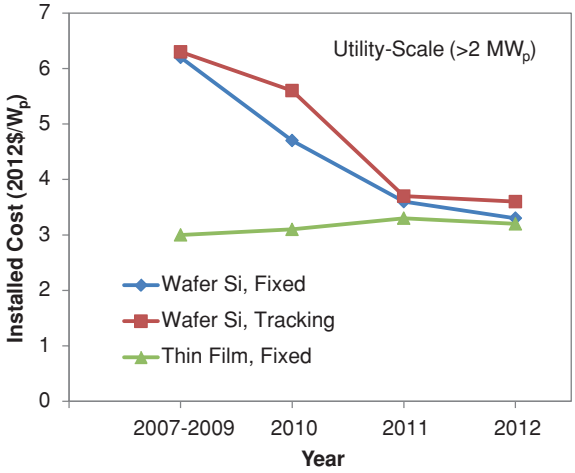

Fig. 2.4 Capacity-weighted average cost of installed utility-scale solar systems in the U.S. between 2007 and 2012 [9]. With the small number of utility-scale systems, the cost is calculated for the systems installed between 2007 and 2009. The average cost for installed utility-scale systems in 2012 is about $\$3.3/W_p$

The capacity-weighted average cost for utility-scale systems installed in the U.S. between 2007 and 2012 is presented in Fig. 2.4 [9]. The number of installed utility-scale systems is small at 11 systems between 2007 and 2009. Therefore, the capacity-weighted cost is calculated for the 11 systems between 2007 and 2009. There are 18 installed systems in the figure for 2010, 53 installed systems for 2011, and 106 systems for 2012. The cost of installed utility-scale wafer-Si solar systems, which have about 90 % of the market, has decreased from $\$6.25/W_p$ for 2007–2009 to $\$3.4/W_p$ in 2012. It is clear by comparing Figs. 2.3 and 2.4 that the economy of scale works for solar systems, with residential systems, which are typically less than 10 kW_p each, at $\$5.3/W_p$ versus utility-scale systems, which are above 1 MW_p each, at $\$3.3/W_p$ in 2012.

The cost breakdown of installed solar systems is worth some discussion, as shown in Fig. 2.5 [10]. Si wafers are the biggest contributor to the overall module cost at about 40 % as of 2012. Cell fabrication accounts for about 25 % of the module cost and module fabrication adds another 35 %. When the price of polycrystalline-Si feedstock was flying high in 2008 due to shortage, Si wafers were an even bigger factor accounting for 50–60 % of the module cost. In 2012, the price of solar modules was about $\$0.85/W_p$ and the cost of installed utility-scale solar systems was about $\$3.3/W_p$. The cost breakdown for installed solar systems is thus modules 26 % and installation 74 %.

The solar cell industry is extremely cost conscious. This is in sharp contrast to the semiconductor industry, where performance plays a critical role in driving the industry, although the same semiconductor, Si, is used in both industries. This can

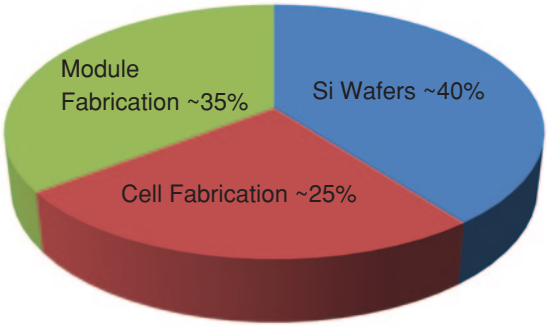

Fig. 2.5 Cost breakdown of solar modules as of 2012 [10]. Si wafers contribute to about 40 % of the module cost, cell fabrication accounts for 25 %, and module fabrication 35 %. In 2012 the module price is \$0.85/W_p and the utility-scale system cost \$3.3/W_p, so the cost breakdown of installed solar systems is modules 26 % and installation 74 %

be illustrated by solar-specific materials, processes, and equipment developed solely for the solar cell industry. One example is the directional solidification process for growth of multicrystalline-Si ingots to replace the Czochralski process for monocrystalline-Si ingots. Directional solidification requires roughly 15 kWh/kg of electricity (meaning 15 kWh of electricity to produce 1 kg of Si), versus about 100 kWh/kg for the Czochralski process, i.e. an 85 % reduction in electricity cost. The efficiency of multicrystalline-Si solar cells is lower than that of monocrystalline-Si cells, but the industry is willing to trade a little efficiency for a large return in cost. Another example is screen printing for metallization, which prints silver (Ag) and aluminum (Al) pastes onto Si cells as the front and back electrodes. In comparison, metallization in most record-efficiency Si cells is performed by vacuum-based deposition, e.g. evaporation or sputter deposition, and photolithographic patterning. Again, the industry trades efficiency for cost.

Innovative approaches to efficiency improvement in solar cells are being pursued worldwide. It is important to remember that efficiency improvement is often accompanied with additional cost, so it has to be done in a cost-effective manner. As an example, let us assume that a new technology promises an increase in cell efficiency from 15 to 18 %, i.e. a relative 20 % increase in efficiency. At the current module price, \$1/W_p, the additional cost for the new technology cannot exceed 20 % of \$1/W_p, i.e. 20¢/W_p, in order to keep the cost constant on a dollars per peak watt basis. In other words, a 100 W_p module now outputs 120 W_p with the new technology, and can be sold for up to \$120 at the current module price of \$1/W_p:

$$\frac{\$120}{120\,W_p} = \$1/W_p$$

In fact, the additional cost often has to be lower than 20¢/W_p, to provide incentives to cell and module manufacturers for their adoption of the technology.

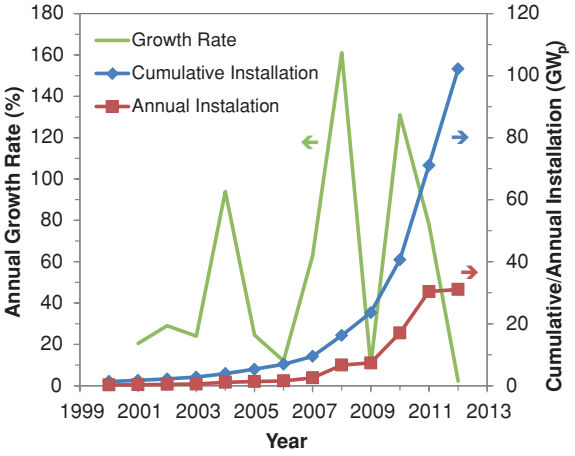

Fig. 2.6 Global cumulative and annual installations of solar photovoltaics between 2000 and 2012 [11]. The annual installation is just over 30 GW_p and the cumulative installation just over 100 GW_p in 2012. The year-to-year growth rate is calculated from the annual installation data

2.3 The Market

The solar cell industry has been experiencing phenomenal growth, about 50 % annually on average, since 2005 when the latest round of oil price hikes started. The crude oil price was about $30/barrel in 2004 and shot up to over $140/barrel in 2008. The higher oil prices played an important role in bringing public attention to the grand energy challenge we are facing, and prompted the rapid growth of the solar cell industry. Nevertheless, the solar cell industry is starting from scratch and the current fossil-fuel based energy industry is enormous in size. Today solar electricity makes a negligible contribution to our energy mix, providing roughly 0.3 % of the global electricity capacity. It will take the industry decades of phenomenal growth to make solar electricity a noticeable source of energy in our life.

Figure 2.6 illustrates the global annual and cumulative installations of solar photovoltaics between 2000 and 2012 [11]. In 2012, the annual installation of solar modules was just over 30 GW_p, while the cumulative installation reached 100 GW_p. About 70 % of the cumulative installation and about 55 % of the annual installation in 2012 were in Europe. It is revealing to compare the capacity of solar photovoltaics to the global electricity capacity, which is just over 5 TW in 2010 according to the U.S. Energy Information Administration [12]. 100 GW_p of solar photovoltaics provides 10–20 GW of time-averaged output, roughly 0.3 % of the global electricity capacity. Solar electricity will remain an insignificant source of energy for many years to come.

Figure 2.6 also calculates the year-to-year growth rate of the solar cell industry from the annual installation data. As an industry in its infancy, its growth has witnessed huge ups and downs. The year-to-year growth rate has been as high as 160 % and as low as 2 %, and on average about 50 % between 2000 and 2012. With an average annual growth rate of 40 %, the capacity of solar photovoltaics could reach 10 TW_p in 15 years, providing about 30 % of the current electricity capacity, if there were no fundamental roadblocks to its future growth. However, as discussed later

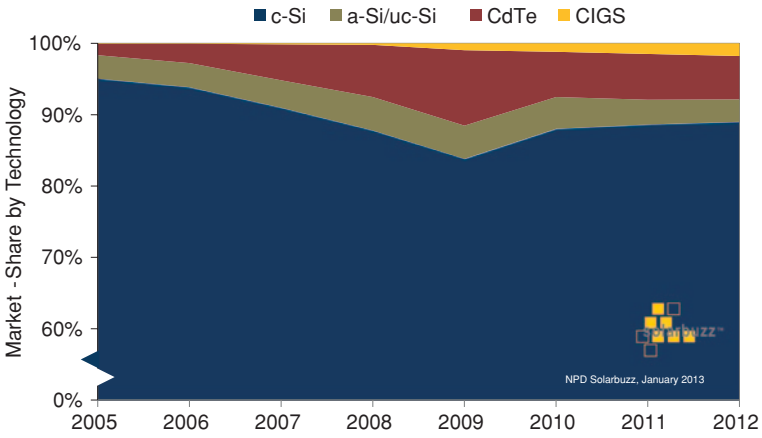

Fig. 2.7 Historical market shares by different solar cell technologies between 2005 and 2012 [8]. Reprinted with permission of NPD Solarbuzz. Wafer-Si solar cells dominate the solar cell industry with about 89 % of the market in 2012. CdTe is the second with roughly 6 % of the market. Thin-film Si has close to 4 % of the market, and CIGS slightly over 1 %

in this book, the future growth of the solar cell industry will likely be constrained by multiple roadblocks and bottlenecks such as large-scale storage of solar electricity, recycling of large-quantity solar modules, and availability of natural resources including raw materials and electricity. In this book, electricity is considered as a natural resource since it is largely generated using natural resources of limited supply: coal, oil, natural gas, nuclear fission, hydropower, or wind. On the other hand, as the base of the solar cell industry expands, its growth will naturally slow down even without these roadblocks and bottlenecks.

Out of all the solar cell technologies in Fig. 2.1, wafer-Si solar cells, either multicrystalline or monocrystalline, dominate the solar cell industry with about 89 % of the market in 2012 (Fig. 2.7). CdTe is the second market leader with roughly 6 % of the market. Thin-film Si solar cells, either amorphous or microcrystalline, have close to 4 % of the market, and CIGS slightly over 1 %. It is interesting that III–V triple-junction tandem cells have practically no market share, although they are commercially ready and they hold the efficiency record at 44.4 %. This further illustrates the cost-driven nature of the solar cell industry, as triple-junction tandem cells are prohibitively expensive. They are primarily employed in space and military applications, where performance is the determining factor.

The market share by CdTe is particularly worth noting. It was about 1.5 % in 2005, and within 4 years it expanded to over 10 % in 2009. This becomes more impressive when we consider the rapid growth of the solar cell industry as a whole during the same period, from 5.36 GW_p annual installation in 2005 to 23.6 GW_p in 2009 (Fig. 2.6). The solar cell industry as a whole grew more than 4 times in 4 years between 2005 and 2009, while the production of CdTe modules grew over 25 times in the same period. Since 2009 CdTe has been losing its market share, and this trend is expected

Table 2.3 Required installations of solar photovoltaics for different contributions to our future energy mix

Contribution (%)	2050 (30 TW) (TW_p)	2100 (46 TW) (TW_p)
10	15–30	23–46
20	30–60	46–92
30	45–90	69–138
40	60–120	92–184
50	75–150	115–230

Tens to hundreds of peak terawatts of solar photovoltaics are required to make it an important source of energy in the future

to continue as long as the solar cell industry continues its rapid growth. This book will explain the reasons behind the shrinking market share by the CdTe technology.

Let us now examine future market opportunities for solar photovoltaics. The global energy demand is projected to reach 30 TW by 2050 and 46 TW by 2100 [13]. These future energy demands will have to be met largely by carbon-free sources. The required amounts of carbon-free energy depend on our target for atmospheric CO_2 concentration. If the target is 750 ppm, Fig. 1.1 suggests about 11 TW carbon-free energy by 2050 and about 30 TW by 2100, or roughly 37 % of the total energy demand in 2050 and 65 % in 2100. Solar photovoltaics is one of the few carbon-free energy sources which are ready for large-scale commercial deployment. If solar photovoltaics is to help stabilize the atmospheric CO_2 concentration, it will have to provide a significant percentage, at least 10 %, of our future energy demands. Table 2.3 lists several scenarios for different contributions from solar photovoltaics to our future energy mix. The required installation of solar photovoltaics for 30 % contribution in 2050 is somewhere between 45 and 90 TW_p depending on the time-averaged output of the modules. In 2100 the required installation for 30 % contribution is 69–138 TW_p. Comparing these numbers with the current cumulative installations, about 100 GW_p in 2012, the capacity of solar photovoltaics will have to expand at least 500 times by 2050 and about 1,000 times by 2100 from its current level. Both the potential and gap for solar photovoltaics are enormous!

In order to install, say, 60 TW_p of solar modules by 2050, the size of the solar systems has to increase dramatically. The current size of the largest utility-scale systems is a few peak megawatts (Table 2.1). At 1 MW_p each, we would have to install 60,000,000 solar systems to reach 60 TW_p, i.e. about 4,500 1 MW_p solar systems each day between now and 2050. Table 2.1 suggests that the future size of utility-scale systems has to be at minimum 1 GW_p each. 60 TW_p of solar photovoltaics by 2050 requires 3–4 solar systems of 1 GW_p capacity every day between now and 2050, with the balance provided by smaller-scale residential and commercial systems.

Let us now estimate the required annual production rate of solar photovoltaics. Assume that our goal is to maintain 60 TW_p steady-state installation. At an average lifetime of 25 years, 2.4 TW_p of solar modules would go through their life cycles each year and need to be replaced, i.e. the required annual production for 60 TW_p steady-state installation would be about 2.4 TW_p/year. This is roughly 80 times the 2012 annual production at about 30 GW_p/year.

Although the potential for solar photovoltaics is enormous, the actual role of solar photovoltaics in our future energy mix depends on our success in removing roadblocks and bottlenecks to terawatt-scale deployment of solar photovoltaics. Besides cost and efficiency, the roadblocks to terawatt solar photovoltaics include terawatt-scale storage of solar electricity, recycling of terawatt-quantity solar modules, and availability of natural resources such as raw materials and electricity. If we fail to remove these roadblocks, solar photovoltaics may always be small demonstration projects and other solar technologies, such as solar fuels or concentrated solar power systems, could dominate our future energy mix. This book will provide an analysis on some of the roadblocks and bottlenecks to terawatt solar photovoltaics, with a focus natural resource limitations. It also attempts to identify sound technological approaches to overcoming these roadblocks and bottlenecks.

References

1. Becquerel E (1839) Mémoire sur les effets électriques produits sous l'influence des rayons solaires. Comptes Rendus 9:561–567
2. Fritts CE (1883) On a new form of selenium cell, and some electrical discoveries made by its use. Am J Sci 26:465–472
3. Ohl RS (1946) Light-sensitive electric device. U.S. Patent no. 2,402,662
4. Chapin DM, Fuller CS, Pearson GL (1954) A new silicon p-n junction photocell for converting solar radiation into electrical power. J Appl Phys 25:676–677
5. Zhao J, Wang A, Green MA, Ferrazza F (1998) 19.8 % efficient 'honeycomb' textured multicrystalline and 24.4 % monocrystalline silicon solar cells. Appl Phys Lett 73:1991–1993
6. U.S. National Renewable Energy Laboratory (2013) Best research-cell efficiencies. Available at http://www.nrel.gov/ncpv/images/efficiency_chart.jpg
7. Burschka J, Pellet N, Moon S-J, Humphry-Baker R, Gao P, Nazeeruddin MK, Gratzel M (2013) Sequential deposition as a route to high-performance perovskite-sensitized solar cells. Nature 499:316–319
8. NPD Solarbuzz (2013) Marketbuzz® 2013
9. Barbose G, Darghouth N, Weaver S, Wiser R (2013) Tracking the Sun VI (U.S. Lawrence Berkeley National Laboratory, 2013). Available at http://emp.lbl.gov/sites/all/files/lbnl-6350e.pdf
10. Goodrich A, Hacke P, Wang Q, Sopori B, Margolis R, James TL, Woodhouse M (2013) A wafer-based monocrystalline silicon photovoltaics roadmap: utilizing known technology improvement opportunities for further reductions in manufacturing costs. Sol Energ Mater Sol Cells 114:110–135
11. European Photovoltaic Industry Association (2013) Global market outlook for photovoltaics 2013–2017. Available at http://www.epia.org/fileadmin/user_upload/Publications/GMO_2013_-_Final_PDF.pdf
12. U.S. Energy Information Administration (2012) International energy statistics 2012. Available at http://www.eia.gov/cfapps/ipdbproject/iedindex3.cfm
13. Hoffert MI, Caldeira K, Jain AK, Haites EF, Harvey LDD, Potter SD, Schlesinger ME, Schneider SH, Watts RG, Wigley TML, Wuebbles DJ (1998) Energy implications of future stabilization of atmospheric CO_2 content. Nature 395:881–884

Chapter 3
Physics of Solar Cells

In this chapter solar cell physics is reviewed. The discussion starts with classification of solar cells. Solar cell operation is introduced in the context of the two essential processes in any solar cell, i.e. light absorption and charge separation. Various loss mechanisms including optical, recombination, and resistive losses in solar cells are discussed and their remedies are outlined. Parameters quantifying solar cell performance beyond cost and efficiency are introduced. The reader is assumed to have college-level solid-state physics or device physics knowledge.

3.1 Classification of Solar Cells

A photovoltaic solar cell takes in solar energy and outputs electric energy. In a generalized description, two processes have to be present simultaneously in any photovoltaic solar cell in order for it to convert sunlight into electricity:

1. Light absorption to convert photons into charge carriers, which are excited electrons and the vacant states left behind by excited electrons; and
2. Charge separation by a built-in potential difference, which also drives the electrical current through an external load.

Although there are many different solar cell technologies today and some of them are included in Fig. 2.1, their operations are all based on the two essential processes above with no exception. The differences among various cell technologies are two-fold:

1. The material they employ for light absorption varies from an inorganic semiconductor to an organic semiconductor to possibly a nanostructured semiconductor; and
2. There are a number of methods to build a potential difference from a p-n junction to a Schottky junction to a heterogeneous interface between two dissimilar semiconductors.

M. Tao, *Terawatt Solar Photovoltaics*, SpringerBriefs in Applied Sciences and Technology, DOI: 10.1007/978-1-4471-5643-7_3, © The Author(s) 2014

Although there are various methods to build the potential difference in solar cells, all the commercial solar cells today, wafer Si, CdTe, thin-film Si, and CIGS, employ a p-n junction for charge separation. The p-n junction may be homogeneous, i.e. a junction between p-type and n-type of the same semiconductor, or heterogeneous, i.e. a junction between p-type and n-type of two different semiconductors. All other approaches for the built-in potential difference are employed only in research cells, as they have yet to demonstrate their advantages over a p-n junction in performance, reliability, or cost. For this reason, the most common classification method for solar cells is based on the material they employ for light absorption, as illustrated in Fig. 2.1.

Categorically, there are two types of solar cells according to the absorber material:

1. Inorganic solar cells, in which the absorber is an inorganic semiconductor. This category includes all the commercial solar cells today including wafer Si (either monocrystalline or multicrystalline), thin-film CdTe, thin-film Si (either amorphous or microcrystalline), and thin-film CIGS, as well as developmental III–V compound semiconductor multiple-junction tandem, GaAs single-junction, CZTSS, and perovskite cells.
2. Organic solar cells, in which the absorber is an organic semiconductor. This includes organic cells and dye-sensitized cells, which are under development. The absorber in dye-sensitized cells is dye molecules, an organic material.

In general, inorganic solar cells have higher efficiencies than organic cells. Except the newest cell technology CZTSS, all inorganic cells in Fig. 2.1 have efficiencies from 13 to over 40 %. Organic cells are typically around 10 %. This disparity can be attributed to the better electrical and optical properties of inorganic semiconductors over organic semiconductors, which will be discussed in more details in this chapter.

On the other hand, the fabrication of inorganic solar cells often involves vacuum-based processes for film deposition, dopant diffusion, and etching. Examples include plasma-enhanced chemical vapor deposition for silicon nitride (Si_3N_4 if stoichiometric or SiN_x if non-stoichiometric) as the antireflection layer in wafer-Si solar cells, sputter deposition of transparent conducting oxide in thin-film solar cells, reactive ion etching for edge isolation in wafer-Si solar cells, among others.

A major motivation for organic solar cells is that a large portion of their fabrication can be carried out by solution-based processes, which typically have lower costs than vacuum-based processes. When coupled with low-cost materials, organic cells promise reduced module costs over inorganic cells. A major research direction in solar photovoltaics should be solution-based processes for the fabrication of inorganic solar cells. The goal is to reduce the fabrication costs of inorganic solar cells, while maintaining their higher efficiencies. Solution-based fabrication is more difficult for Si solar cells, including wafer Si and thin-film Si, than thin-film chalcogenide solar cells. CdTe, CIGS, CZTSS, and several solar photovoltaic materials under development have better chances for solution fabrication.

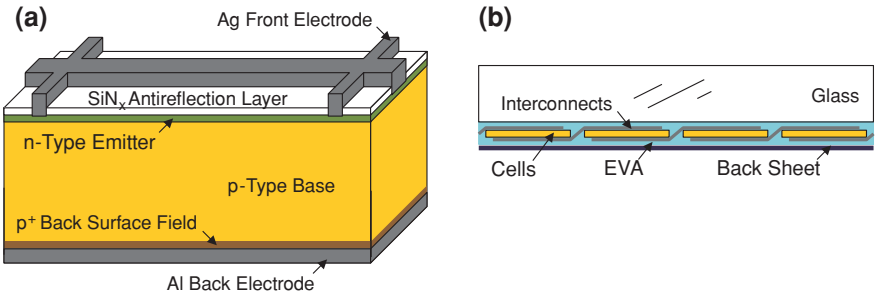

Fig. 3.1 Schematic of **a** wafer-Si cells and **b** wafer-Si modules. The figures are not drawn to scale. Light absorption takes place largely in the base, while charge separation is performed by the p-n junction between emitter and base in (**a**). Surface texture is not shown in (**a**). In (**b**), the solar cells are connected in series and then sealed in a module

Solution-based fabrication of Si solar cells is likely difficult due to the strong and directional covalent bond in Si. Both the bond length and angle are rigidly fixed in Si. Any atomic misplacement leads to a strained bond or a dangling bond, both of which are electrical defects in the crystal. For this reason, solution-based synthesis of Si has not produced a device-quality material and low-temperature vacuum-based synthesis of Si, such as plasma-enhanced chemical vapor deposition, results in highly-defective Si. In fact, the density of defects is so high in low-temperature vacuum-deposited Si that the material becomes structurally amorphous and the electrical properties deteriorate dramatically. As an example, the carrier mobility in amorphous Si is often below 1 cm^2/V-s, versus 450–1,500 cm^2/V-s in monocrystalline Si. On the contrary, ionically-bonded semiconductors such as metal chalcogenides have demonstrated their capability for solution synthesis with excellent crystal quality. The ionic bond is non-directional, i.e. the bond angle is not rigidly fixed due to the Coulombic nature of the bond. The flexibility of the ionic bond allows small atomic misplacement to be accommodated in the crystal without introducing an electrical defect. The implication is significant, as many metal chalcogenides have been synthesized into multicrystalline forms by solution-based processes with excellent electrical properties, enabling solution-fabricated high-efficiency inorganic solar cells.

Figure 3.1 illustrates schematically the most popular structures of today's commercial wafer-Si cells and modules. The Si wafer, either monocrystalline or multicrystalline, is p-type with a resistivity of about 1 Ω-cm and a thickness between 180 and 200 μm. On the front, phosphorus is diffused into the wafer to form an n-type layer of about 0.5 μm deep, which is called the emitter. The antireflection layer is 75 nm SiN_x, and the front finger-shaped electrode is made of Ag. The back electrode is Al. The Al also diffuses into Si to form a heavily p^+-type region, which is called the back surface field. In a module, typically 60 or 72 wafer-Si solar cells are connected in series, so current matching among the cells is critical to minimize mismatch losses. The cells, front glass sheet, and backsheet are laminated together with a thermoplastic material, commonly EVA. The edges

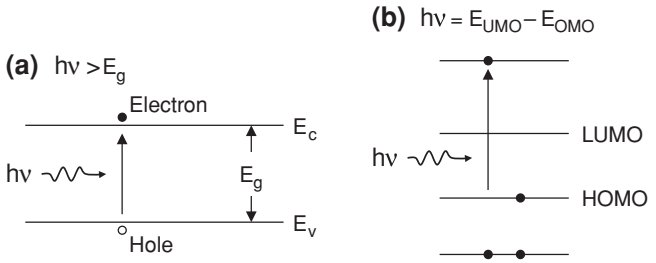

Fig. 3.2 Absorption mechanisms in **a** inorganic semiconductors and **b** organic molecules. A photon with energy hν larger than the bandgap E_g can be absorbed by the inorganic semiconductor in (**a**). A photon with energy equal to the energy difference between an unoccupied molecular orbital and an occupied molecular orbital, $E_{UMO} - E_{OMO}$, can be absorbed by the organic molecule in (**b**)

of the laminated piece are then sealed with an Al frame. The peak power by such a module, i.e. the power delivered at noon, is between 250 and 350 W_p, with over 8 A in current and about 30 or 36 V in voltage.

3.2 Operation of Solar Cells

In this section, the physics behind solar cell operation is discussed. Instead of the specific physics of a particular cell technology, the intent of the author is to provide the reader with a general picture of solar cell operation across various cell technologies. This includes major types of semiconductors for light absorption and different approaches to establish a built-in potential difference. This way the reader can develop a sense of the pros and cons of each cell technology in terms of their device physics.

3.2.1 Light Absorption in Solar Cells

A wide range of semiconductors, from inorganic to organic, can be used in solar cells as the absorber. However, the absorption mechanisms in different semiconductors vary. In inorganic semiconductors, band-to-band excitation is the dominant mechanism for light absorption as shown in Fig. 3.2a. When a photon with energy hν larger than the bandgap, E_g, enters the semiconductor, it has a chance to be absorbed exciting an electron from the valence band into the conduction band. The excited electron leaves behind a vacant state in the valence band, i.e. a hole. Both the electron and the hole can contribute to the output current of the solar cell.

The chance for a photon, if its energy is slightly larger than the bandgap, to be absorbed depends on the band structure of the inorganic semiconductor, i.e. whether the bandgap is direct or indirect. The bandgap of a semiconductor is defined as the

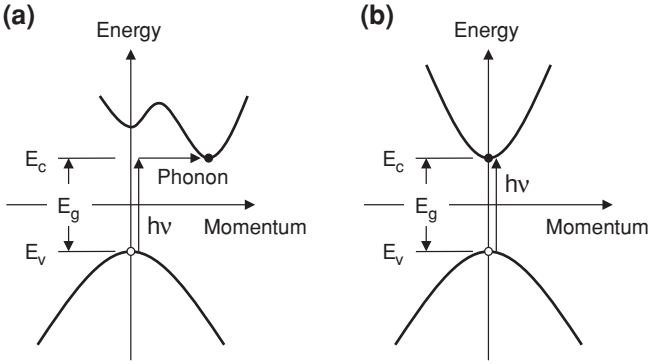

Fig. 3.3 Absorption mechanisms in **a** indirect bandgap semiconductors and **b** direct bandgap semiconductors. To excite an electron by a photon with energy equal to the bandgap in (**a**), a phonon is required to change the momentum of the excited electron. Momentum conservation is always obeyed in (**b**) when an electron is excited by a photon with energy equal to the bandgap

energy difference between the minimum of its conduction band, E_c, and the maximum of its valence band, E_v, as shown in Fig. 3.3. In an indirect bandgap semiconductor such as Si, the conduction band minimum is displaced from the valence band maximum in the momentum domain (Fig. 3.3a). As a photon practically does not change the momentum of the exited electron, a phonon is often required in the absorption process of an indirect bandgap semiconductor for momentum conservation. As shown in Fig. 3.3a, when a photon with energy slightly larger than the bandgap is absorbed by an electron at the valence band maximum, the momentum of the excited electron has to change in order for it to jump into the conduction band minimum, which requires a phonon. This phonon involvement reduces the chances of absorption for photons with energies just slightly larger than the bandgap of the semiconductor. In a direct bandgap semiconductor such as CdTe, the conduction band minimum coincides with the valence band maximum (Fig. 3.3b), and thus momentum conservation is always obeyed whenever a photon is absorbed leading to higher chances for photon absorption.

A consequence of the different chances for photon absorption is that it requires a layer of hundreds of micrometers of an indirect bandgap semiconductor to absorb most of the incident sunlight, while it takes only a few micrometers of a direct bandgap semiconductor to achieve the same. Direct bandgap semiconductors are the basis for thin-film solar photovoltaics, in which the semiconductor absorber is typically 1–5 μm thick. The thickness of the Si wafer in today's wafer-Si solar cells is 180–200 μm. Thin-film cell technologies include CdTe, CIGS, and thin-film Si. It is noted that, while crystalline Si has an indirect bandgap of 1.12 eV, amorphous Si has a direct bandgap of 1.75 eV and enables thin-film Si solar cells. Many III–V compound semiconductors used in multiple-junction tandem cells have direct bandgaps such as GaAs.

The mechanism for photon absorption in organic semiconductors is excitation of electrons from lower-energy occupied states to higher-energy unoccupied states, as shown in Fig. 3.2b. When a photon with energy equal to the energy difference

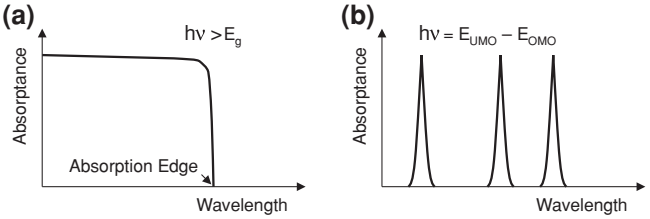

Fig. 3.4 Absorption spectra of **a** direct bandgap inorganic semiconductors and **b** organic molecules. Photons with energies larger than the bandgap can all be absorbed in a direct bandgap semiconductor, while an organic molecule can only absorb photons with energies equal to the energy differences between unoccupied states and occupied states

between an unoccupied state and an occupied state enters an organic semiconductor, it has a chance to be absorbed exciting an electron in the occupied state into the unoccupied state and leaving the lower-energy state vacant. The lowest unoccupied state is often called the *l*owest *u*noccupied *m*olecular *o*rbital (LUMO), and the highest occupied state is often called the *h*ighest *o*ccupied *m*olecular *o*rbital (HOMO). LUMO and HOMO are to organic semiconductors what conduction band minimum and valence band maximum are to inorganic semiconductors.

The different absorption mechanisms in Fig. 3.2 reveal one of the fundamental reasons for the low efficiencies of organic solar cells. Figure 3.4 schematically illustrates the absorption spectra for direct bandgap inorganic semiconductors and organic molecules. While direct bandgap inorganic semiconductors show large absorption coefficients for all the photons with energies larger than the bandgap, organic molecules only absorb photons with certain energies which are determined by the energy differences between unoccupied states, E_{LUMO}, and occupied states, E_{OMO}. In other words, inorganic semiconductors utilize a broader solar spectrum than organic molecules. In an organic semiconductor, the ensemble of many organic molecules broadens the absorption peaks of an individual molecule. Nevertheless, solar energy utilization in organic semiconductors is typically inferior to inorganic semiconductors.

The absorption threshold, or often called the absorption edge, in an inorganic semiconductor is determined by its bandgap, as shown in Fig. 3.4a. The absorption edge in an organic semiconductor is determined by the energy difference between LUMO and HOMO, i.e. $E_{LUMO} - E_{HOMO}$. The photon flux in a typical terrestrial solar spectrum is about 4.4×10^{17} photons/cm^2-s (Fig. 1.4). Assuming that every photon generates an electron-hole pair and every photo-generated charge carrier reaches the external load, the maximum possible current of a solar cell is the electron charge times the photon flux:

$$J_{max} = 1.6 \times 10^{-19} \times 4.4 \times 10^{17} = 70\,\text{mA/cm}^2$$

The absorption edge prevents absorption of those photons with energies smaller than the bandgap of an inorganic semiconductor. For wafer-Si solar cells with a

bandgap of 1.12 eV, the maximum possible current is about 44 mA/cm^2. Today's best wafer-Si cells can achieve over 40 mA/cm^2 in output current, sufficiently close to the maximum possible current. Obviously the smaller the bandgap of the semiconductor, the larger the maximum possible current of the cell.

3.2.2 Charge Separation in Solar Cells

Most commercial solar cells today employ a p-n junction for charge separation. As shown in Fig. 3.5a, the potential gradient in a homogeneous p-n junction drives photo-generated electrons to the n-side and holes to the p-side of the junction. When an external load is connected to the cell, the potential gradient drives an electrical current through the load, i.e. delivering electric power to the load. The width of the potential gradient in a p-n junction is on the order of micrometer with the typical doping levels used in solar cells. In thin-film solar cells, the potential gradient often extends throughout the entire semiconductor absorber. This results in immediate separation of photo-generated electron and hole pairs as soon as they appear, as they are generated within the potential gradient. In wafer-Si solar cells, the wafer is much thicker, more than 100 times, than the width of the p-n junction and most of the photo-generated charge carriers are produced outside the junction region. They will wander in pairs in the Si wafer due to Coulombic attraction until they reach the potential gradient for separation. It is possible that the electron-hole pairs recombine before reaching the junction, leading to a reduced electric power output. A good-quality Si crystal with few defects is critical to minimize the recombination loss. In other words, wafer-Si solar cells require better material quality than thin-film solar cells.

A heterogeneous p-n junction between two dissimilar semiconductors is employed in thin-film chalcogenide solar cells, in which n-type cadmium sulfide (CdS) and p-type CdTe or CIGS form a heterogeneous p-n junction. CdS has a bandgap of 2.42 eV, larger than that of CdTe or CIGS. In Fig. 3.5b, the two semiconductors have different bandgaps. The smaller bandgap semiconductor is the absorber. The larger bandgap semiconductor provides the potential gradient, as well as serves as the window. An appropriate band offset between and appropriate doping in the two semiconductors are required for effective charge separation. In Fig. 3.5b, the smaller bandgap semiconductor is p-type and the larger bandgap semiconductor is n-type. The conduction band offset ΔE_c is small to minimize the energy barrier for electrons moving from the smaller bandgap semiconductor to the larger bandgap semiconductor. The heterogeneous p-n junction extracts photo-generated electrons out of, and drives photo-generated holes into, the smaller bandgap semiconductor.

Although not utilized in commercial solar cells, a Schottky junction between a metal and an inorganic semiconductor can also create a potential gradient in the semiconductor. Figure 3.5c shows the band diagram of a Schottky junction, which extracts photo-generated holes out of, and drives photo-generated electrons into,

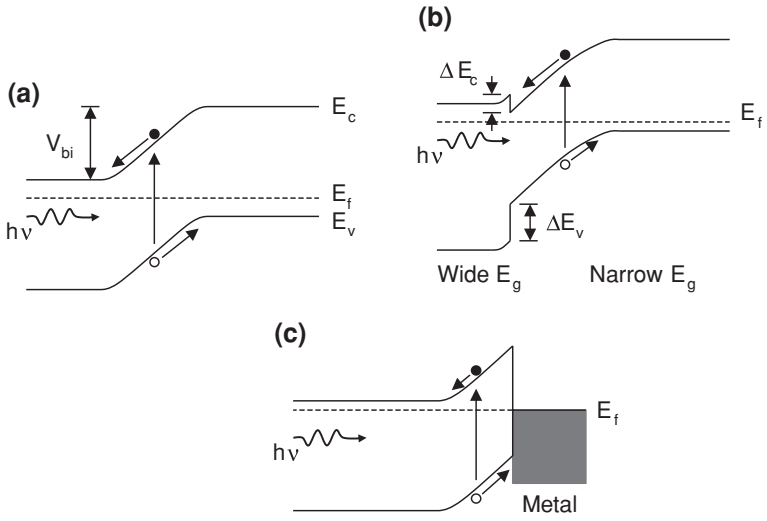

Fig. 3.5 Charge separation in inorganic solar cells by **a** a homogeneous p-n junction, **b** a heterogeneous p-n junction, and **c** a Schottky junction. Si solar cells, including wafer Si and thin-film Si, employ a homogeneous p-n junction. Thin-film chalcogenide solar cells, including CdTe and CIGS, employ a heterogeneous p-n junction

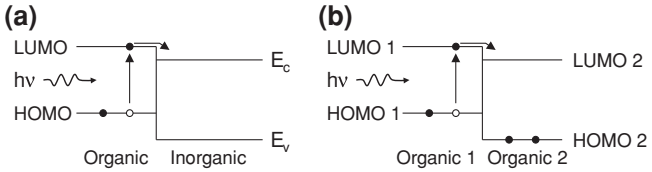

Fig. 3.6 Charge separation in organic solar cells by **a** an organic/inorganic interface and **b** an organic/organic interface. Dye-sensitized solar cells employ an organic/inorganic interface, while organic solar cells employ an organic/organic interface. Excited electrons are extracted out of the organic absorber by a lower-energy vacant state in another semiconductor

the semiconductor. The metal layer is better placed on the backside of the semiconductor to not block the incident sunlight into the semiconductor.

Organic solar cells do not rely on p-n junction for charge separation. Instead, they employ an organic/inorganic interface or an organic/organic interface, i.e. an interface between two dissimilar organic semiconductors, for charge separation as shown in Fig. 3.6. One important reason for not utilizing a p-n junction in organic solar cells is that doping in organic semiconductors is still a challenge [1]. Another reason is that photon absorption creates bound electron-hole pairs, called excitons, in organic semiconductors. Separation of excitons requires energy of a few tenths of an electron volt, and properly-aligned energy levels at a heterogeneous interface can provide such a driving force for effective exciton separation

in organic solar cells. In Fig. 3.6a, the organic semiconductor absorbs a photon which excites an electron from the HOMO into the LUMO. The conduction band minimum of the inorganic semiconductor has to be a few tenths of an electron volt below the LUMO of the organic semiconductor to extract the excited electron into the inorganic semiconductor for charge separation. The HOMO of the organic semiconductor needs to be above the valence band maximum of the inorganic semiconductor to prevent valence electrons from falling into the empty HOMO after photon absorption. Dye-sensitized solar cells employ an organic/inorganic interface for charge separation.

In Fig. 3.6b, organic semiconductor 1 is the absorber. When the LUMO of organic semiconductor 1 is a few tenths of an electron volt above the LUMO of organic semiconductor 2, photo-excited electrons can be injected from semiconductor 1 to semiconductor 2 for charge separation. The HOMO of organic semiconductor 1 also needs to be above the HOMO of organic semiconductor 2, which prevents HOMO electrons in semiconductor 2 from flowing into semiconductor 1. Various organic solar cells employ an organic/organic interface for charge separation.

Excitons in organic solar cells have very short diffusion lengths on the order of nanometer, i.e. the distance they travel before their recombination. This limits the thickness of the organic absorber to a few nanometers. Even though organic semiconductors have large absorption coefficients, the limited thickness of the absorber presents a challenge for effective absorption of the incident sunlight. To achieve a higher efficiency, the two semiconductors in organic solar cells are better made into a three-dimensional nanostructure for simultaneous, effective light absorption and charge separation. In dye-sensitized solar cells, the three-dimensional nanostructure is realized through a nanoporous film of titanium dioxide (TiO_2). The nanopores in the TiO_2 film are filled with the absorber, dye molecules, of a monolayer thick. The three-dimensional nanostructure increases the overall thickness of the dye molecules for light absorption, while maintaining the thickness of each dye molecule layer in the nanopores to a few nanometers. The porous TiO_2 film forms a continuous network of electron conductor for charge transport.

The potential difference for charge separation in inorganic solar cells is often created by a p-n junction. The maximum possible voltage of an inorganic solar cell is limited by the built-in potential V_{bi}, which is the total potential difference across the p-n junction as shown in Fig. 3.5a. By increasing the doping levels in the p-side and n-side of the p-n junction, the built-in potential increases. However, doping levels in an inorganic semiconductor cannot increase indefinitely and they are actually limited by solid solubilities of the dopants in the semiconductor. With practical solid solubilities, the maximum possible built-in potential is limited by the bandgap of the semiconductor:

$$V_{max} \leq V_{bi} \leq \frac{E_g}{q}$$

where V_{max} is the maximum possible voltage of a p-n junction solar cell and q is the electron charge. Obviously a larger bandgap allows a larger maximum possible voltage of the cell.

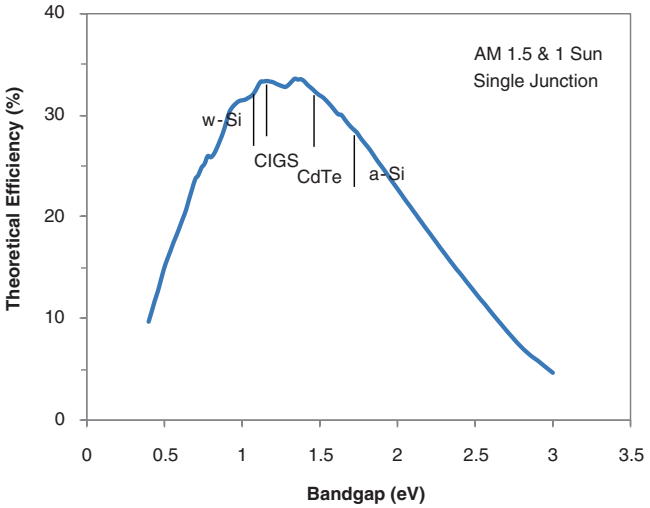

Fig. 3.7 Theoretical efficiency of a single-junction solar cell as a function of its bandgap under the AM 1.5 solar spectrum (Fig. 1.4). While the maximum possible efficiency is over 33 %, a range of bandgaps, from 1.1 to 1.5 eV, all give good efficiencies above 32 %. The bandgaps for wafer-Si, CdTe, amorphous-Si, and CIGS cells are marked

The discussions here and in Sect. 3.2.1 illustrate the critical importance of an appropriate bandgap in maximizing the efficiency of an inorganic solar cell. Maximizing efficiency means maximizing the output electric power, which is the product of current and voltage. To achieve a larger current out of a solar cell, a smaller bandgap is needed. To obtain a larger voltage, a larger bandgap is required. It can be imagined that when we maximize the power, there exists an optimum bandgap for solar cells which matches the solar spectrum for maximum efficiency. This has been examined in several studies [2, 3]. The exact value of the optimum bandgap varies slightly in different studies due to the solar spectrum used in the study, but is typically around 1.4 eV. Figure 3.7 shows the theoretical efficiency of an inorganic solar cell as a function of its bandgap using the reference AM 1.5 solar spectrum (Fig. 1.4). The maximum possible efficiency is over 33 % for a bandgap of about 1.35 eV. It is noted that a range of bandgaps, from 1.1 to 1.5 eV, all give good efficiencies above 32 %, which provides some leeway in our efforts to develop a low-cost, high-efficiency, and terawatt-capable solar cell technology.

3.3 Loss Mechanisms in Solar Cells

Figure 3.7 illustrates the theoretical efficiency of a single-junction solar cell as a function of its bandgap. It is noted that none of the inorganic solar cells in Fig. 2.1 has reached its efficiency limit. For wafer-Si solar cells, the best efficiency is 25.0 %, i.e. about 8 % below the efficiency limit. This is true for all other inorganic solar

cells, although the gap between efficiency limit and demonstrated efficiency varies. There are various loss mechanisms in solar cells which cause the discrepancy between actual efficiency and efficiency limit. These losses can be minimized, but it is hard to imagine that any of them can be completely eliminated with the known device physics we have today for solar cells. A major direction for solar cell research in the last 30 years has been the minimization of various loss mechanisms and thus setting new efficiency records for solar cells.

The various loss mechanisms in solar cells fall under three categories:

1. Optical losses: Not every photon from the solar spectrum necessarily enters the absorber of a solar cell, and not every photon which enters a solar cell is absorbed and converted to charge carriers.
2. Recombination losses: When a photon gets absorbed and creates charge carriers, not every photo-generated charge carrier reaches the external load. They may annihilate each other in pairs by recombination.
3. Resistive losses: When an electrical current is driven by the built-in potential through a solar cell, some of the potential is consumed by various resistances in the cell, reducing the power delivered to the external load.

Minimizing the various loss mechanisms in a cost-effective manner is an important role engineers play in advancing solar cell technologies.

3.3.1 Optical Losses

There are mainly four optical loss mechanisms in solar cells:

1. Reflection at front surface and interfaces;
2. Optical leak from front and back surfaces;
3. Absorption in non-active layers, and
4. Shadowing by front metal electrode.

Figure 3.8 illustrates the optical structure of a wafer-Si solar cell and three of these four optical losses.

Sunlight is an ensemble of electromagnetic waves of different wavelengths. Whenever an electromagnetic wave strikes an interface between two materials of different refractive indices, part of it is reflected back at the interface and does not enter the second material. Under normal incidence, the reflectance at the interface of two materials with refractive indices n_1 and n_2 is given by a Fresnel equation:

$$r = \left| \frac{n_1 - n_2}{n_1 + n_2} \right|^2$$

From air to Si, the reflectance is over 35 % with $n_{air} = 1.0$ and $n_{Si} = 3.9$ at 600 nm.

A well-established antireflection technique in optics is to sandwich an optically-transparent film between the two materials, with a refractive index between the two

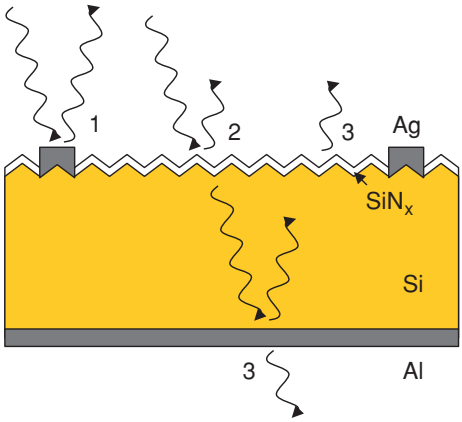

Fig. 3.8 Optical structure of the wafer-Si solar cell in Fig. 3.1 and optical losses in solar cells. Texture is shown for the back surface. Doping in Si barely changes its refractive index. "*1*" is shadowing by front electrode, "2" is reflection at front surface and Si/SiN_x interface, and "*3*" is optical leak from front and back surfaces. Light absorption in non-active layers is not shown in the figure

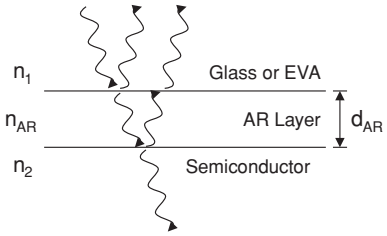

Fig. 3.9 Schematic of a single antireflection layer for solar cells. In solar modules, the antireflection layer is sandwiched between semiconductor absorber and glass or EVA. Its optimum thickness is 1/4 of the wavelength of interest and its optimum refractive index is the geometric mean of the indices above and below

materials (Fig. 3.9). The principle of the antireflection layer is quarter-wavelength destructive interference, i.e. its thickness should be:

$$d_{AR} = \frac{\lambda}{4n_{AR}}$$

n_{AR} is the refractive index of the antireflection layer, and λ is the wavelength of interest in vacuum. For the broad solar spectrum, the wavelength at maximum intensity, about 600 nm, is often used to determine the thickness of the antireflection layer. There is also an optimum value for the refractive index of the antireflection layer, which can be proven with Fresnel equations:

$$n_{AR} = \sqrt{n_1 n_2}$$

where n_1 and n_2 are the refractive indices of the materials below and above. As solar cells are typically packaged into modules, the material on top of the cells is glass or EVA with refractive indices of about 1.4. Therefore, the optimum index of the antireflection layer on wafer-Si solar cells is around 2.34 with $n_{Si} = 3.9$ at 600 nm.

Other factors to consider in selecting an antireflection material include bandgap, transmittance, material availability and cost, and process complexity. Typically the minimum bandgap required is 3 eV to allow most of the solar spectrum to pass through. High transmittance means little absorption for photons with energies below the bandgap. Below-bandgap absorption in antireflection layer may be caused by structural defects and/or impurities in the material. The most common antireflection material in wafer-Si solar cells today is SiN_x with a refractive index of 2.0 at 600 nm and a thickness of 75 nm. SiN_x is prepared by plasma-enhanced chemical vapor deposition, which is a vacuum-based process. Another candidate material for antireflection in wafer-Si solar cells is TiO_2, which has a refractive index of 2.6 at 600 nm and can be deposited by solution-based processes. The main disadvantage of TiO_2 is that it is a semiconductor, which can introduce a leakage current between the two electrodes in a cell.

It should be noted that the antireflection layer discussed above is designed to minimize reflection of a particular wavelength at a particular incident angle. For solar cells, the wavelength at maximum solar intensity, 600 nm, and normal incidence are usually used to design the antireflection layer. The solar spectrum is broad from 300 to 2,500 nm (Fig. 1.4). Without two-axis tracking, the incident angle varies between sunrise and sunset and throughout the year. Therefore, the effectiveness of the antireflection layer in Fig. 3.9 is limited.

Another common technique for antireflection is surface roughening. This is best illustrated by texturing of Si(100) wafers as the anisotropic nature of the single crystal allows a pyramidal surface texture. When a Si(100) wafer is immersed into a solution containing sodium hydroxide (NaOH), the etch rate on the (111) planes is much slower than on the (100) planes. This exposes the (111) planes in the crystal, resulting in pyramids of random sizes on the wafer. The pyramidal texture reduces surface reflection by introducing second chance of incidence for sunlight, as shown in Fig. 3.10. If the surface reflectance is r and the incident solar intensity is I_o, the amount of solar energy reflected after first incidence is rI_o. If the reflected solar energy, rI_o, strikes the surface for the second time, the amount of solar energy reflected is now r^2I_o, i.e. the equivalent surface reflectance is now r^2. For a Si wafer in air, the reflectance is 35 % before surface texturing and becomes 12 % after surface texturing. In today's wafer-Si solar cells, a SiN_x antireflection layer is often deposited on textured Si wafers, and the combination of the two techniques can reduce the surface reflectance to almost zero for a particular wavelength at a particular incident angle.

This pyramidal texturing technique is unique for monocrystalline Si as it relies on the anisotropic nature of a single crystal. It does not work as well on multicrystalline Si since the crystal grains are randomly oriented in multicrystalline materials, and it does not work on microcrystalline or amorphous materials.

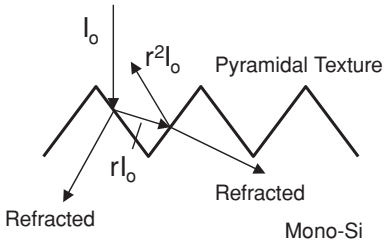

Fig. 3.10 Antireflection by a pyramidal surface texture on monocrystalline-Si solar cells. The reflected light after first incidence strikes the surface for the second time due to the pyramidal texture. The reflected intensity after first incidence is rI_o, where I_o is the intensity of incident sunlight and r is the surface reflectance. The reflected intensity after second incidence is r^2I_o

More complicated surface roughening techniques have been developed for multicrystalline Si, CdTe, thin-film Si, and CIGS. Some of them are used in commercial solar cells and many of them are not, as their cost effectiveness has yet to be demonstrated.

Optical leak is caused by poor light trapping, i.e. some of the sunlight which enters a solar cell escapes the cell from either the front or back surface. One pass by light from front side to backside of a cell does not allow complete absorption of all the photons. This is particularly true for Si as its indirect bandgap leads to a small absorption coefficient. Ideally the solar cell should act like an optical cavity, i.e. the front and back surfaces of the cell should be perfect mirrors for light already in the cell (To incident sunlight, the front surface should be a perfect antireflector). Once sunlight enters the cell, it is bounced back and forth at the front and back surfaces until it is completely absorbed. In most wafer-Si solar cells, the back surface is covered by a metal, typically Al, which serves as a reasonable reflector (Fig. 3.8).

The front reflector cannot be a metal, as it would block the incident sunlight. When light gets reflected from the back surface and travels from backside to front side in a cell, it goes from the high-index semiconductor to the low-index antireflection layer. This reverse index profile serves as a partial mirror for the backward light by total internal reflection. Figure 3.11 shows the onset of total internal reflection when the incident angle is equal to the critical angle given by:

$$\theta_c = \arcsin \frac{n_{AR}}{n_{Si}}$$

At this angle the refracted light travels along the interface and no light enters the antireflection layer. When the incident angle is larger than the critical angle, all the light is specularly reflected back into the semiconductor. This means that only light with incident angle smaller than the critical angle has a chance to escape from the front surface of the cell. For a SiN_x/Si structure, the critical incident angle is about 31°.

When wafer-Si solar cells are packaged into a module, the non-active layers in front of the cells include glass, EVA, and SiN_x (Fig. 3.1b). EVA is a polymer with a reasonable transmittance and a reasonable cost. Low-iron (Fe) glass is required in

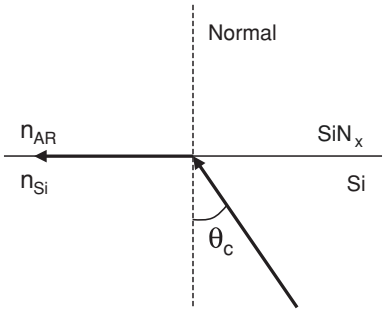

Fig. 3.11 Onset of total internal reflection. When light goes from a high-index material to a low-index material, there exists a critical incident angle. Beyond it all the light gets specularly reflected and no light enters the low-index material. At the critical angle the refracted light travels along the interface between the two materials

solar modules with transmittance above 90 %, as Fe causes significant below-bandgap absorption. For thin-film solar modules, the non-active layers in front of the cells also include low-Fe glass and EVA, but the SiN_x layer is replaced with a layer of transparent conducting oxide. The transparent conducting oxide layer serves both as the antireflection layer and one of the two electrodes in the cell. *I*ndium *t*in *o*xide (ITO) has the best performance among all the transparent conducting oxides to date in terms of transmittance and resistance. Fluorine-doped tin oxide and aluminum-doped zinc oxide are also used in thin-film solar cells, although their performance is still inferior to ITO.

The front metal electrode has to be in a finger shape to allow sunlight through. In today's wafer-Si solar cells, the coverage of the front metal electrode is typically between 5 and 10 % of the surface area, which translates into about 1 % loss in absolute cell efficiency due to the shadowing effect. Simply reducing the width of the metal fingers can reduce the shadowing loss, but the resistive loss in the metal fingers increases as the cross section of the metal fingers gets smaller. It is possible to place both electrodes on the backside of the cell to avoid the shadowing loss. A successful structure for wafer-Si solar cells is the *i*nterdigitated *b*ack *c*ontact (IBC) cells, in which both electrodes of the cell are placed on the backside. The best efficiency of this cell is 24.2 % on a commercial cell, not far below the record 25.0 % efficiency on a research cell.

3.3.2 Recombination Losses

The absorption of each photon generates an excited electron and a vacant state in the absorber. They have to be separated and extracted by their respective electrodes to generate an electric power output. Recombination is a loss mechanism in which an excited electron falls back into a vacant state before they reach their respective electrodes. Recombination is much better understood for inorganic

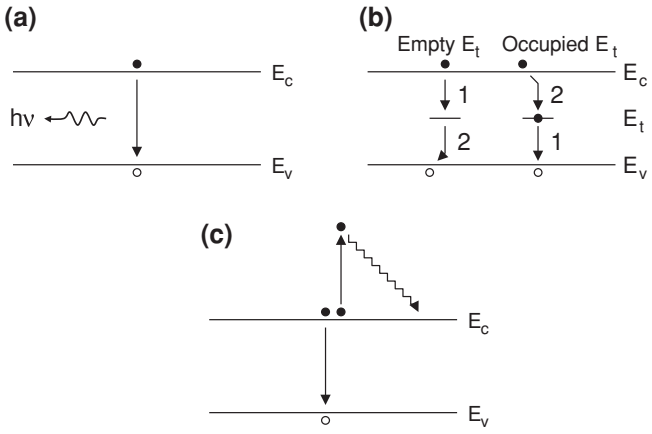

Fig. 3.12 Recombination pathways in inorganic semiconductors. **a** Band-to-band recombination. **b** Recombination through defects: (*left*) an electron can fall onto an unoccupied defect state in the bandgap and then recombines with a hole, or (*right*) a hole can recombine with an occupied defect state in the bandgap and then another electron falls onto the defect state. **c** Auger recombination

semiconductors than organic semiconductors. There are several pathways for recombination in inorganic semiconductors, which are illustrated in Fig. 3.12:

1. Band-to-band recombination: An electron in the conduction band directly recombines with a hole in the valence band, resulting in annihilation of an electron-hole pair.
2. Recombination through defects: An electron (or a hole) first falls onto a defect state within the bandgap of a semiconductor and then recombines with a hole (or an electron)
3. Auger recombination: When an electron and a hole recombine, the energy released excites another electron (or hole) into a higher-energy state.

When an electron in the conduction band directly recombines with a hole in the valence band, it releases a photon with energy equal to the bandgap of the semiconductor as required by energy conservation (Fig. 3.12a). This band-to-band recombination is more common in direct bandgap semiconductors such as CdTe. The direct bandgap not only increases the chances for photon absorption exciting electrons from the valence band to the conduction band, but also the chances for the reverse process, i.e. recombination of electrons from the conduction band with holes from the valence band. This is because the recombination of an electron-hole pair and subsequent generation of a photon in a direct bandgap semiconductor always preserve the momentum of the system. In indirect bandgap semiconductors such as Si, an electron at the minimum of the conduction band has a different momentum from a hole at the maximum of the valence band (Fig. 3.3a). Band-to-band recombination, therefore, requires the involvement of a phonon for momentum conservation, which reduces the chances for band-to-band recombination in indirect bandgap semiconductors. As a result, the lifetime of photo-generated charge carriers,

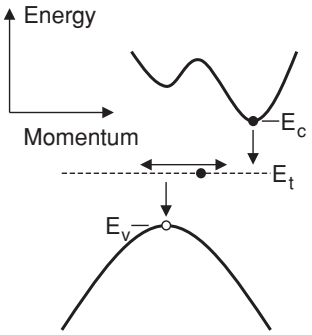

Fig. 3.13 Recombination in indirect bandgap semiconductors through defect states. The momentum of an electron in a defect state E_t is largely undefined as indicated by the width of the defect state. When an electron from the conduction band falls into the defect state and when it further recombines with a hole in the valence band, its momentum is always conserved without any phonon

i.e. the time between their generation and recombination, can be quite long up to several milliseconds in good-quality Si wafers. In direct bandgap semiconductors, the lifetime of photo-generated charge carriers is often in nanosecond or below.

Various structural defects in an inorganic semiconductor crystal often introduce electronic states near the middle of the bandgap in the semiconductor (Fig. 3.12b). These defect states, or more often trap states E_t, can act as stepping stones for recombination. The trap states may be unoccupied or occupied. In case of an unoccupied trap state, an electron in the conduction band can first fall onto such an unoccupied state and turn it into an occupied state. The occupied trap state can then find a hole in the valence band to recombine with. If a trap state is occupied, it has to first recombine with a hole in the valence band and turns itself into an unoccupied state, which can then find an electron in the conduction band to recombine with. Structural defects in a crystal include:

1. Point defects such as impurity atoms, vacancies, and interstitials;
2. One dimensional defects such as dislocations and dislocation loops;
3. Two dimensional defects such as crystal surface and grain boundaries; and
4. Three dimensional defects such as precipitates.

While recombination through defects is present in direct bandgap semiconductors, it is particularly important in indirect bandgap semiconductors such as Si. An electron (or a hole) in a low-dimensional defect is spatially confined. The uncertainty principle of quantum physics suggests that its momentum is thus largely undefined. This significantly increases the chances of recombination in indirect bandgap semiconductors, as illustrated in Fig. 3.13. When an electron in an indirect bandgap semiconductor falls onto a spatially-confined defect state, it does not require a phonon. When the electron further recombines with a hole in the valence band, momentum conservation is again observed without a phonon. Even though the electron and the hole have different momenta to begin with, they recombine through a defect without the involvement of any phonon. Minimizing

defect densities in inorganic semiconductors is critical to increase the lifetime and diffusion length of photo-generated charge carriers. A good-quality crystal improves the chances for photo-generated charge carriers to reach their respective electrodes, and thus the cell efficiency.

Several defects are well recognized as responsible for recombination in wafer-Si solar cells. Among them are surface states. Surface atoms have unsaturated dangling bonds. They introduce surface states within the bandgap of Si, resulting in surface recombination. Surface passivation is a term used for techniques which reduce surface recombination, although there are multiple mechanisms for surface passivation. A common mechanism for surface passivation is to terminate surface dangling bonds with a layer of a dielectric material or a wide-bandgap semiconductor. A good example of this mechanism is thermal oxidation of Si surface to form a silicon dioxide (SiO_2) layer, which effectively eliminates surface states on both n-type and p-type Si. A layer of amorphous Si, which has a bandgap of 1.75 eV, is used to passivate both n-type and p-type Si in the *h*eterojunction *i*ntrinsic *t*hin-layer (HIT) cells. The efficiency record for commercial HIT cells is 24.7 % (Fig. 2.1). The most common, although less effective, passivation material in commercial wafer-Si solar cells today is hydrogenated SiN_x as shown in Fig. 3.1a. The SiN_x layer serves the dual purposes of antireflection and surface passivation, and it works only on n-type Si for surface passivation. In all these cases the passivation layer terminates, to various degrees, the dangling bonds on Si surface.

It is interesting to see where photons of different energies are absorbed in wafer-Si solar cells. As implied in Fig. 3.3a, photons with energies just slightly larger than the bandgap of Si have smaller absorption coefficients, and photons with energies way above the bandgap of Si have larger absorption coefficients. High-energy photons can excite electrons from the valence band into the second minimum of the conduction band, which requires no phonon. High-energy photons with their large absorption coefficients are more likely absorbed near the top of the wafer, i.e. near the emitter (Fig. 3.1a), and low-energy photons are more likely absorbed towards the bottom of the wafer, i.e. in the base. When recombination in the emitter and on the front surface is minimized, the conversion efficiency of high-energy photons, or the 'blue' response of the cell, is improved. When recombination in the base and on the back surface is minimized, the conversion efficiency of low-energy photons, or the 'red' response of the cell, is improved.

Under a metal electrode, recombination becomes more complicated. Besides dangling bonds on the Si side, the wave functions of electrons on the metal side extend into the Si side and introduce additional electronic states within the bandgap of Si. They are termed metal-induced gap states which contribute to recombination under metal-contacted areas. The common method to reduce recombination under a metal contact is to repel one type of charge carriers, either electrons or holes, from the contact region. This is usually realized by heavily doping the region under a metal contact. The mass action law states:

$$np = n_i^2$$

where n and p are the electron and hole concentrations in the semiconductor and n_i is the intrinsic carrier concentration of the semiconductor. At a given temperature

n_i is a fixed quantity for a given semiconductor. When the concentration of electrons is increased by doping, the hole concentration is decreased, and vice versa. As recombination requires an electron-hole pair, eliminating one type of charge carriers by heavy doping reduces recombination under metal contacts.

Transition metals such as copper (Cu) and iron introduce electronic states deep into the bandgap of Si and significantly reduce the lifetime of photo-generated charge carriers. Si wafers for solar cells usually have these impurities in the sub-ppm range, but the fabrication processes may introduce metallic impurities due to unintentional contamination. One example is the conveyor belt furnace for phosphorus diffusion, which forms the p-n junction in wafer-Si solar cells. A major advantage of a conveyor belt furnace over a quartz tube furnace for diffusion is the wafer-to-wafer uniformity, as each wafer in a belt furnace goes through the same temperature ramps. In a tube furnace, there are temperature and dopant concentration variations along the tube. The temperature variation is due to injection of cold gas from the front end and heat dissipation from both ends of the tube, while the dopant variation is due to more depletion of the dopant further away from the injection point. A major concern with the belt furnace is the metallic conveyor belt, which typically contains iron and chromium (Cr). At the temperature of diffusion, which is around 900 °C, Si wafers in contact with the metallic belt are readily contaminated by Fe and Cr from the belt. There is a trend in the industry to employ a ceramic wafer transport system, which introduces less metallic contamination at elevated temperatures.

When an electron in the conduction band recombines directly with a hole in the valence band, the energy released (which is equal to the bandgap) can excite another electron in the conduction band to a higher-energy state (Fig. 3.12c). The excited electron will quickly lose all of its excess energy through multiple steps of relaxation and come down to the minimum of the conduction band. The same can happen to a hole: the energy released through band-to-band recombination can also excite a hole into a higher-energy state, which will eventually relax and come to the maximum of the valence band. This is called Auger recombination and requires a very high electron (or hole) concentration in the semiconductor, which is typically not the case in solar cells.

Recombination in organic semiconductors takes place largely by the reverse process of photon absorption, i.e. an electron in an excited state falls back to a vacant state and in the process releases a photon (Fig. 3.14). The lifetime of an excited electron is very short, typically below a nanosecond, in organic semiconductors. This necessitates immediate separation of photo-excited charge carriers as soon as they are produced, either through an organic/inorganic or organic/organic interface (Fig. 3.6). The thickness of the absorber layer is thus limited to a few nanometers, as photo-excited charge carriers may not survive a thicker absorber before reaching the interface.

3.3.3 Resistive Losses

Figure 3.15 illustrates the path and direction of the electron flow in a wafer-Si solar cell. The current flows vertically in the base but horizontally in the emitter. The fingers collect currents from different regions of the cell and the busbars collect

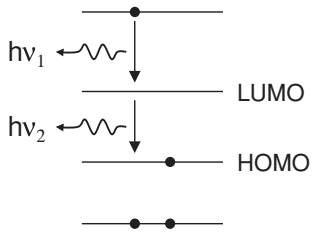

Fig. 3.14 Recombination in organic semiconductors. The excited electron can fall back into either of the two vacant states below. The figure shows a two-step relaxation process in which the electron falls into the LUMO first and then further into the available HOMO, emitting two photons in the process. The excited electron can also fall directly into the available HOMO emitting only one photon

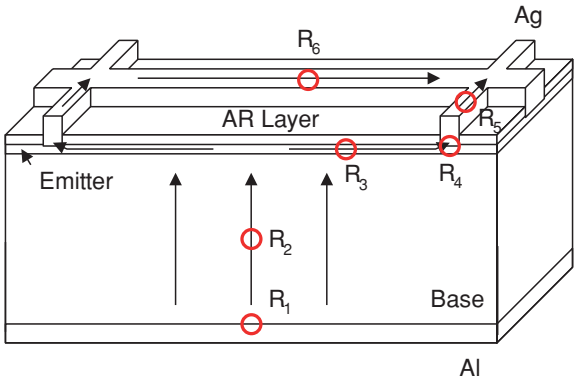

Fig. 3.15 Path and direction of the electron flow in a wafer-Si solar cell. The direction of the electron flow is the opposite of the electrical current. The current flows vertically in the base but horizontally in the emitter. Various resistances are labeled with circles, including emitter resistance R_3, front contact resistance R_4, finger resistance R_5, and busbar resistance R_6

currents from all the fingers. There are resistances in the current path which convert part of the electric power into heat:

1. The back Al/Si contact resistance R_1;
2. The base resistance R_2;
3. The emitter resistance R_3;
4. The front Ag/Si contact resistance R_4;
5. The finger resistance R_5; and
6. The busbar resistance R_6.

Resistance is proportional to the length and inversely proportional to the cross section of the conductor. The direction of the current in Fig. 3.15 indicates that the back contact resistance R_1 and base resistance R_2 are small compared to other resistances, as the cross section of R_1 and R_2 is large, basically the size of the wafer. This can be verified by a quantitative analysis. The remaining four resistances, emitter resistance R_3, front contact resistance R_4, finger resistance R_5, and busbar

resistance R_6, often dominate the resistive losses in wafer-Si solar cells. Three out of the four resistances, emitter resistance R_3, finger resistance R_5, and busbar resistance R_6, are design parameters in solar cells. If possible, the cell should be designed in a way that the losses due to these three resistances are roughly the same, which produces the most efficient cell.

The design of the fingers and busbars is a compromise between shadowing losses and resistive losses. Once the thickness is fixed, the widths of the fingers and busbars determine the finger resistance R_5 and busbar resistance R_6. Wider fingers and busbars reduce the resistances but block more sunlight. Narrower fingers and busbars reduce shadowing losses but increase resistive losses. The metal used for fingers and busbars, Ag, has the lowest resistivity among all the metals on this planet, and it is unlikely that a lower-resistivity substitute for Ag can be found. As discussed in Chap. 6 of this book, Ag will likely be replaced by an Earth-abundant metal in the near future, but those metal candidates all have higher resistivities than Ag.

The current manufacturing process for metallization is screen printing, which produces Ag fingers of about 180 μm wide and about 25 μm thick, i.e. an aspect ratio of about 0.3. One approach around the tradeoff between resistive losses and shadowing losses is to increase the aspect ratios of the fingers and busbars, which allows narrower fingers and busbars with the same cross sections. Screen printing has largely reached its full potential in achieving high aspect ratios in fingers and busbars, and a new cost-effective metallization technique is required for higher aspect ratios. Another approach around this tradeoff is to reduce the porosity of the metal fingers and busbars. The Ag paste in wafer-Si cells is made of Ag nanoparticles, which forms a porous Ag layer after proper processing. The resistivity of the porous Ag layer is roughly 10 times higher than bulk Ag. A new cost-effective technique for metallization, such as electroplating, is required for denser fingers and busbars. It will be discussed in Chap. 6 of this book that electroplating for metallization will likely come with a new metal, either Cu or Al, to replace Ag in wafer-Si solar cells. A third approach to bypass the tradeoff is to place both electrodes on the backside of a cell, as in the interdigitated back contact cells discussed above.

When wafer-Si solar cells are packaged into a module, Cu strips are soldered onto the busbars of each cell. This significantly reduces the resistive losses in the busbars, and thus the finger losses become important. The effective finger resistance is found to be [4]:

$$R_5 = \frac{\rho L}{3tw}$$

where ρ, L, t, and w are the resistivity, length, thickness, and width of the finger, respectively. It is noted that the finger resistivity ρ is not the same as but roughly 10 times higher than the bulk Ag resistivity. The above equation can also be used to estimate the effective resistance of the busbars, as long as the electrical current is extracted from an edge of the solar cell and no Cu strips are soldered to the busbars.

For the wafer-Si solar cell in Fig. 3.1a, the typical doping level for the n-type emitter is low 10^{19} cm^{-3} and the typical thickness of the emitter is about 0.5 μm. This doping level is much higher than that of the p-type base, which is in low

10^{16} cm^{-3}. There is a tradeoff between resistive losses and recombination losses in the emitter. The high doping level in the emitter significantly reduces the lifetime and diffusion length of photo-generated charge carriers, resulting in high recombination losses in the emitter. Increasing the emitter thickness simply widens the high recombination region leading to even higher recombination losses. The recombination losses can be minimized by employing a thinner emitter with a lower doping level. As shown in Fig. 3.15, a thinner emitter reduces the cross section for the horizontal emitter current, and a lower doping level leads to a higher emitter resistance. Both result in higher resistive losses in the emitter. 10^{19} cm^{-3} doping and 0.5 μm thickness are optimized emitter parameters.

Another critical parameter in solar cell design is the finger spacing, which is again a compromise between shadowing losses and resistive losses. As shown in Fig. 3.15, a larger spacing between fingers increases resistive losses in the emitter. A smaller spacing between fingers adds more fingers to the cell, thus more shadowing losses. The increased shadowing losses can be partially offset by narrower fingers, if a cost-effective metallization technique for narrower fingers is ready for the stage. The effective resistance of the emitter is given by [4]:

$$R_3 = \frac{\rho_e S}{6 L t_e}$$

where ρ_e and t_e are the resistivity and thickness of the emitter, and S and L are the spacing and length of the fingers.

The contact resistance between a metal and a semiconductor is determined primarily by two factors: the Schottky barrier height as well as the doping level. Due to surface states, the Fermi level of a semiconductor surface is often pinned to roughly the middle of the bandgap. The Schottky barrier height between a semiconductor and any metal, irrespective of its work function, is thus about half of the bandgap. Schottky barrier heights for various metals on n-type and p-type Si have been experimentally found to be between 0.4 and 0.9 eV, while half of the bandgap is 0.56 eV. For this reason, any metal/semiconductor contact in solar cells today is actually a Schottky junction with a high doping level, i.e. it is a quasi-Ohmic contact. The high doping level narrows the width of the Schottky barrier such that quantum tunneling of charge carriers takes place with sufficient probabilities through the Schottky barrier. The current-voltage relation for such a quasi-Ohmic contact is linear.

With a metal on a heavily-doped semiconductor, the specific contact resistance in Ω-cm^2 is given by [5]:

$$R_c \sim \exp\left(\frac{4\pi\phi_B}{h}\sqrt{\frac{\varepsilon_s m^*}{N}}\right)$$

where ϕ_B is the Schottky barrier height between metal and semiconductor, ε_s the permittivity of the semiconductor, m^* the effective mass of the charge carriers, N the doping level, and h the Planck constant. It is noted that the doping level in the emitter of a solar cell is often determined by considerations other than the contact resistance, such as resistive and recombination losses. Therefore, reducing the

contact resistance by increasing the doping level is not always an option. On the other hand, reducing the Schottky barrier height is an alternative and effective approach to reduce contact resistance. This requires unpinning of the Fermi level on the semiconductor surface, such that the Schottky barrier height varies with the work function of the metal [6].

3.4 Solar Cell Parameters

The two often-cited performance parameters for solar photovoltaics are cost and efficiency. Several methods for calculating the cost of solar photovoltaics are discussed in Chap. 2. The efficiencies of best laboratory solar cells are presented in Fig. 2.1. Other important parameters for solar cells include short-circuit current J_{sc}, open-circuit voltage V_{oc}, fill factor FF, current at maximum power J_m, voltage at maximum power V_m, series resistance R_s, and shunt resistance R_{sh}.

The current-voltage relation of an ideal p-n junction solar cell is given by:

$$J = J_{ph} - J_s\left[exp\left(\frac{qV}{kT}\right) - 1\right]$$

where J is the current of the cell, J_{ph} the photocurrent, J_s the reverse saturation current, q the electron charge, V the voltage, k the Boltzmann constant, and T the absolute temperature. The expression for J_s varies depending on the structure of the p-n junction and the diffusion lengths of minority carriers. For the solar cell in Fig. 3.1a with a narrow n-type emitter and a wide p-type base, J_s is given by:

$$J_s = q\left(\frac{D_p p_{no}}{t_e} + \frac{D_n n_{po}}{L_n}\right)$$

where D_p and D_n are the diffusion coefficients of holes in n-type Si and electrons in p-type Si, p_{no} and n_{po} are the equilibrium concentrations of holes in n-type Si and electrons in p-type Si, L_n is the diffusion length of electrons in p-type Si, and t_e is the emitter thickness.

Figure 3.16 schematically illustrates the current-voltage relation of a solar cell, which defines some of the solar cell parameters. Short-circuit current J_{sc} is the current of the cell when the voltage across the cell is zero. Open-circuit voltage V_{oc} is the voltage of the cell when its current is zero. They are marked in Fig. 3.16.

To extract maximum power out of a solar cell, we have to find the maximum power point in Fig. 3.16. This is done by taking the product of current and voltage in the figure and plotting the product, which is the output power of the cell, as a function of its voltage. Once the maximum power point is found, the efficiency of the cell is defined as the ratio between maximum electric power output and incident solar power. In Fig. 3.16, the maximum power point is labeled P_{max}, and the current and voltage at maximum power are labeled J_m and V_m. The fill factor of the cell is defined as:

$$FF = \frac{P_{max}}{J_{sc}V_{oc}} = \frac{J_m V_m}{J_{sc}V_{oc}}$$

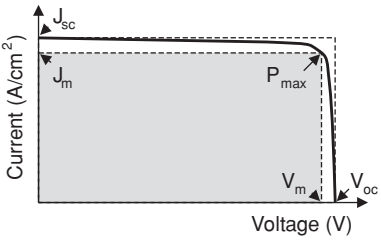

Fig. 3.16 Current-voltage relation of a solar cell. Efficiency is calculated at maximum electric power output P_{max}. Short-circuit current J_{sc}, open-circuit voltage V_{oc}, current at maximum power J_m, and voltage at maximum power V_m are marked in the figure. Fill factor FF is the ratio between the shaded rectangle and the open rectangle

It is the ratio between the shaded rectangle defined by J_m and V_m over the open rectangle defined by J_{sc} and V_{oc} in Fig. 3.16. This is a measure of the squareness of the current-voltage relation of a solar cell. The efficiency can be defined in terms of J_{sc}, V_{oc}, and FF as:

$$\eta = \frac{FF \times J_{sc} \times V_{oc}}{Incident\ Solar\ Power}$$

An efficient solar cell requires a large fill factor, a large short-circuit current, and a large open-circuit voltage.

For an ideal p-n junction solar cell, its parameters can be found from its current-voltage relation above. When a solar cell is short circuited, its voltage is zero leading to $J_{sc} = J_{ph}$, i.e. the short-circuit current is equal to the photocurrent. When a solar cell is an open circuit, its current is zero leading to:

$$V_{oc} = \frac{kT}{q} ln\left(\frac{J_{ph}}{J_s} + 1\right)$$

These relations reveal the keys to a larger short-circuit current and a large open-circuit voltage in a solar cell, i.e. maximizing the photocurrent J_{ph} and minimizing the reverse saturation current J_s. They require reduction of all the optical losses discussed in Sect. 3.3.1 and all the recombination losses in Sect. 3.3.2.

The current-voltage relation of a real, non-ideal p-n junction solar cell is given by:

$$J = J_{ph} - J_s\left\{exp\left[\frac{q(V + JR_s)}{nkT}\right] - 1\right\} - \frac{V + JR_s}{R_{sh}}$$

where R_s and R_{sh} are the series resistance and shunt resistance of the cell, and n is the ideality factor of the p-n junction. The series resistance R_s is the sum of all the resistances discussed in Sect. 3.3.3. The shunt resistance R_{sh} represents the internal leakage current between the two electrodes of the cell, which is caused by improper fabrication or faulty structure of the cell. For example, if the p-n junction of a cell is exposed to a surface and the surface is not properly passivated, a leakage current can flow between the two electrodes along the surface through surface

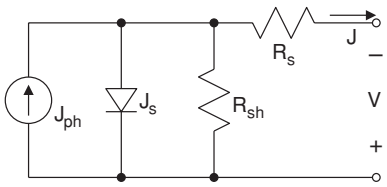

Fig. 3.17 Equivalent circuit for a real, non-ideal p-n junction solar cell. To minimize resistive losses, the series resistance R_s is ideally reduced to zero and the shunt resistance R_{sh} is ideally increased to infinity. Optical and recombination losses are embedded into the photocurrent J_{ph} and reverse saturation current J_s

states. The ideality factor n takes a value between 1 and 2, depending on the dominant recombination mechanism in the p-n junction. Figure 3.17 is the equivalent circuit for a non-ideal p-n junction solar cell. To minimize the resistive losses of the cell, the series resistance R_s is ideally reduced to zero and the shunt resistance R_{sh} is ideally increased to infinity. Optical and recombination losses are embedded in the photocurrent J_{ph} and reverse saturation current J_s.

References

1. Lussem B, Riede M, Leo K (2013) Doping of organic semiconductors. Phys Status Solidi A 210:9–43
2. Shockley W, Queisser HJ (1961) Detailed balance limit of efficiency of pn junction solar cells. J Appl Phys 32:510–519
3. Henry CH (1980) Limiting efficiencies of ideal single and multiple energy gap terrestrial solar cells. J Appl Phys 51:4494–4500
4. Goetzberger A, Knobloch J, Voss B (1998) Crystalline silicon solar cells. Wiley, Chichester
5. Sze SM (1981) Physics of semiconductor devices, 2nd edn. Wiley, New York
6. Tao M, Udeshi D, Basit N, Maldonado E, Kirk WP (2003) Removal of dangling bonds and surface states on Si (001) surface by a monolayer of Se. Appl Phys Lett 82:1559–1561

Chapter 4
Manufacturing of Wafer-Si Solar Cells and Modules

In this chapter the current manufacturing processes for wafer-Si solar cells and modules are explained including monocrystalline Si and multicrystalline Si, as they are the most popular cell technologies on the market with a 90 % combined market share. The discussion will start from quartz reduction through module fabrication. Understanding the manufacturing processes for wafer-Si cells and modules also helps grasp some of the roadblocks and bottlenecks to terawatt-scale deployment of solar photovoltaics. Several critical research directions for solar photovoltaics are identified based on the discussions in this chapter and Chap. 3, such as solution-based fabrication of chalcogenide solar cells and efficiency uniformization in wafer-Si cell and module manufacturing.

Figure 4.1 shows a current industrial process flow to manufacture monocrystalline-Si cells and modules. It involves quartz (SiO_2) reduction, conversion of metallurgical-grade Si to trichlorosilane ($SiHCl_3$), purification of $SiHCl_3$, reduction of $SiHCl_3$ to polycrystalline Si, growth of monocrystalline-Si ingot, wafering of ingot, cell fabrication, and module fabrication. The electricity inputs for the most energy-intensive steps are labeled in the figure [1].

4.1 Polycrystalline-Si Feedstock

While it is often said that Si comes from sand, quartz is actually the raw material for wafer-Si solar cells due to its higher purity over sand. It is reduced to Si in an electric-arc furnace with carbon, in the form of charcoal or coke, at about 1,900 °C:

$$SiO_2(s) + C(s) \rightarrow Si(l) + CO_2(g)$$

The Si produced at this temperature is a melt, which cools down to form metallurgical-grade Si. Depending on the purity of the raw materials, the purity of the resultant metallurgical-grade Si is at best 99 % which is insufficient for solar cells. The energy input for this step is about 20 kWh/kg, i.e. 20 kWh of electricity for each kilogram of metallurgical-grade Si produced. In 2012, the global production

M. Tao, *Terawatt Solar Photovoltaics*, SpringerBriefs in Applied Sciences and Technology, DOI: 10.1007/978-1-4471-5643-7_4, © The Author(s) 2014

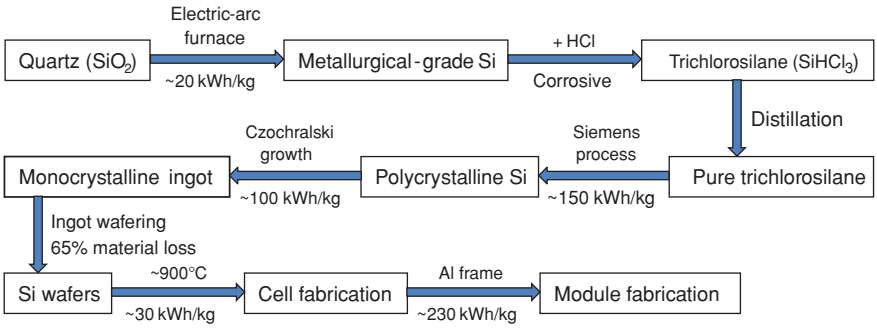

Fig. 4.1 A current industrial process flow for monocrystalline-Si cells and modules. The energy inputs for the most energy-intensive steps are indicated [1]. They are expressed in kWh/kg of Si processed. Purification of metallurgical-grade Si is realized by converting it into $SiHCl_3$ for distillation

of metallurgical-grade Si is about 1,500,000 metric tons/year [2], which releases roughly 10,000,000 metric tons of CO_2 into the atmosphere (The reaction above generates close to 7 kg of CO_2 for 1 kg of Si produced). There is additional CO_2 emission from the generation of the 20 kWh electricity, which is not included in the CO_2 number above.

A small fraction of the metallurgical-grade Si, about 20 %, is purified to produce ultrapure Si for the solar cell and semiconductor industries. The required impurity levels for semiconductor-grade Si are typically below 0.1 ppm or the purity of semiconductor-grade Si is above 99.9999999 %, i.e. 9 N's. It is widely believed that the required impurity levels for solar-grade Si are less stringent than semiconductor-grade Si, typically below 1 ppm or above 99.9999 % (6 N's). To purify metallurgical-grade Si, the most common industrial process today is through $SiHCl_3$, which is formed by reacting metallurgical-grade Si with hydrogen chloride (HCl):

$$\mathrm{Si(s) + 3HCl(g) \rightarrow SiHCl_3(g) + H_2(g)}$$

The reaction above is accompanied by the formation of other chlorosilanes such as tetrachlorosilane ($SiCl_4$), as they are allowed by the thermodynamics of the system. There are no large-scale industrial applications for $SiCl_4$, so it has to be collected and converted to $SiHCl_3$ for a sustainable solar cell industry.

The boiling point of $SiHCl_3$ is 31.8 °C, allowing room-temperature distillation for its purification. Multiple-step distillation is typically carried out to achieve semiconductor-grade Si with 9 N's purity, as impurities with boiling points close to that of $SiHCl_3$ are harder to remove and require multiple steps to bring their levels to the targets. Both the evaporation and condensation temperatures are tightly controlled in each step for this purpose. In addition, the corrosive HCl and $SiHCl_3$ attack stainless steel, resulting in periodic replacement of the distillation equipment and adding to the cost.

The purified $SiHCl_3$ is then reduced to ultrapure polycrystalline Si by hydrogen (H_2) in the so-called Siemens process. This reaction takes place on ultrapure Si

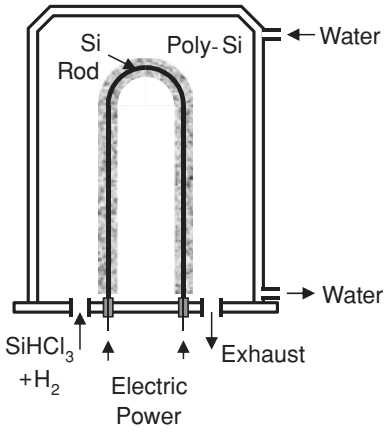

Fig. 4.2 Schematic of a Siemens reactor for the reduction of $SiHCl_3$ to ultrapure polycrystalline Si. The power required to maintain the Si rod at 1,150 °C increases quadratically with time, and most of the power is ultimately converted to hot water. The water-cooled wall is to minimize formation of Si powder in the gas phase and on the wall of the reactor

rods which are maintained at 1,150 °C by passing an electrical current through it, and the overall reaction on the Si rods is:

$$SiHCl_3(g) + H_2(g) \rightarrow Si(s) + 3HCl(g)$$

This turns out to be one of the most energy-intensive steps in the entire process flow from quartz to modules at about 150 kWh/kg of polycrystalline Si produced. Figure 4.2 illustrates schematically a Siemens reactor. $SiHCl_3$ and H_2 are mixed and fed into the reactor. They react on the hot Si rod according to the overall reaction above, depositing Si onto the rod. As the diameter of the rod increases linearly with time, the power required to maintain the rod at 1,150 °C increases quadratically with time. The Siemens reactor is a cold-wall reactor, in which the wall is water-cooled to less than 100 °C. This minimizes the formation of Si powder in the gas phase and on the wall of the reactor, which is hard to process in subsequent steps. At the same time, most of the electric power is converted into hot water and wasted. When done, the Si rod is smashed into small pieces which are the feedstock for the solar cell industry.

The purity of the polycrystalline Si produced by the Siemens process above can reach 9 N's, exceeding the required purity for solar-grade Si. As the $SiHCl_3$/Siemens process is costly and energy-intensive, there have been extensive efforts in the last 10 years to develop alternative purification techniques for metallurgical-grade Si which produce less pure solar-grade Si at significantly lower cost and energy input [3]. These efforts can be grouped into three categories:

1. Purer raw materials: These include purer quartz and purer coke. This also includes pretreatment, such as leaching, of the raw materials to remove certain impurities.
2. Impurity segregation: This involves alloying impure Si with a metal such as Al. Many impurities tend to segregate into the alloy phase leaving behind a purer Si phase.
3. Treatment of molten Si: This includes vacuum or a reactive ambient over, or bubbling a gas through, or adding a reactant to the Si melt to remove certain impurities from Si.

Although there have been claims of success, none of these alternative processes has really been adopted by the solar cell industry. One common limitation of these alternative processes is that they are effective for only a few, but not all the impurities in metallurgical-grade Si. This is because they do not rely on a common property every impurity has for purification. In distillation, we rely on a common property of all the impurities, i.e. the boiling point of the impurities, which enables controlled evaporation and condensation of all the impurities for their removal. It is suggested that a new purification technique to replace $SiHCl_3$ distillation will have to rely on a different but common property of all the impurities, such as the redox potential of all the impurities.

4.2 Monocrystalline-Si Wafers

The ultrapure polycrystalline Si produced is converted into monocrystalline ingots in the Czochralski process. Polycrystalline-Si pieces are loaded into a crucible made of high-purity quartz. A measured amount of a dopant, typically boron, is added along with polycrystalline Si. The target resistivity of the ingot is around 1 Ω-cm, which requires about 1×10^{16} cm^{-3} of boron. The crucible is heated above the melting point of Si, 1,420 °C, in an inert ambient such as argon. A small Si seed crystal is brought into contact with the Si melt in the crucible and then pulled up slowly. With the temperature tightly controlled, melt Si crystallizes on the seed crystal. The seed has a (100) orientation to ensure that the crystal growth is along the (100) direction. The seed is rotated, resulting in a cylindrical ingot of monocrystalline Si. The Si melt corrodes the quartz crucible, dissolving oxygen into the melt and then the ingot. The oxygen concentration in Czochralski ingots is typically at its solid solubility, about 2×10^{18} cm^{-3}, which degrades the efficiency of the cell due to recombination through a boron-oxygen complex in Si. This is one of the reasons for an industrial push to switch from p-type wafer-Si solar cells as shown in Fig. 3.1a to n-type cells, in which the wafer, and thus the base, is n-type. The energy input for the Czochralski process is about 100 kWh/kg of Si ingot produced. This is another energy-intensive step in the entire process flow from quartz to modules.

The monocrystalline-Si ingot has a cylindrical shape. The top and bottom of the ingot are more defective. They are cut off the ingot and then the ingot is cut into a quasi-square shape, resulting in about 25 % material loss. The quasi-square shape allows closer packing of the wafers in the module, as shown in Fig. 4.3. Circular wafers would create more dead space between wafers which does not generate electricity. For recycling, the cut-off material is usually cleaned and loaded into another crucible in the Czochralski process for a new ingot. The whole quasi-square ingot is then sliced into wafers in one step with a multiple-wire diamond saw. As the ingot grows along the (100) direction, the wafers have a (100) surface. Si is a hard material, so the slicing is very slow taking many hours to cut through one ingot. Slicing remains one of the most costly steps in Si wafer manufacturing due to its low throughput.

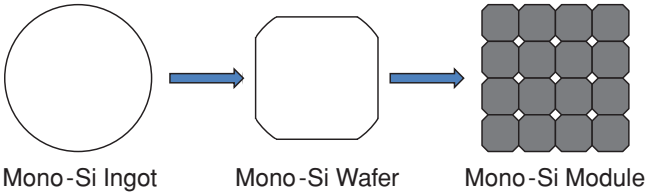

Fig. 4.3 Monocrystalline-Si ingots to modules. The circular ingot is first cut into a quasi-square shape, which is then sliced into quasi-square wafers. The quasi-square wafers allow closer packing in the module. The space between wafers does not generate electricity

Finally, the monocrystalline-Si wafers are etched to remove saw damage and cleaned for cell fabrication. The thickness of the monocystalline-Si wafers after saw damage removal is between 180 and 200 μm. There is a significant material loss in the sawing step. The smallest diameter of the saw wire is 120 μm, resulting in a kerf of about 150 μm wide and turning that Si into saw dust. Saw damage removal takes away another 50 μm or so off Si. The material loss from saw dust and damage removal is about 55 %. This material loss is hard to recycle as the Si waste is either dust mixed with saw slurry or dissolved in a solution. The overall material loss between as-grown ingot and wafers is about 65 %. The high material loss drives up the energy input for monocrystalline-Si wafers to over 1,000 kWh/kg of Si wafers, which will be discussed in Sect. 5.4.

Si wafers currently account for about 40 % of the overall module cost (Fig. 2.5). This is in sharp contrast to the semiconductor industry in which the cost of Si wafers is negligible at only about 1 % of the chip cost. There have been industrial efforts to reduce Si material consumption in solar cells. The current consumption rate of polycrystalline Si is about 7 g/W_p, i.e. it takes 7 g of polycrystalline Si to produce 1 W_p of wafer-Si cells. The Si consumption rate can be reduced by using thinner wafers. The downside of thinner wafers is the poor mechanical strength of the wafers, which increases wafer breakage during cell and module manufacturing leading to lower yields. Advanced wafer handling capabilities can be developed for these thin wafers, but the manufacturing cost would go up accordingly. The thickness of Si wafers in the solar cell industry has been stable for several years now at 180–200 μm. On the other hand, the Si consumption rate can also be reduced by using thinner saw wires which produce narrower kerfs. Wires down to 100 μm diameter have been tested, but further thinning the wire causes frequent fracture of the wire. Innovations are needed here to develop a new ingot slicing technique which is fast and kerfless, i.e. less Si waste.

4.3 Wafer-Si Cells and Modules

The monocrystalline-Si wafers shipped to cell manufacturers are typically 125 × 125 mm^2 quasi-square shaped with a thickness between 180 and 200 μm. They are (100)-oriented and p-type boron-doped with a resistivity of about 1 Ω-cm.

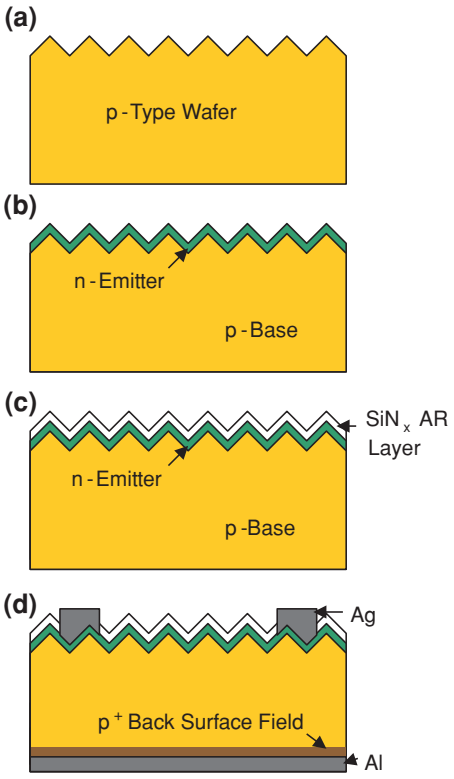

Fig. 4.4 A common process flow for the wafer-Si solar cell depicted in Fig. 3.1a. The major steps include **a** wafer cleaning and texturing, **b** diffusion of n-type emitter, **c** deposition of SiN_x antireflection layer, and **d** screen printing and firing for front and back electrodes. The figures are not drawn to scale, and surface texture on the backside is not shown

Figure 4.4 schematically illustrates a common process flow to manufacture wafer-Si solar cells from monocrystalline-Si wafers. It involves four major steps: wafer cleaning and texturing, diffusion of phosphorus to form n-type emitter, deposition of SiN_x antireflection layer, and screen printing and firing for front and back electrodes. Each of the steps is discussed in more details below.

Throughput in wafers/hour is extremely high in solar cell manufacturing. A 30 MW_p/year line runs over 1,000 wafers/hour, which is far beyond the throughput of a semiconductor fab and requires special equipment to accomplish. Today the solar cell industry has developed its own low-cost high-throughput processes and equipment which are distinctively different from the semiconductor industry.

As-received monocrystalline-Si(100) wafers are immersed into a heated aqueous solution of NaOH for surface cleaning and texturing. NaOH etches Si(100) wafers anisotropically, i.e. it etches the (100) surface much faster than the (111) surface resulting in pyramids of random sizes on the Si(100) wafer. The facets of the pyramids have a (111) orientation, and the base of the pyramids varies between 1 and 10 μm in dimension. The pyramidal texture reduces surface reflection by second chance of incidence (Fig. 3.10). When a layer of material is etched off the surface during texturing, all the surface contaminants are removed from the surface and a fresh clean surface is exposed. It is noted that surface texture on the backside of the wafer is not shown in Fig. 4.4.

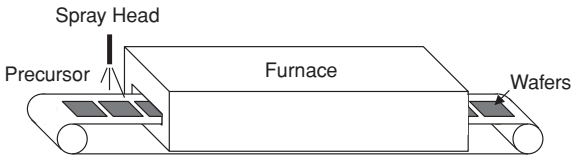

Fig. 4.5 Schematic of a conveyor belt furnace. Wafers are loaded onto and unloaded from the conveyor belt by robots. A liquid phosphorus precursor is sprayed onto each wafer before it enters the furnace. The furnace temperature is set around 900 °C, and it usually takes about 20 min to for wafers to move from one end of the furnace to the other

The next step in cell fabrication is diffusion of phosphorus into the textured Si wafer to form an n-type emitter. There are two diffusion techniques. One is the traditional horizontal quartz tube furnace, which is a batch process. Hundreds of Si wafers are placed vertically in the quartz tube and heated to about 900 °C. The heater is placed outside the quartz tube, so it is a hot-wall reactor. Phosphoryl chloride ($POCl_3$) is introduced into the tube as the phosphorus source, and the diffusion lasts for about 30 min. The emitter has a surface phosphorus concentration of low 10^{19} cm^{-3} and is about 0.5 μm deep, resulting in an emitter sheet resistance of 50–100 □/γ. The other technique for diffusion is the conveyor belt furnace, which is a continuous process (Fig. 4.5). Si wafers are placed on a conveyer belt, and a liquid phosphorus precursor is sprayed onto each wafer. The belt carries the wafers into the furnace, which is set at about 900 °C. It usually takes about 20 min for a wafer to go from one end of the furnace to the other, resulting in a surface phosphorus concentration of low 10^{19} cm^{-3} and an emitter depth of about 0.5 μm. After diffusion, the phosphosilicate glass formed on the wafer surface from either furnace is removed by acid etching. Phosphorus diffusion also occurs along the edges of the wafer, which is removed by reactive ion etching. This step is to confine the emitter to the front surface of the wafer, eliminating a pathway for shunt resistance.

Diffusion is one of the most critical steps in cell fabrication. Tube furnace diffusion is well established, but conveyor furnace diffusion has several advantages. Besides being a continuous process with a higher throughput, conveyor furnace diffusion also provides better wafer-to-wafer uniformity. This is because every wafer goes through the same temperature ramps as it enters and leaves the conveyor furnace. In a tube furnace, wafers at different locations in the tube often experience different temperatures. The cold carrier gas with $POCl_3$ entering the tube gets warmer as it flows further into the tube. Wafers near the gas injection point have lower temperatures than wafers in the middle of the tube, resulting in poor wafer-to-wafer uniformity in terms of surface phosphorus concentration and emitter depth. There are also variations in phosphorus concentration in a tube furnace, as phosphorus is continuously consumed as it flows further into the tube. In a conveyor furnace, each wafer experiences the same concentration of phosphorus as it is sprayed onto each wafer. The main disadvantage of the conveyor furnace is the metallic conveyor belt, which introduces metallic impurities into the wafers. There are ongoing efforts to use a ceramic wafer transport system for reduced metallic contamination in the conveyor furnace.

After diffusion, a SiN_x antireflection layer is deposited on the front surface (the emitter side) of the wafer by plasma-enhanced chemical vapor deposition. The SiN_x layer is around 75 nm thick, targeting 600 nm for destructive interference (Fig. 3.9). Similar to diffusion, there are also two techniques for SiN_x deposition. One is the tube reactor and the other is the conveyor reactor. In the tube reactor hundreds of Si wafers are placed vertically. The tube is pumped to a low pressure, often less than 1 Torr, before plasma deposition of SiN_x. In the conveyor reactor, wafers are continuously brought into the reactor for SiN_x deposition. Although the throughput is higher, the main problem for the conveyor reactor is the lower-index SiN_x it produces. The conveyor reactor is not entirely sealed off from the ambient, resulting in oxygen incorporation into the SiN_x layer. The refractive index of the SiN_x layer depends on its oxygen content, and is lower than the index of oxygen-free SiN_x, 2.0. This results in more reflection in the cell, as the optimum index between glass and Si is 2.34 as discussed in Sect. 3.3.1. TiO_2 may turn out to be a better choice for the antireflection layer on wafer-Si solar cells, as it has an index of 2.6 and can be prepared in air with solution-based processes. A noticeable disadvantage of TiO_2 is that it is a semiconducting material. It can introduce a pathway for leakage current between the two electrodes of the cell if improperly processed, i.e. a pathway for shunt resistance.

Metallization is the next step. Ag paste is screen printed over the SiN_x layer on the front side into a finger shape. A bake at about 200 °C follows to dry the printed Ag paste. Al paste is screen printed on the backside of the wafer, into a blank film. Screen printing of Ag is also performed on small areas on the backside of the wafer. This is for soldering to the backside of the wafer during module fabrication. Another bake at about 200 °C dries the printed Al paste. The wafer then goes through a conveyor furnace set at about 750 °C for about 20 min. The Ag paste contains lead (Pb). Around 750 °C, the Pb in the Ag paste dissociates the SiN_x layer underneath, allowing Ag to penetrate the SiN_x layer and bond directly with the Si wafer below for a quasi-Ohmic contact. On the backside, Al and Si form an eutectic alloy (the eutectic point of Al and Si is 577 °C), which produces heavy Al doping into the Si wafer and creates the back surface field. The Al nanoparticles in the Al paste also fuse together (the melting point of Al is 660 °C) and form a continuous network of Al, which reduces the resistivity of the back electrode.

The final step in cell fabrication is testing and sorting. When cells are connected in series in the module, the output current of the module is limited by the smallest current of all the cells in the series. For this reason only cells with similar efficiencies (within ±0.5 % absolute) are packaged into a module. This requires the measurement of the current-voltage relation for each cell. A high-throughput cell efficiency tester is attached to the end of the metallization line. After testing, cells with similar efficiencies are placed together, ready for module fabrication.

In module fabrication, 60 or 72 cells with similar efficiencies are first soldered into a series with Cu wires. This is done by connecting the front electrode of one cell to the back electrode of the next cell. A glass sheet, an EVA sheet, the connected solar cells, and a back sheet are stacked together. The stack is heated under vacuum to drive out air in the stack, and the thermoplastic EVA laminates the

stack together air-free. Any air trapped in the stack would create a reverse index profile, leading to total reflection of the incident sunlight under certain incident angles (Fig. 3.11). Finally an Al frame is placed around the stack to seal it, and the module is air-tight and moisture-tight. The modules are again tested to determine their current-voltage relations and sorted. This is important as only modules with similar output currents should be connected in series and only modules with similar output voltages should be connected in parallel in a system, to reduce mismatch losses.

The total energy input for fabricating solar cells from Si wafers is estimated at about 30 kWh/kg of Si wafers processed. There are several high-temperature steps in wafer-Si cell fabrication (Fig. 4.4), including phosphorus diffusion at about 900 °C and metallization at about 750 °C. The energy input for module fabrication from cells is high, estimated at about 230 kWh/kg of Si wafers processed. The main contributors to the high energy input in module fabrication are the Al frame and glass sheet. It takes about 12 kg of Al and about 12 kg of glass each to package 1 kg of Si wafers into modules. The energy input for Al is about 15 kWh/kg of Al produced, which translates into about 180 kWh/kg of Si wafers for the Al frame. The energy input for glass is estimated at 3–4 kWh/kg of glass produced, which adds another 40 kWh/kg of Si wafers for the module. It should be noted that although 230 kWh/kg is the largest number for energy input in Fig. 4.1, module fabrication is actually the third most energy-intensive step between quartz and monocrystalline-Si modules. The Siemens process is the most energy-intensive step and the Czochralski process is the second most energy-intensive step in the manufacturing processes of monocrystalline-Si cells and modules. This is because most of the polycrystalline Si feedstock and most of the monocrystalline-Si ingot produced in those steps are turned into saw dust, drastically driving up their actual energy inputs in terms of the weight of the final Si wafers.

4.4 Alternative Processes for Si Wafers

The two most energy-intensive steps between quartz and monocrystalline-Si modules are the Siemens process, which reduces $SiHCl_3$ to polycrystalline Si, and the Czochralski process, which produces monocrystalline-Si ingots (Fig. 4.1). Alternative processes have been developed to replace Siemens and Czochralski processes for the solar cell industry. As shown in Fig. 4.6, directional solidification has largely replaced the Czochralski process and the fluidized-bed process is starting to chip away the market for the Siemens process, with significantly-reduced energy inputs.

Figure 4.7 is a schematic of the directional solidification process. The quartz crucible has a rectangular shape. Polycrystalline Si is loaded into the crucible with a measured amount of a dopant, typically boron. The crucible is heated above the melting point of Si, 1,420 °C, in an inert ambient. The crucible is then gradually pulled out of the hot zone. There is a heat exchange block at the bottom of the

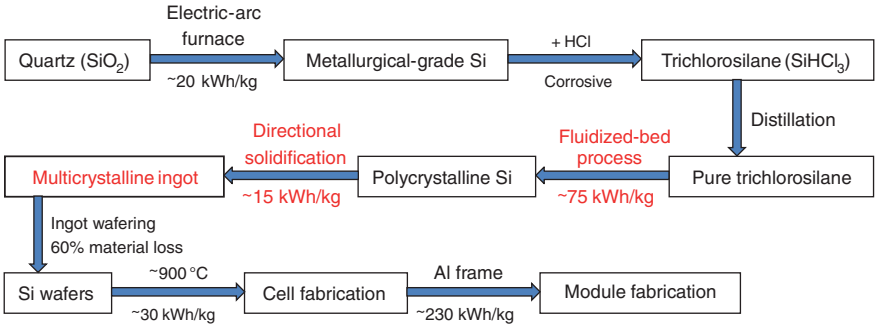

Fig. 4.6 A current industrial process flow for multicrystalline-Si cells and modules. The steps which are replaced from the process flow in Fig. 4.1 include the Siemens process, which can be replaced by the fluidized-bed process, and the Czochralski process, which is largely replaced by the directional solidification process

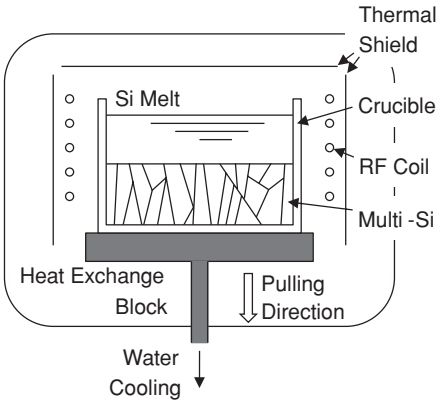

Fig. 4.7 Schematic of the directional solidification process. The bottom of the crucible is pulled out of the hot zone, leading to crystallization of the Si melt at the bottom of the crucible. As the crucible is continuously pulled down and out of the hot zone, the crystals grow from bottom to top in the crucible

crucible which can be water cooled. With the temperature tightly controlled, melt Si at the bottom of the crucible starts to crystallize. The crucible is continuously pulled out of the hot zone, and the crystallization continues from the bottom to the top of the crucible. As there are multiple crystal grains growing at the same time, the resultant material is a multicrystalline-Si ingot, in a rectangular shape. To obtain large crystal grains, the growth is purposely slow taking several days to complete an ingot. On the other hand, the chamber is thermally insulated and the only cooling is at the bottom of the crucible through the heat exchange block. The energy input for directional solidification is significantly lower that of the Czochralski process, at about 15 kWh/kg versus 100 kWh/kg.

During ingot wafering, all the six sides of the rectangular multicrystalline-Si ingot are cut off as they are more defective. This results in about 15 % material loss. The remaining rectangular ingot is cut into square blocks of 156 × 156 mm^2. Each of these blocks is then sliced into square wafers in one step with a multiple-wire diamond saw. The slicing is very slow taking many hours to cut through an ingot, and is one of the most costly steps in Si wafer manufacturing. The square wafers allow the closest packing possible in the module. This provides an easy method to distinguish multicrystalline-Si modules from monocrystalline-Si modules, i.e. multicrystalline-Si modules do not have the white diamond areas as in Fig. 4.3. Finally, the multicrystalline-Si wafers are etched to remove saw damage and cleaned for cell fabrication. The thickness of the multicrystalline-Si wafers after saw damage removal is about 200 μm. The material loss in multicrystalline-Si wafering is lower than monocrystalline-Si wafering but still significant, with the overall material loss between as-grown ingot and wafers at about 60 %.

Surface texturing for multicrystalline-Si wafers is different from monocrystalline-Si(100) wafers. The crystal grains in multicrystalline Si are randomly oriented, preventing effective anisotropic etching of its surface. The most common texturing technique for multicrystalline-Si wafers involves acid etching, which is inferior to the pyramidal texture on monocrystalline-Si(100) wafers in terms of antireflection. The rest of the manufacturing process flow for multicrystalline-Si cells and modules is almost identical to that of monocrystalline-Si cells and modules.

Besides more optical losses, multicrystalline-Si cells also suffer from recombination at grain boundaries which are absent in monocrystalline-Si cells. Overall, the efficiency of commercial multicrystalline-Si cells is 2–5 % absolute lower than monocrystalline-Si cells, but interestingly the industry is willing to trade a little efficiency for a large return in cost. The cost reduction comes partially from the reduced energy input for the directional solidification process from the Czochralski process, 15 kWh/kg versus 100 kWh/kg, i.e. an 85 % reduction in electricity cost. This performance-cost tradeoff highlights the extremely cost sensitive nature of the industry and is seldom found in the semiconductor industry. Today multicrystalline-Si modules have about 60 % of the solar cell market, while monocrystalline-Si modules have less than 30 % of the market.

An alternative for the Siemens process is required to significantly reduce the overall energy input for wafer-Si solar cells, as it is the most energy-intensive step in Fig. 4.1. One alternative process which is chipping away the market share by the Siemens process is the fluidized-bed process, as shown in Fig. 4.6. $SiHCl_3$ and H_2 flow into the fluidized-bed reactor from the bottom. There are Si particles floating in the reactor. $SiHCl_3$ and H_2 react on the Si particles resulting in Si deposition on the particles. When the Si particles grow to a certain size, they can no longer float and will fall to the bottom of the reactor, which are then collected.

A major difference between the Siemens reactor and the fluidized-bed reactor is that the latter is a hot-wall reactor, i.e. the wall is not actively cooled. To prevent Si deposition on the hot wall, H_2 is forced to flow along the wall of the reactor. The laminar flow of H_2 along the wall provides a barrier layer between the

hot wall and $SiHCl_3$, reducing the chances for $SiHCl_3$ to react and deposit on the wall. Nevertheless, there is some unavoidable Si deposition on the wall. Another major challenge in the fluidized-bed process is to prevent gas-phase formation of Si powder, which requires precise process control. The desired form of Si is solid Si pieces. Si powder is hard to process in the subsequent step, either the directional solidification process or the Czochralski process. The conversion efficiency of $SiHCl_3$ to solid Si is lower in the fluidized-bed process than in the Siemens process. The energy input for the fluidized-bed process is estimated at about 75 kWh/kg of polycrystalline Si produced.

4.5 A First Look at Major Issues in Solar Photovoltaics

Based on the discussions in this chapter and Chap. 3, we can identify a number of critical research directions in order to reduce the cost and improve the performance of solar photovoltaics. Some of these research directions will lead to incremental improvements over the current state-of-the-art solar cell technologies, and others require significant modifications to the current technologies with potentially revolutionary advances. For example, we can further optimize the current manufacturing processes to increase production throughput and yield, along with cell and module efficiency and lifetime, all of which contribute to a lower module cost. The following are some of the research directions which have been discussed throughout this chapter and in Chap. 3. It is reminded that any new technology developed to improve the efficiency of solar cells has to be cost effective as discussed in Sect. 2.2.

1. Solution-based fabrication of chalcogenide solar cells: The goal is to reduce the manufacturing costs of inorganic solar cells, while maintaining their high efficiencies. Solution fabrication may be difficult for Si solar cells, but has potentials for ionically-bonded semiconductors such as chalcogenides. Active layer, transparent conducting oxide, and metal electrodes may all be deposited from solution.
2. Minimizing optical losses: This includes cost-effective techniques for texturing multicrystalline Si. Alternative antireflection materials such as TiO_2 can be explored as it is better index-matched between glass and Si, and it can be deposited from solution in air. A transparent conducting oxide with higher transmittance and lower sheet resistance is in demand for thin-film solar cells.
3. Minimizing recombination losses: This suggests semiconductors with lower defect densities, which can be realized with improved growth conditions, purer materials, and larger grains in multicrystalline semiconductors. Passivation of existing defects is a different approach, such as cost-effective surface and grain boundary passivation. Process-induced contamination and/or defects in cell and module manufacturing need to be minimized.
4. Minimizing resistive losses: Finger and busbar resistances can be reduced by a higher aspect ratio and/or a denser metal layer. This will likely require a new

metallization technique such as electroplating. Reducing the Schottky barrier height is a more effective approach to reduce metal/semiconductor contact resistance, which requires removal of surface states. Innovative cell structures can bypass some of the tradeoffs in cell design.

5. Reducing material consumption, energy input, and CO_2 emission: The electric-arc furnace process generates about 7 kg of CO_2 for each kilogram of Si produced, and a lower carbon process is desirable. An energy-efficient technique to purify metallurgical-grade Si for 6 N's solar-grade Si shall have a major impact on the solar cell industry. A fast wafering technique with less material losses is needed to replace the sawing process.

There is also a critically important area in solar cell and module manufacturing which can lead to significant cost reductions in installed wafer-Si solar systems, i.e. minimization of the efficiency dispersion or *efficiency uniformization* in cell and module manufacturing. In the current manufacturing processes, the efficiency dispersion in cells and modules is really large. For example, the efficiency of multicrystalline-Si cells from the same ingot and nominally the same process flow can vary between 10 and 18 %. This creates serious problems for module manufacturing and system installation. All the cells and all the modules have to be individually tested and sorted. Only cells within a small efficiency window can be assembled into a module and only modules within a small efficiency window can be connected together into a system, either in series or in parallel, to minimize mismatch losses. Designs of solar systems have to accommodate modules with a wide range of efficiencies, and thus a wide range of output powers. Solar systems of the same output power end up with different numbers of modules, and thus system installers have to custom-make installation hardware for each solar system. When a module in a system fails, we cannot randomly pick up a replacement module. It actually takes some efforts to find a replacement module with a similar efficiency and similar dimensions to the bad module, or the efficiency of the system may be dragged down significantly.

If the cell efficiency dispersion can be narrowed down to, say ± 1 % or ± 0.5 % absolute, testing and sorting in cell and module manufacturing will be largely eliminated. Module fabrication will be so much simpler as we can randomly pick up a cell which will match any other cells in the module. System installation will also be so much simpler in terms of system design and installation hardware as a randomly-picked module will match any other modules in the system. Efficiency uniformization in cell and module manufacturing could be the beginning for industry-wide standardization for wafer-Si solar modules, when all the modules will come out with the same dimensions and power rating with matched current and voltage. Standardization of manufacturing processes and equipment might one day become a reality when the modules are standardized. All of these shall lead to significantly-reduced costs for installed wafer-Si solar systems.

The key to efficiency uniformization lies with the critical steps in wafer-Si cell and module manufacturing to achieve better wafer-to-wafer uniformity. The most critical step for efficiency dispersion in today's manufacturing processes is emitter diffusion, and the second most critical step is front metallization. The surface

doping concentration and emitter depth are determined by diffusion conditions such as temperature and dopant concentration. The recombination losses in the emitter are proportional to the emitter depth. The emitter sheet resistance is a function of both surface doping concentration and emitter depth. The contact resistance of the front electrode depends sensitively on the surface doping concentration. All these parameters play critical roles in cell efficiency. A more consistent surface doping concentration and a more consistent emitter depth between wafers can be achieved in the conveyor furnace over the tube furnace, as each wafer experiences the same temperature ramps and the same dopant concentration in the conveyor furnace. Better control of the width and height of the fingers and busbars is also critical for reproducible finger and busbar resistances between wafers. In addition, thickness consistency of the antireflection layer between wafers needs to be improved for consistent antireflection performance.

In-line metrology is indispensable in our efforts to reduce the cell efficiency dispersion. It is largely missing in today's cell and module manufacturing processes but is required to detect and control process variations. One challenge for in-line metrology is that it has to be able to handle over 1,000 wafers/hour, to be in line with the throughput of solar cell manufacturing. Non-contact approaches such as optical and electromagnetic techniques are good candidates for the required throughput and cost effectiveness.

References

1. Markvart T (2000) Solar electricity, 2nd edn. Wiley, Chichester
2. U.S. Geological Survey (2013) Mineral Commodity Summaries. Available at http://minerals.usgs.gov/minerals/pubs/mcs/2013/mcs2013.pdf
3. Braga AFB, Moreira SP, Zampieri PR, Bacchin JMG, Mei PR (2008) New processes for the production of solar-grade polycrystalline silicon: a review. Sol Energy Mater Sol Cells 92:418–424

Chapter 5
Roadblocks to Terawatt Solar Photovoltaics

As shown in Table 2.3, solar photovoltaics has to be deployed at a scale of tens of peak terawatts or it will make little impact on our future energy mix. Terawatt-scale deployment of any of the cell technologies in Fig. 2.1 requires massive amounts of natural resources such as electricity and raw materials. The limited supplies of these resources will likely prevent many of them from reaching terawatt scales. This chapter begins with a discussion on requirements for a terawatt-scale low-cost high-efficiency solar cell technology. Shortcomings of each current commercial cell technology are outlined. The chapter then presents a quantitative analysis of the maximum possible wattage from each of the current commercial cell technologies based on the known reserve of the limiting material. It is concluded that without significant technological breakthroughs, the current commercial cell technologies combined would meet only an insignificant portion of our future energy demands. In the last section, other roadblocks to terawatt solar photovoltaics are discussed including storage of solar electricity and recycling of end-of-life solar modules.

5.1 Requirements for Terawatt Solar Photovoltaics

Terawatt-scale deployment of solar photovoltaics puts forward many stringent requirements on the cell technology which are unprecedented in other semiconductor technologies such as central processing units, memories, digital signal processors, light-emitting diodes, etc. These requirements can be grouped into two categories: material requirements and device requirements, as listed in Tables 5.1 and 5.2 [1]. Generally speaking, material requirements deal with the scalability and cost of the cell technology and device requirements deal with the efficiency of the cell technology. Out of the four current commercial cell technologies, wafer Si, CdTe, thin-film Si, and CIGS, those which meet each material or device requirement are listed in the last column of Tables 5.1 and 5.2.

M. Tao, *Terawatt Solar Photovoltaics*, SpringerBriefs in Applied Sciences and Technology, DOI: 10.1007/978-1-4471-5643-7_5, © The Author(s) 2014

Table 5.1 Required and desired material properties for a terawatt-scale solar cell technology [1]

	Material property	Candidate technologies
1	Earth-abundant raw materials	None
2	Low-cost raw materials	CdTe
3	Low-cost processing	CdTe
4	Energy-efficient processing	CdTe, thin-film Si, CIGS
5	Low carbon processing	CdTe, thin-film Si, CIGS
6	Low health and environmental impact	Wafer Si, thin-film Si, CIGS
7	Ambient and ultraviolet stability	All
8	Recyclability of dead solar modules	CdTe, CIGS

Current commercial cell technologies which possess each property are listed. Wafer-Si and thin-film Si cells employ scarce materials in their structures

Table 5.2 Required and desired device properties for a terawatt-scale solar cell technology [1]

	Device property	Candidate technologies
9	Broad-spectrum absorption	All
10	High absorption coefficient	CdTe, thin-film Si, CIGS
11	High minority carrier lifetime	Wafer Si, CdTe, CIGS
12	A suitable band gap	Wafer Si, CdTe, CIGS
13	Both conduction types	All
14	Suitable resistivity	All

Current commercial cell technologies which possess each property are listed

5.1.1 Material Requirements

Table 5.1 lists some of the required and desired material properties for a terawatt-scale solar cell technology. Some of these material requirements are common in other semiconductor technologies, but others are unique to solar photovoltaics. To manufacture tens of peak terawatts of solar modules, there must be enough raw materials on this planet. Traveling to the Moon or other planets to mine raw materials is unlikely in the foreseeable future. Many scientists and engineers in the semiconductor industry have not encountered resource limitations, as those technologies require little raw materials as compared to the reserves. The issue of resource limitations became apparent only recently in the solar cell industry as some cell technologies are hitting their resource limitations and others will hit in the near future.

Other material requirements unique to solar photovoltaics include energy-efficient processing and low carbon processing, which are in some cases related. In the U.S. about 68 % of the electricity is generated from fossil fuels. The amount of CO_2 emitted in electricity generation depends on the fuel, from 0.51 kg/kWh (0.51 kg of CO_2 emitted for each kilowatt hour of electricity generated) for natural gas to 1.02 kg/kWh for coal [2]. In other cases a few processes in wafer-Si cell and module manufacturing are quite carbon intensive. A good example is the reduction

of quartz to metallurgical-grade Si in the electric-arc furnace. It emits about 7 kg of CO_2 for each kilogram of Si produced. The semiconductor industry and the solar cell industry share the same manufacturing processes for the production of ultrapure polycrystalline Si, including the energy-intensive Siemens process and the carbon-intensive quartz reduction process. As the amount of Si consumed by the semiconductor industry is small at roughly 40,000 metric tons/year, the energy-intensive and carbon-intensive processes do not make a major impact on natural resources or the environment. The solar cell industry requires dramatically more Si (about 7,000,000 metric tons of Si for 1 TW_p of wafer-Si modules), and this is where the issues of resource limitations and environmental impacts emerge.

Two requirements, i.e. low health and environmental impact as well as ambient and ultraviolet stability, are linked to the field conditions solar modules are under. If a solar module contains a toxic element such as cadmium (Cd), rain or sand storm may rinse or scratch it off the module, contaminating the soil underneath or water nearby. Few solar modules have been out on the field for more than 10 years, so there are limited data on how likely this happens and what long-term effects the toxic element has. Improved module designs can significantly reduce this risk. Solar modules are exposed to all kinds of weather conditions on a 24/7 basis: temperature cycles, ultraviolet radiation, moisture, dust, rain, wind, and sand storm. These conditions either degrade the performance or shorten the lifetime of the module. Selecting proper materials for solar cells and modules and improving module designs are critical in extending the lifetime of solar modules. Although it often sounds less exciting, extending the module lifetime in a cost-effective manner is a strategic research area for solar photovoltaics.

A related issue in terawatt-scale deployment of solar photovoltaics, which has received less attention, is the *recycling of solar modules*. The problem will become obvious in about 15 years when today's installed solar modules, about 100 GW_p total, have gone through their life cycles and start to scatter along highways or pile up in junk yards. CdTe modules are recycled today, due to concerns for the toxic Cd. It is expected that recycling techniques for CIGS modules, similar to those for CdTe modules, can be developed. While wafer-Si modules have about 90 % of the market, there is currently no established technique to recycle them. We can treat dead wafer-Si cells as impure metallurgical-grade Si and adopt the process flow in Fig. 4.1 or 4.6 to recycle them, but a cost-effective and energy-efficient process is desirable. It is also important to remember that there is Ag fused into Si in the cells, which needs to be separated from Si for recycling.

A low-cost cell technology requires low-cost raw materials and low-cost processing. If we have to dig deep under the Earth crust for raw materials or if the raw materials exist in very low concentrations in the minerals, the cost of mining raw materials becomes high. Gallium (Ga) is a good example. It is relatively abundant in the upper Earth continental crust, just slightly scarcer than copper and nickel (Ni) but more abundant than cobalt (Co) and tin (Sn) [3]. However, Ga occurs in very small concentrations in ores of other metals such as bauxite at a typical concentration of about 50 ppm [4]. Producing 100 metric tons of Ga would require the processing of about 2,000,000 metric tons of bauxite if the Ga were

100 % recovered. At 50 % recovery, 100 metric tons of Ga would require the processing of 4,000,000 metric tons of bauxite. Ga production could well be curtailed if there were no need for all the Al produced or Ga consumers would have to pay for all the bauxite and its processing.

In principle, solution-based processes have lower costs than vacuum-based processes. Several solution processes have already found applications in solar cell manufacturing, but it is unlikely to have solar cells fabricated entirely by solution-based processes. This is particularly true for Si solar cells, wafer or thin-film. A root cause for the costly and energy-intensive wafer-Si solar cells, from a materials science prospective, is the directionality and strength of the covalent bond in Si. It makes Si hard to cut through and requires high temperatures to process Si. As the bond angle is rigidly fixed in Si, any atomic misplacement leads to a strained bond or a dangling bond, both of which are electrical defects in the crystal. In low-cost Si synthesized from solution, the density of these defects is so high that the material is often useless in solar cells. On the contrary, the ionic bond in chalcogenides is non-directional, i.e. the bond angle is not rigidly fixed due to the Coulombic nature of the bond. CdTe, CIGS, CZTSS, metal oxides, and metal sulfides all belong to this category. The flexibility of the ionic bond allows small atomic misplacement to be accommodated in the crystal without introducing an electrical defect. For this reason, chalcogenides can be, and in many cases have been, synthesized into multicrystalline films by solution processes with excellent electrical properties, allowing efficient solar cells on these solution-synthesized materials.

5.1.2 Device Requirements

Table 5.2 lists some of the required and desired device properties for a terawatt-scale solar cell technology. As the material requirements in Table 5.1 deal with the scalability and cost of the cell technology, the device requirements in Table 5.2 focus on the efficiency of the cell technology. Some of the requirements have been discussed in Chap. 3. High absorption coefficient requires a direct bandgap semiconductor and enables thin-film photovoltaics. For single-junction solar cells, the suitable bandgap is between 1.1 and 1.5 eV to match the solar spectrum for maximum efficiency. High minority carrier lifetime is to provide photo-generated charge carriers enough time to reach the electrodes. Broad-spectrum absorption refers to the selective absorption of organic semiconductors (Fig. 3.4b), as inorganic semiconductors often display an absorption edge and absorb everything below.

Other requirements in Table 5.2 are implied in Chap. 3. If the terawatt-scale solar cell technology follows the precedents of today's commercial cell technologies and employs a p-n junction for charge separation, it has to have an n-type semiconductor and a p-type semiconductor. The two semiconductors are ideally lattice-matched to minimize recombination losses at the interface. For a maximum efficiency, the resistivity of the semiconductors needs to be optimized. In the

semiconductor industry, conduction type and resistivity are controlled through doping, i.e. introducing a controlled amount of a different element. For Si, n-type doping requires phosphorus or arsenic and p-type doping is typically boron. In chalcogenide semiconductors, native point defects such as vacancies and interstitials play a major role and doping is less effective in determining the conduction type and resistivity of the semiconductor.

5.1.3 Shortcomings of Current Cell Technologies

The fundamental difficulty in solar photovoltaics is that, after 60 years of efforts since the first wafer-Si solar cell [5], we have not discovered a single semiconductor which meets all of the requirements in Tables 5.1 and 5.2. The lack of a perfect semiconductor for solar photovoltaics has led to the co-existence of several cell technologies today, as we have to decide which requirements in Tables 5.1 and 5.2 are less important and can be given up. The shortcomings of each of the current commercial cell technologies, wafer Si, CdTe, thin-film Si, and CIGS, are summarized here. A quantitative analysis will be presented later in this chapter on resource limitations to terawatt solar photovoltaics.

Although Si is one of the most abundant elements on this planet, today's wafer-Si solar cells employ Ag as the front electrode (Fig. 3.1a). Ag is pricy with a limited reserve, and a substitute for Ag has to be found for wafer-Si solar cells to reach a terawatt scale. Another limitation is the high energy input to fabricate wafer-Si cells and modules, which is roughly 4 kWh/W_p, meaning 4 kWh of electricity to produce 1 W_p of wafer-Si modules. The manufacturing processes for wafer-Si cells and modules are costly, as the strong and directional covalent bond in Si makes it hard to cut through and requires high temperatures to process it. The low absorption coefficient of Si due to its indirect bandgap necessitates a thick wafer, currently about 180–200 μm, and light-trapping techniques, such as total internal reflection and back reflector, for complete light absorption.

Thin-film Si solar cells were developed with the intent to reduce the cost and energy input of wafer-Si cells. The fabrication of thin-film Si solar cells bypasses many of the costly and energy-intensive steps for wafer-Si cells, such as $SiHCl_3$ reduction, ingot growth, and ingot wafering. The Si film is synthesized by plasma-enhanced chemical vapor deposition from silane (SiH_4), and SiH_4 is non-corrosive. The amorphous nature of the Si film produces a direct bandgap of 1.75 eV, enabling thin-film Si photovoltaics. At the same time, the amorphous Si leads to a significantly lower efficiency, 13.4 % record versus 25.0 % record for monocrystalline-Si cells (Fig. 2.1). As plasma-enhanced chemical vapor deposition is a vacuum-based batch process, the cost of thin-film Si solar cells is only marginally lower than wafer-Si cells. In addition, today's thin-film Si solar cells often employ Ag as the back reflector and ITO as the front transparent electrode. Both silver and indium (In) have limited reserves on this planet and have to be replaced with Earth-abundant elements for terawatt-scale deployment of thin-film Si solar cells.

CdTe meets most of the requirements in Tables 5.1 and 5.2, except Earth-abundant raw materials and low health and environmental impact. Tellurium (Te) is scarce on this planet, and the annual production of Te is limited. The latter controls the production rate of CdTe modules, i.e. how fast CdTe modules can be deployed. The shrinking market share by CdTe since 2009 (Fig. 2.7) is at least partially attributed to the limited supply of Te. Cd is a toxic heavy metal, although there are arguments that CdTe is a rather stable compound with less toxicity than metallic Cd.

In CIGS, In is scarce and the annual production of In is limited. There are also competitions for In and Ga from other semiconductor technologies such as light-emitting diodes, lasers, and high-voltage power devices, which are almost certain to drive up the prices of In and Ga. The manufacturability of CIGS is another concern, which reduces the yield of CIGS modules resulting in a high module cost. CIGS contains three cations, Cu, In, and Ga, and it is difficult to achieve compositional uniformity for the three cations over large substrates. For this reason CIGS has a higher laboratory efficiency (Fig. 2.1) but much slower commercialization than CdTe. A perfect semiconductor for terawatt solar photovoltaics is ideally a simple compound with fewer components, such as a binary or ternary semiconductor.

5.2 Availability of Raw Materials

All of the current commercial solar cell technologies, wafer Si, CdTe, thin-film Si, and CIGS, suffer from natural resource limitations that prevent them from reaching terawatt scales [6]. These limitations include material scarcity for wafer-Si, CdTe, thin-film Si, CIGS cells [7–9] and high energy input for wafer-Si cells [10, 11]. A quantitative analysis is presented here on these resource limitations to estimate the maximum possible wattage from each of these cell technologies. In particular, the combined impact of these cell technologies on our future energy mix is quantified.

The analysis presented here is performed under best scenarios. If each peak watt of a cell technology requires 1 g of a particular material and there are only 10 g of this material on the planet, the maximum possible wattage from that cell technology is 10 W_p. This is equivalent of assuming:

1. The entire reserve of the raw material can be extracted;
2. All the raw material is exclusively consumed by the solar cell industry;
3. There is no material loss during cell and module manufacturing; and
4. The solar module has an infinite lifetime.

None of these assumptions can be true, so realistically the analysis here represents the upper limit on current cell technologies and their practical contributions to our future energy mix are expected to be significantly lower than our analysis.

The most recent data on raw material reserves and annual productions of raw materials from the U.S. Geological Survey [4], as well as the most recent data on electricity capacity, generation, and consumption from the U.S. Energy

Information Administration [12], is used in the analysis. It is recognized that the reserve data are estimates and new reserves may be discovered in the future. However, the contributions to our future energy mix from all these cell technologies, except wafer Si, are so small that even a 10-time increase in material reserve would not qualitatively change the conclusions of our analysis.

5.2.1 CdTe

CdTe solar cells have seen significant improvements in efficiency recently, up from about 17 % two years ago to 19.6 % today. The best efficiency of commercial CdTe modules today is around 12.8 %. Being a thin-film technology, the CdTe layer is usually 2–8 μm thick [13]. The known reserve of Cd is about 500,000 metric tons as compared to a reserve of about 24,000 metric tons for Te [4], so Te availability will likely limit future production of CdTe modules.

The CdTe crystal has a zinc blende structure with a lattice constant of 0.648 nm. Each unit cell of CdTe contains four Te atoms with a mass of 128 *a*tomic *m*ass *u*nits (amu). The maximum possible volume of CdTe is calculated from the reserve of Te:

$$\text{Volume of CdTe} = \frac{2.4 \times 10^{10}\,\text{g} \times (6.48 \times 10^{-10}\,\text{m})^3}{4 \times 128 \times 1.66 \times 10^{-24}\,\text{g}} = 7.68 \times 10^3\,\text{m}^3$$

Under the best scenario that the CdTe layer is 2 μm thick, the total surface area of CdTe cells is calculated to be 3.84×10^9 m^2. With the solar intensity at AM 1.5 (1,000 W/m^2) and the efficiency of commercial CdTe modules (12.8 %), the total wattage of CdTe modules is found to be 492 GW$_p$. This is equivalent to a time-averaged power output of 49–98 GW, or about 0.16 % of the predicted energy demand in 2100 (Fig. 1.1). Practically, the maximum possible wattage from CdTe is likely to be a fraction of our best-scenario estimate, i.e. less than 0.1 % of the 2100 energy demand.

To illustrate the best-scenario nature of our analysis, our estimate is compared with two earlier estimates published in 2000 and 2008, which found the total wattage of Te-limited CdTe modules to be 300 GW$_p$ [8] and 120 GW$_p$ [9], respectively. They are significantly less than our best-scenario estimate. The 2011 Minerals Yearbook by the U.S. Geological Survey [14] reports a Te consumption rate of about 100 metric tons for 1 GW$_p$ of CdTe modules, resulting in a total wattage of 240 GW$_p$ from CdTe.

5.2.2 CIGS

The best efficiency of commercial CIGS modules is 14.3 %. The CIGS layer is typically 1–2.5 μm thick [13]. The typical composition for CIGS is $CuIn_{0.7}Ga_{0.3}Se_2$. The known reserve of each element in CIGS is Cu

680,000,000 metric tons, In 11,000 metric tons (U.S. Geological Survey 2008), Ga abundant but hard to mine, and Se 98,000 metric tons [4]. The availability of In will likely be the roadblock to future production of CIGS modules.

The CIGS crystal structure is chalcopyrite with lattice constants a = 0.574 nm and c = 1.15 nm. Each unit cell of CIGS contains 2.8 In atoms on average with a mass of 115 amu. The maximum possible volume of CIGS is derived from the reserve of In. The CIGS layer is assumed to be 1 μm thick under the best scenario, and thus the total surface area of CIGS cells is obtained. Assuming AM 1.5 solar intensity, the total wattage from CIGS modules is found to be 1.1 TW_p, or a time-averaged output of 110–220 GW. This is about 0.34 % of the predicted energy demand in 2100. Practically, the maximum possible wattage from CIGS is likely to be less than 0.2 % of the 2100 energy demand.

For comparison, two earlier estimates of material constraint for CIGS modules based on In reserve concluded the maximum possible wattage of 90 GW_p [8] and 120 GW_p [9], respectively. In both cases, our best-scenario analysis presents a better, but still insignificant, outlook. Currently it takes about 25 metric tons of In to produce 1 GW_p of CIGS modules. At this consumption rate, 11,000 metric tons of In reserve would be enough for a total wattage of 440 GW_p from CIGS.

Furthermore, In is used in other semiconductor technologies other than CIGS modules, such as flat-panel displays, light-emitting diodes, lasers, and high-voltage power devices. Those devices consume much less In but can be sold for much higher prices than CIGS solar modules on a per unit area basis, meaning that they can afford higher-price In than the solar cell industry. Besides availability, the cost of In may become prohibitively high in the future.

5.2.3 Wafer Si

Wafer-Si solar cells, including multicrystalline and monocrystalline, dominate the solar cell industry with a market share close to 90 % (Fig. 2.7). Monocrystalline-Si cells, which are manufactured using the Czochralski process, have the highest efficiency of all commercial single-junction solar cells (Fig. 2.1). Multicrystalline-Si cells, which are manufactured using directional solidification, have a lower efficiency (2–5 % absolute) but a significantly lower cost.

Despite the abundance of Si, wafer-Si solar cells suffer from several resource limitations for terawatt-scale deployment. One of these limitations is Ag which is used in wafer-Si cells as the front finger electrode (Fig. 3.1a). The known reserve of Ag is about 540,000 metric tons [4]. The density of Ag is 10.5 g/cm^3. The typical efficiency of mass-produced monocrystalline-Si modules with Ag front electrode is about 16.8 %. Assuming that the Ag electrode is 12 μm thick, the maximum possible area of the Ag electrode is:

$$\text{Area of Ag electrode} = \frac{5.4 \times 10^{11}\,\text{g}}{10.5\,\text{g/cm}^3 \times 1.2 \times 10^{-3}\,\text{cm}} = 4.29 \times 10^9\,\text{m}^2$$

If the Ag electrode covers 7 % of the surface area of monocrystalline-Si cells, the total surface area of the cells is found to be 6.12×10^{10} m^2. At AM 1.5 and with 16.8 % efficiency, the maximum possible wattage of monocrystalline-Si modules as limited by Ag availability would be 10.3 TW_p. This is equivalent of an averaged power output of 1–2 TW or about 3.3 % of the predicted energy demand in 2100. The current Ag consumption rate in wafer-Si solar cells is about 0.1 g/W_p, leading to a maximum possible wattage of 5.4 TW_p from wafer Si for the 540,000 metric tons of reserve. On the other hand, our estimate is smaller than an early analysis [9], as that analysis assumed a 2-μm thick Ag electrode.

The number for wafer-Si solar cells based on Ag reserve is more optimistic than the numbers for CdTe and CIGS. However, this is a best-scenario estimate and does not take into account of the other industries which compete for Ag [14]. Those industrial applications for Ag include solders, brazing alloys, batteries, catalysts, jewelry, silverware, among others. The competition for Ag is likely to drive up the Ag price, and the actual output of wafer-Si modules is likely to fall far short of the above analysis, maybe just 2 % of the 2100 energy demand.

The future scale of wafer-Si modules depends on several factors. One factor is the Ag reserve as discussed above. If more Ag, say 5 times more, is discovered or a substitute for Ag is developed, it will eliminate one of the roadblocks for wafer-Si modules to reach a terawatt scale. The scarcity of Ag also suggests the importance of recycling Ag from wafer-Si modules. Currently there is no established technique to recycle Ag fused into Si. Another roadblock for wafer-Si solar cells is the high energy input, which will be discussed in Sect. 5.4. The reserves of Te and In have to increase by 100 times for those cell technologies to be able to make noticeable contributions to our future energy mix, which is unlikely.

5.2.4 Thin-Film Si

Thin-film Si solar cells have a significantly lower energy input than wafer-Si cells, but they suffer from resource limitations as they often employ Ag as the back reflector and ITO as the transparent electrode [13]. The reserves of Ag and In are 540,000 and 11,000 metric tons, respectively [4]. The availability of In will likely be the roadblock to future production of thin-film Si modules.

The crystal structure of ITO is body-centered cubic. The unit cell contains 80 atoms, including 48 oxygen atoms and 32 In and Sn atoms, with a lattice constant of 1.01 nm. The maximum Sn/In ratio in ITO is about 10 %. The maximum possible volume of ITO based on the In reserve is:

$$\text{Volume of ITO} = \frac{1.1 \times 10^{10}\,\text{g} \times (1.01 \times 10^{-9}\,\text{m})^3}{32 \times 0.9 \times 115 \times 1.66 \times 10^{-24}\,\text{g}} = 2.06 \times 10^3\,\text{m}^3$$

If the ITO layer is 0.5 μm thick in thin-film Si cells, the maximum possible area of ITO is found to be 4.12×10^9 m^2. The best efficiency of commercial thin-film

Table 5.3 Estimated, best-scenario maximum wattages for current commercial solar cell technologies based on the reserve of the limiting material in each technology [6]

Technology	Efficiency (%)	Limiting material	Reserve [4] (metric ton)	Maximum wattage	Averaged output	% of 2100 energy demand
Wafer-Si	16.8	Ag	540,000	10.3 TW_p	1.03–2.06 TW	3.3
CdTe	12.8	Te	24,000	492 GW_p	49–98 GW	0.16
CIGS	14.3	In	11,000	1.1 TW_p	110–220 GW	0.34

Thin-film Si is not listed as it competes for In with CIGS and Ag with wafer Si

Si modules is about 9.8 %. Under AM 1.5, the maximum possible wattage from thin-film Si is limited to 404 GW_p, or 40–81 GW time-averaged output. This is about 0.13 % of the predicted 2100 energy demand.

If an Earth-abundant substitute for In or ITO is developed, Ag would become the next limiting factor for thin-film Si cells. Assuming the Ag back reflector is 2 μm thick, the reserve of Ag allows a maximum possible area of 2.57×10^{10} m^2 for the Ag reflector. The maximum possible wattage from thin-film Si, as limited by Ag reserve, is then 2.5 TW_p or 250–500 GW time-averaged output. This is about 0.78 % of the predicted 2100 energy demand.

Thin-film Si solar cells compete with wafer-Si cells for Ag, and with CIGS cells for In. For the same amount of Ag, wafer-Si cells generate 4 times more power over thin-film Si (10.3 TW_p versus 2.5 TW_p). For the same amount of In, CIGS cells generate 2.7 times more power over thin-film Si (1.1 TW_p versus 404 GW_p). It would be better to use these limited resources in a more effective manner, i.e. in wafer-Si and CIGS cells.

However, the long-term outlook for thin-film Si modules is less clear. CdTe and CIGS are unlikely to reach terawatt scales due to limited reserves of raw materials. The future of wafer-Si solar cells depends on two factors: substitution of Ag electrode with an Earth-abundant metal and reduction of the energy input in Si wafer manufacturing as discussed in Sect. 5.4. If either of these efforts fails, *and* if substitutes for ITO and Ag are developed, thin-film Si modules may become the only cell technology capable of terawatt-scale deployment, even if the cost remains high and the efficiency remains low.

5.2.5 Summary on Material Availability

It is interesting to add up all the numbers from the analysis above and examine the combined impact of all the current commercial solar cell technologies on our future energy mix. Table 5.3 summarizes our best-scenario estimates of the maximum wattages for the current commercial cell technologies based on the known reserve of the limiting material in each technology. Thin-film Si is not listed, since Ag and In are better used in wafer-Si and CIGS cells for more electricity. With all the technologies combined, they would provide no more than 4 % of

the energy demand in 2100 under best scenarios. Realistically these technologies combined would provide probably just 2 % of the 2100 energy demand, an insignificant number.

5.3 Annual Production of Raw Materials

The production rates of the raw materials limit the deployment rates of various cell technologies [6]. Under steady state, the annual deployment of solar modules for 60 TW_p total installation and 25-year average module lifetime is 2.4 TW_p/year. During the initial build-up period, it is preferred to deploy more than 2.4 TW_p/year for a quick build-up of the solar photovoltaic capacity. As the analysis below suggests, the maximum possible deployment rate of all the current commercial solar cell technologies combined would be about 500 GW_p/year under best scenarios.

The annual production of Te is 500–550 metric tons in 2011 [14]. This gives a maximum possible production rate of about 10.8 GW_p/year for CdTe modules. Compared to the current production rate of CdTe modules at about 2 GW_p/year, the room for future growth is not unlimited for CdTe. Taking into consideration the current production rate of all types of solar cells combined at about 30 GW_p/year and the expected rapid growth of the solar cell industry as a whole, the market share by CdTe will likely continue its decline in the future. At the current mining rate of 500–550 metric tons/year, it would take 46 years to reach the maximum wattage for CdTe and deplete the Te reserve.

The annual production of Ga is about 292 metric tons/year in 2011, compared to that of In at 662 metric tons/year [14]. The deployment rate of CIGS modules may be limited by either of these two materials. If Ga is the limiting material and all the Ga production is used only for CIGS cells, the production rate of CIGS modules would be limited to 114 GW_p/year. If In is the limiting material and all the In production is used only for CIGS cells, the production rate would be limited to 67.1 GW_p/year. Therefore, In is more likely to limit the deployment rate of CIGS modules. At 67.1 GW_p/year, it would take 17 years for CIGS modules to reach the maximum wattage and deplete the In reserve.

The annual production of Ag is 24,000 metric tons/year [4], which allows at best 458 GW_p of wafer-Si modules a year. Practically, wafer-Si modules will likely be limited to maybe 200–300 GW_p/year. In 2012, the annual production of solar modules reached 30 GW_p/year, with 89 % of them wafer-Si modules. The solar cell industry currently consumes about 10 % of the global Ag production. If the solar cell industry maintains an average annual growth rate of 50 % as it has seen since 2005, it will take only 6 years before the production of wafer-Si modules reaches 300 GW_p/year and consumes most of the global Ag production. The price of Ag will likely skyrocket due to short supply. On the other hand, the current production rate of Ag would deplete its reserve in 23 years.

Table 5.4 summarizes the best-scenario production rates of all the current commercial solar cell technologies based on the current production rate of the limiting

Table 5.4 Estimated, best-scenario maximum annual productions of current commercial solar cell technologies based on the annual production of the limiting material in each technology [6]

Technology	Efficiency (%)	Limiting material	Annual production (metric ton)	Annual peak wattage (GW_p)	Years to depletion
Wafer-Si	16.8	Ag	24,000	458	23
CdTe	12.8	Te	525	11	46
CIGS	14.3	In	662	67	17

Thin-film Si is not listed as it competes for In with CIGS and Ag with wafer Si

material in each technology. Thin-film Si is not listed, as Ag and In are better used in wafer-Si and CIGS cells. With the current production rates of the raw materials, CdTe and CIGS modules are to be limited to no more than a few tens of peak gigawatts a year. The largest number is wafer-Si modules at over 450 GW_p/year best scenario. The combined production rate is 536 GW_p/year best scenario and maybe 300 GW_p/year practical. This is far short of the 2.4 TW_p/year required for 60 TW_p steady-state installation.

5.4 Energy Input for Wafer-Si Cells and Modules

The energy input to manufacture wafer-Si cells and modules is huge. Figure 4.1 shows a common industrial process flow to manufacture monocrystalline-Si cells and modules [1]. The major steps include quartz reduction to metallurgical-grade Si, distillation of $SiHCl_3$ for purification, reduction of $SiHCl_3$ to ultrapure polycrystalline Si, Czochralski growth for monocrystalline-Si ingot, ingot slicing for Si wafers, cell fabrication, and module fabrication. The electricity inputs for the most energy-intensive steps are labeled in the figure.

Let us first estimate the energy input for polycrystalline Si. The energy input for the electric-arc furnace process is about 15 kWh/kg of Si produced. There is additional electricity for quartz mining and transportation, and for coke and graphite electrode production. The total energy input for metallurgical-grade Si is thus estimated at 20 kWh/kg of Si produced. The energy input for the Siemens process for $SiHCl_3$ reduction is indicated in Fig. 4.1 [15]. Let us assume that the energy inputs for the remaining steps, conversion of metallurgical-grade Si to $SiHCl_3$ and distillation of $SiHCl_3$, are each at 10 kWh/kg of Si content processed. Let us also assume that each step loses on average 20 % of the Si material. The energy input for impure $SiHCl_3$ is:

$$\text{Energy Input for Impure } SiHCl_3 = \frac{20\,\text{kWh/kg}}{0.8} + 10\,\text{kWh/kg} = 35\,\text{kWh/kg}$$

Similarly, the energy inputs for purified $SiHCl_3$ and for polycrystalline Si are:

$$\text{Energy Input for Purified } SiHCl_3 = \frac{35\,\text{kWh/kg}}{0.8} + 10\,\text{kWh/kg} = 53.8\,\text{kWh/kg}$$

$$\text{Energy Input for Poly-Si} = \frac{53.8\,\text{kWh/kg}}{0.8} + 150\,\text{kWh/kg} = 217\,\text{kWh/kg}$$

i.e. the energy input for polycrystalline Si is over 200 kWh/kg.

Now let us estimate the energy input for monocrystalline-Si wafers. The energy input for Czochralski growth is indicated in Fig. 4.1 [15]. With 20 % material loss in Czochralski growth, the energy input for monocrystalline-Si ingots is:

$$\text{Energy Input for Mono-Si Ingot} = \frac{217\,\text{kWh/kg}}{0.8} + 100\,\text{kWh/kg} = 371\,\text{kWh/kg}$$

The wafering step for monocrystalline-Si ingots has about 65 % material loss. If ingot slicing takes 10 kWh of electricity for each kilogram of Si produced, the total amount of electricity required to produce one kilogram of monocrystalline-Si wafers is:

$$\text{Energy Input for Mono-Si Wafer} = \frac{371\,\text{kWh/kg}}{0.35} + 10\,\text{kWh/kg} = 1,071\,\text{kWh/kg}$$

i.e. the energy input for monocrystalline-Si wafers is over 1,000 kWh/kg. This makes monocrystalline-Si wafers the most energy-intensive product on the Earth.

Finally let us estimate the energy input for monocrystalline-Si modules. Let us assume that the electricity required to fabricate solar cells from monocrystalline-Si wafers is 30 kWh/kg of Si. The fabrication involves multiple steps as shown in Fig. 4.4, including diffusion at about 900 °C and metal electrode firing at about 750 °C. The electricity required to fabricate modules from cells is estimated at 230 kWh/kg of Si processed. The energy input for Al is about 15 kWh/kg, and it takes about 12 kg of Al to frame 1 kg of Si wafers. This is equal to 180 kWh/kg of Si just for the Al frame. It takes about 12 kg of glass to frame 1 kg of Si wafers, and the energy input for the front glass sheet is estimated at 40 kWh/kg of Si. If the yields from wafers to cells and from cells to modules are both 90 %, the energy inputs for monocrystalline-Si cells and modules are:

$$\text{Energy Input for Mono-Si Cell} = \frac{1,071\,\text{kWh/kg}}{0.9} + 30\,\text{kWh/kg} = 1,220\,\text{kWh/kg}$$

$$\text{Energy Input for Mono-Si Module} = \frac{1,220\,\text{kWh/kg}}{0.9} + 230\,\text{kWh/kg} = 1,586\,\text{kWh/kg}$$

Each kilogram of monocrystalline-Si wafers has a surface area of 2.26 m^2, if they are 190 μm thick. Under AM 1.5 and with 16.8 % efficiency, each kilogram of monocrystalline-Si wafers generates 380 W_p in output power. This gives the energy input for monocrystalline-Si modules in kWh/W_p:

$$\text{Energy Input for Mono-Si Module} = \frac{1,586\,\text{kWh/kg}}{380\,\text{W}_\text{p}/\text{kg}} = 4.17\,\text{kWh/W}_\text{p}$$

Although the final energy input for monocrystalline-Si modules, about 4.2 kWh/W_p, is high, it is only a fraction of two earlier estimates at about 16 kWh/W_p [10, 11]. Each peak watt of solar modules will produce the following amount of electricity on an annual basis:

$$\text{Electricity Generation} = 0.15\,\text{W/W}_\text{p} \times 24\,\text{h/d} \times 365\,\text{d/y} = 1.31\,\text{kWh/W}_\text{p}\text{-year}$$

where 0.15 W/W_p is the time-averaged output of solar modules. The calculation above indicates that the energy payback time, i.e. the time for solar modules to generate the same amount of electricity we put in to manufacture them, is over 3 years for monocrystalline-Si modules.

If monocrystalline-Si modules were produced at 2.4 TW_p/year for 60 TW_p steady-state installation, they would require over 6,000,000 metric tons of monocrystalline-Si wafers and consume about 1×10^{13} kWh of electricity each year. If we take into consideration the transmission losses between power plants and solar cell factories, which are typically about 30 %, the amount of electricity required to manufacture 2.4 TW_p/year of monocrystalline-Si modules would be 1.3×10^{13} kWh/year. This is about 65 % of the 2010 global electricity generation [12]. It would be difficult for the energy-thirsty planet to squeeze out 65 % of its electricity consumption for solar cells, which will likely become a roadblock for wafer-Si modules to reach a terawatt scale. The exact scale of wafer-Si modules would depend on non-technical issues such as public consensus and determination, if Ag is successfully replaced with an Earth-abundant metal.

One argument in favor of wafer-Si solar cells is that installed solar modules will generate electricity to offset the high energy input for manufacturing additional modules. If the production of wafer-Si modules were stable at 2.4 TW_p/year, in 4 years the 9.6 TW_p installed modules would generate enough electricity to cover the production of 2.4 TW_p monocrystalline-Si modules in each subsequent year till the end of the life cycles of the modules, and then the industry would produce net electricity. This argument works when the industry is in a steady-state mode. It does not work when the industry expands rapidly. To build up the initial capacity of 60 TW_p, we would have to invest a significant portion of our electricity into wafer-Si modules, which could well slow the deployment rate of wafer-Si modules.

A related bottleneck for wafer-Si solar modules is the cost associated with the high energy input. In the U.S., industrial electricity costs about $0.07/kWh [16]. With the energy input at 4.2 kWh/W_p for monocrystalline-Si modules, the electricity cost is about $0.29/$W_p$. It is difficult for the module cost to drop below $0.50/$W_p$ if the electricity cost alone is $0.29/$W_p$. To contain cost, many polycrystalline-Si and Si wafer producers place their factories near hydropower plants for cheap electricity. This strategy works only when the solar cell industry is small, since the availability of hydropower is limited [17]. When the production of wafer-Si modules reach 2.4 TW_p/year at 4 kWh/W_p, it would demand more electricity than all the hydropower on this planet. In other words, the energy input for wafer-Si modules has to be reduced significantly or their cost will likely go up when the increasing demand for electricity strains the supply.

Table 5.5 Estimated energy input for wafer-Si solar modules by different processes, which is between 2.5 and 4.2 kWh/W_p

	Siemens process (kWh/W_p)	Fluidized-bed process (kWh/W_p)
Mono-Si modules	~4.2	~3.3
Multi-Si modules	~3.4	~2.5

At these levels, terawatt-scale production of wafer-Si modules would require a prohibitively huge amount of electricity

Multicrystalline-Si modules have the largest market share at about 60 %. Directional solidification, instead of Czochralski growth, is used to produce multicrystalline-Si ingots with an energy tag of about 15 kWh/kg (Fig. 4.6). A similar calculation is made for the total energy input of multicrystalline-Si modules, with the material loss during wafering of multicrystalline-Si ingots at 60 %. The best efficiency of multicrystalline-Si modules today is about 16 %, resulting in an energy input of 3.38 kWh/W_p for multicrystalline-Si modules. There is also a possibility to replace the energy-intensive Siemens process with the fluidized-bed process for polycrystalline Si. Directional solidification combined with fluidized-bed process results in the most energy-efficient process flow for wafer-Si modules to date (Fig. 4.6), with an energy input of 2.54 kWh/W_p for multicrystalline-Si modules. The energy payback time for this process flow is about 2 years. The estimated energy inputs for wafer-Si modules by different processes are listed in Table 5.5. The driving force for multicrystalline-Si modules is partially their lower energy input and the associated lower cost.

5.5 Other Roadblocks to Terawatt Solar Photovoltaics

Besides resource limitations such as raw materials and electricity, there are other roadblocks to terawatt-scale deployment of solar photovoltaics. Here we discuss two of those roadblocks. One is storage of solar electricity and the other is recycling of solar modules.

5.5.1 Storage of Solar Electricity

Solar electricity is a less predictable energy source and its production cycle often mismatches with the demands. Storage of solar electricity is often required to deliver the energy for later demands or to different locations. The current electric grid can provide some buffer for the instantaneous solar electricity, but it is widely believed that the electric grid is incapable of taking more than 10 % of its input from instantaneous sources. 10 % of the 2010 global electricity capacity is 500 GW [12], providing about 3 % of the current global energy demand. A 500-GW

electricity capacity requires 2.5–5 TW_p of solar modules, i.e. the deployment of solar photovoltaics would be capped at 2.5–5 TW_p if they were integrated into the current electric grid without storage.

Storage for solar electricity is required for solar photovoltaics to become an important source of energy in our life. However, it is important to recognize that the storage for solar electricity can, but does not have to, be connected to the electric grid. Grid-connected storage takes in electricity and outputs electricity, which narrows the options for storage to "electricity-in and electricity-out". Off-grid storage takes in electricity but can output electricity or fuel or heat. This provides more leeway for creative ideas in solar electricity storage as the options now become "electricity-in and anything-out".

The amount of solar electricity for storage can be estimated. If our target is for solar photovoltaics to provide 30 % of the current global energy demand, it means 5.4 TW out of the 18-TW total demand. This is equivalent to roughly 1.3×10^{11} kWh of electricity over a 24-hour period. This electricity is produced in the daytime. Some of it is consumed as soon as it is generated, but most of it has to be stored for demands at night. From the hourly solar intensity, it is estimated that solar modules generate electricity for about 11 hours over a 24-hour period, i.e. about 55 % of the 1.3×10^{11} kWh of electricity has to be stored on a daily basis:

$$\text{Electricity Storage} = 0.55 \times 1.3 \times 10^{11}\,\text{kWh/day} = 7.13 \times 10^{10}\,\text{kWh/day}$$

The typical capacity of laptop computer batteries is 50 Wh. Storage of 7.13×10^{10} kWh/day of electricity requires about 1.43×10^{12} batteries of laptop type, or about 204 batteries per person for the 7 billion people on this planet. At this scale, we have to consider resource limitations to battery technologies and pick up a technology which is not only low cost but also employs Earth-abundant materials. The known reserves of lithium and vanadium, which are the key materials in two battery technologies, are about 13,000,000 metric tons each on this planet [4].

There are several factors which will likely drive up the required storage capacity far beyond the estimate above. The global energy demands are projected to reach 30 TW by 2050 and 46 TW by 2100 [18]. If solar-to-chemical conversion technologies do not work out or turn out to be more costly than solar photovoltaics, the contribution from solar photovoltaics to our future energy mix would have to be significantly higher than 30 %. There are also cloudy and rainy days, so the batteries may not be charged on a daily basis.

There have been several analyses on grid-connected storage options for solar electricity [19]. The options considered include batteries, flywheels, supercapacitors, compressed air, pumped hydropower, superconducting magnetic storage, and thermal storage. Since the power output from the storage will likely be above 5 TW, the capacity of each individual storage system on the electric grid has to be on the order of gigawatt. This would eliminate many of the options above. The capacities of flywheels, supercapacitors, and superconducting magnetic storage are typically about 1 MW each. It would take millions of these devices to store and

output 5 TW. The capacity of batteries is about 30 MW today. Gigawatt-scale battery storage systems are possible with further development of the technology, and we have to examine the resource requirements of the technology: raw materials, electricity, water, chemicals, wastes, recycling, etc. Pumped hydropower and compressed air are currently the only two technologies with gigawatt capacity [19], but they are limited by geological conditions. For example, the Phoenix area in Arizona, with the highest solar intensity in the U.S. and over 4 million people, has no reservoir for pumped hydropower or underground cavern for compressed air.

5.5.2 Recycling of Solar Modules

Recycling of solar modules, in particular Si modules, has received less attention. The problem will become obvious in about 15 years when today's installed solar modules have gone through their life cycles and start to scatter along highways or pile up in junk yards. CdTe modules are recycled today, due to concerns for the toxic Cd. While wafer-Si modules have about 90 % of the market, there is currently no established process to recycle them. It is also important to remember that the Ag fused into Si needs to be extracted out of the dead modules.

With 60 TW_p steady-state installation and 25 years of average module lifetime, there would be 2.4 TW_p dead modules each year. If these were wafer-Si modules with 16.8 % efficiency, their total area would be 1.43×10^4 km^2 or 5.52×10^3 $miles^2$. This is about the size of Connecticut, i.e. each year and globally we would have to recycle dead modules of the size of Connecticut. If not recycled, they would quickly litter the planet.

Recycling of wafer-Si modules is not straightforward. The front glass sheet can be stripped off the module. It can be cleaned and then either reused in a new module or fed into the glass production line as a feedstock. The polymeric back sheet and EVA can be burned off by heating them in air to about 400 °C, which generates a small amount of CO_2. If the back sheet is metallic, it can be cleaned and then either reused in a new module or melted to form a new back sheet. Now the wafer-Si cells remain, with Cu wires soldered to them. The solders typically contain Sn and Pb. As shown in Fig. 3.1a, the cells are Si wafers of 180–200 μm thick, with Ag and Al of tens of micrometers on the front side and backside. There is a thin SiN_x layer of about 75 nm, which has little value to recycle. There are also small amounts of boron, phosphorus, and aluminum as dopants in Si, which need to be removed from recycled Si.

We can treat the dead wafer-Si cells as impure metallurgical-grade Si and go through the rest of the process flow in Fig. 4.1 or 4.6 to produce ultrapure polycrystalline Si and manufacture new wafer-Si modules from it. There are few cost or energy benefits in such a process flow as compared to the process flow with quartz as the starting material, as dead wafer-Si cells would have to go through all the energy-intensive steps in Fig. 4.1 or 4.6. In addition, modifications have to be made in these process flows to extract Ag, Sn, Pb, and Cu out of dead cells,

which incur additional costs. Ag, Sn, Pb, and Cu are likely to remain in the leftover sludge from the formation of $SiHCl_3$, as chlorides of these metals (AgCl, $SnCl_2$, $CuCl_2$, and $PbCl_2$) have far higher boiling points, ranging from 623 °C for $SnCl_2$ to 1,547 °C for AgCl, than $SiHCl_3$ and the chlorides of other impurities, boron, phosphorus, nitrogen, and aluminum. It is not entirely clear that how Ag, Sn, Pb, and Cu can be separated and recovered from the sludge, as it contains many elements.

A more reasonable process we can think of is to recycle about 90 % of the Ag as well as about 80 % of the Si in dead wafer-Si cells. The Cu wires, Sn and Pb solders, and Ag fingers and busbars can be dissolved chemically or electrolytically from dead wafer-Si cells. This would recover most of the Ag, Sn, Pb, and Cu into a solution (about 90 %), but usually not the Ag fused into Si. It is feasible to electrolytically reduce and separate the dissolved metals into solid Ag, Sn, Pb, and Cu from the solution for recycling, which is achieved by applying different reduction potentials to the solution. The dead wafer-Si cells through this process are largely intact. We can further dissolve the Al and SiN_x from the dead cells chemically. The remaining Si wafers have fused-in silver and heavy phosphorus doping on the front side, as well as heavy aluminum doping on the backside. The heavy Al layer on the backside is 10–20 μm thick. There are well-established chemistries to etch off about 20-μm material from each side of the wafer in a solution. This removes the heavy aluminum layer on the backside and the heavy phosphorus layer on the front side. The resultant Si wafer is about 150 μm thick with low 10^{16} cm^{-3} boron doping. The purity and doping of the remaining wafer is suitable as a feedstock for Czochralski growth or directional solidification. However, there is currently no effective technique to extract ultrapure solid Si from the dissolved Si in the solution, which is roughly 20 % of the Si in dead cells. A more effective process is desirable to recover more Si from dead wafer-Si cells.

References

1. Tao M (2008) Inorganic photovoltaic solar cells: silicon and beyond. Electrochem Soc Interface 17(4):30–35
2. U.S. Environmental Protection Agency, Clean energy. Available at http://www.epa.gov/cleanenergy/energy-and-you/index.html
3. U.S. Geological Survey (2002) Rare earth elements—critical resources for high technology. Available at http://pubs.usgs.gov/fs/2002/fs087-02/
4. U.S. Geological Survey (2013) Mineral commodity summaries. Available at http://minerals.usgs.gov/minerals/pubs/mcs/2013/mcs2013.pdf
5. Chapin DM, Fuller CS, Pearson GL (1954) A new silicon p-n junction photocell for converting solar radiation into electrical power. J Appl Phys 25:676–677
6. Tao CS, Jiang J, Tao M (2011) Natural resource limitations to terawatt-scale solar cells. Sol Energy Mater Sol Cells 95:3176–3180
7. Andersson BA, Azar C, Holmberg J, Karlsson S (1998) Material constraints for thin-film solar cells. Energy 23:407–411
8. Andersson BA (2000) Materials availability for large-scale thin-film photovoltaics. Prog Photovoltaics Res Appl 8:61–76

9. Feltrin A, Freundlich A (2008) Material considerations for terawatt level deployment of photovoltaics. Renew Energy 33:180–185
10. Shah AV, Platz R, Keppner H (1995) Thin-film silicon solar cells: a review and selected trends. Solar Energy Mater Solar Cells 38:501–520
11. Kato K, Murata A, Sakuta K (1998) Energy pay-back time and life-cycle CO_2 emission of residential PV power system with silicon PV module. Prog Photovoltaics Res Appl 6:105–115
12. U.S. Energy Information Administration (2012) International energy statistics 2012. Available at http://www.eia.gov/cfapps/ipdbproject/iedindex3.cfm
13. Fortunato E, Ginley D, Hosono H, Paine DC (2007) Transparent conducting oxides for photovoltaics. MRS Bull 32:242–247
14. U.S. Geological Survey (2013) 2011 Minerals yearbook. Available at http://minerals.usgs.gov/minerals/pubs/commodity/myb/
15. Markvart T (2000) Solar electricity, 2nd edn. Wiley, Chichester
16. U.S. Energy Information Administration (2013) Electric power annual. Available at http://www.eia.gov/electricity/annual/
17. Lewis NS (2007) Powering the planet. MRS Bull 32:808–820
18. Hoffert MI, Caldeira K, Jain AK, Haites EF, Harvey LDD, Potter SD et al (1998) Energy implications of future stabilization of atmospheric CO_2 content. Nature 395:881–884
19. International Renewable Energy Agency (2012) Electricity storage-technology brief. Available at http://www.irena.org/DocumentDownloads/Publications/IRENA-ETSAP%20Tech%20Brief%20E18%20Electricity-Storage.pdf

Chapter 6
Pathways to Terawatt Solar Photovoltaics

There are multiple roadblocks and bottlenecks for the current commercial solar cell technologies to become a noticeable source of energy in our future energy mix. Roadblocks represent showstoppers which we have to remove in order to move forward. Bottlenecks are difficulties which we would like to overcome, but we can live with if push comes to shove. For terawatt-scale deployment of solar photovoltaics, resource limitations are roadblocks, and cost and efficiency are bottlenecks.

We took our first look at some of the major issues in solar photovoltaics in Sect. 4.5. In this chapter we will take a more serious look at roadblocks and bottlenecks for terawatt-scale deployment of solar photovoltaics. Several strategic research directions for terawatt solar photovoltaics are identified as enlightened by the discussions in previous chapters, in particular Chap. 5 on resource limitations. A number of technical approaches to tackle these roadblocks and bottlenecks are proposed based on the best judgment of the author. The discussions here are divided into terawatt wafer-Si solar photovoltaics, terawatt thin-film solar photovoltaics (including thin-film Si), and terawatt storage for solar electricity.

6.1 Terawatt Wafer-Si Solar Photovoltaics

Three roadblocks for wafer-Si solar cells were discussed in Chap. 5. They are the front Ag electrode, the high energy input, and storage for solar electricity. If no more Ag is discovered on this planet, the maximum wattage from wafer-Si modules will likely be limited to about 10 TW_p under best scenarios (Table 5.3). The energy input for monocrystalline-Si modules is about 4.2 kWh/W_p and for multicrystalline-Si modules it is about 2.5 kWh/W_p (Table 5.5). At a production rate of a few peak terawatts per year, wafer-Si modules would demand a prohibitive portion of the global electricity generation. Storage of solar electricity is a cross-cutting issue for all terawatt-scale cell technologies. Without storage, the scale of grid-connected solar photovoltaics will likely be capped at 2.5–5 TW_p.

M. Tao, *Terawatt Solar Photovoltaics*, SpringerBriefs in Applied Sciences and Technology, DOI: 10.1007/978-1-4471-5643-7_6, © The Author(s) 2014

Several bottlenecks for wafer-Si solar modules were discussed in Chaps. 4 and 5. The most critical bottleneck is probably ingot wafering. With most of the Si material turned into saw dust during wafering, it significantly drives up the cost and energy input for wafer-Si modules. Efficiency dispersion in cell and module manufacturing is another critical bottleneck, which was discussed in Sect. 4.5. Improving module lifetime is particularly important for wafer-Si modules, as wafer-Si cells often last far beyond the lifetime of the module. Recycling of wafer-Si cells is also a critical bottleneck for which there is currently no established process. These bottlenecks are on top of our daily efforts to reduce production cost and improve cell and module efficiencies. Some of the roadblocks and bottlenecks for terawatt wafer-Si solar photovoltaics are discussed in more details below.

6.1.1 Substitution for Front Ag Electrode

Most of today's wafer-Si solar cells employ Ag as the front finger electrode over the n-type emitter, while Al is used as the back electrode on the p-type base (Fig. 3.1a). The limited Ag reserve at about 540,000 metric tons [1] will likely limit the role of wafer-Si modules in our future energy mix (Table 5.3), unless a substitute for Ag is developed. In addition, the price of Ag has been fluctuating since summer 2010 from as low as $18/ounce to as high as $45/ounce. This makes cost control difficult for solar cell manufacturers, as Ag metallization is the most costly step between wafers and cells. If the solar cell industry continues to grow at the current pace, which is on average about 50 % annually since 2005, and if the consumption rate for Ag in wafer-Si cells remains constant on the basis of grams per peak watt (currently about 0.1 g/W_p), the demand for Ag will soon overwhelm the supply, ensuring a skyrocketing Ag price. The solar cell industry is working on techniques to reduce the consumption rate of Ag in wafer-Si solar cells. This alleviates, but does not eliminate, the roadblock.

In order to replace Ag in wafer-Si solar cells, we have to first identify suitable substitutes for Ag. There are several considerations in identifying suitable substitutes such as material abundance and resistivity. As the front finger electrode, the resistivity of the substitute metal has to be low and comparable to that of Ag. If a metal with a higher resistivity is used, the aspect ratio of the finger electrode has to increase in order to maintain the same finger resistance. This presents a challenge for the current metallization process, i.e. screen printing. We can increase the density of the metal finger so its resistivity approaches its bulk value. This will likely require a new metallization technique.

As a reference, Ag has the lowest resistivity of all metals at 1.59×10^{-6} Ω-cm. Table 6.1 compares the resistivity of ten least-resistive metals, from low to high. Based on resistivity, Cu is the best candidate for Ag, with its resistivity only 6 % higher than Ag. If gold (Au) is used for the front finger electrode and the finger width is kept the same, the finger height or aspect ratio has to increase by 53 % to keep the same finger resistance. This is challenging, but potentially still doable.

Table 6.1 Resistivity of ten least-resistive metals as compared to Ag (unit: 10^{-6} Ω-cm)

Metal	Ag	Cu	Au	Al	Ca	W	Zn	Ni	Li	Fe
Resistivity	1.59	1.68	2.44	2.82	3.36	5.60	5.90	6.99	9.28	10.0
% Increase	0	5.7	53	77	111	252	271	340	452	529

Cu has a similar resistivity to Ag, and Al has a roughly 77 % higher resistivity than Ag. Anything beyond Ca is probably too resistive as the front finger electrode

Table 6.2 Reserve and annual production of the ten metals in Table 6.1 [1] (unit: 10^6 metric tons)

Metal	Ag	Cu	Au	Al	Ca	W	Zn	Ni	Li	Fe
Reserve	0.54	680	0.052	28,000	Large	3.2	250	75	13	80,000
Annual production	0.024	17	0.003	44.9	–	0.073	13	2.1	0.037	1,100

Both Cu and Al have huge reserves and annual productions. Au is excluded from consideration as it does not meet the material abundance requirement

For Al, the aspect ratio has to increase by 77 % and for calcium (Ca), it is 111 %. The difficulty in processing these metals increases from Cu to Au to Al to Ca. Anything beyond Ca is probably too resistive as the finger electrode.

For terawatt solar photovoltaics, material abundance has to be taken into consideration. This eliminates Au as a candidate. As shown in Table 6.2, the known reserve of Au is only 52,000 metric tons and the annual production of Au is less than 3,000 metric tons/year [1]. The other three metals, Cu, Al, and Ca meet the material abundance requirement. Another consideration is the stability of the metal in air. Ca readily reacts with air and easily oxidizes. This raises concerns about the reliability and lifetime of modules with Ca electrodes. Although we can design a perfectly airtight module for Ca electrodes, the cost of such modules is likely high. For this reason, Ca is eliminated and suitable substitutes for Ag are limited to Cu and Al. Both have huge reserves with annual productions above 10,000,000 metric tons/year, sufficient for terawatt-scale production and deployment of wafer-Si solar modules.

The biggest advantage of Cu over Al is its low resistivity, resulting in little change in the required aspect ratio for the finger electrode as compared to Ag. Major efforts have been underway for years in the solar cell industry to develop a metallization process for Cu electrodes. Instead of screen printing, Cu is electroplated, a solution process to ensure low-cost processing. Electroplated Cu is dense with its resistivity very close to its bulk value and far below that of screen-printed Ag. Efficiencies above 20 % have been demonstrated on commercial-size wafer-Si cells with a Cu front electrode [2]. On the other hand, the higher resistivity of Al requires a higher aspect ratio for the finger electrode, challenging the current screen printing process. Development of an Al metallization process has barely started.

At this time it is difficult to draw a conclusion on which metal, Cu or Al, is a better substitute for Ag in wafer-Si solar cells. Nevertheless an analysis can be made on their respective pros and cons. Despite its low resistivity and manufacturing-ready process, Cu has several weaknesses as an electrode in wafer-Si cells.

Cu as an impurity in Si introduces defect states deep into the middle of the bandgap which significantly reduce the lifetime of photo-generated charge carriers and thus the cell efficiency. A barrier layer is required between Cu and Si to prevent Cu from contacting and diffusing into Si. The most common barrier material is nickel monosilicide (NiSi) [2]. It is formed by depositing a layer of Ni on a Si wafer and then annealing the wafer at about 400 °C to form NiSi. It is unclear how fast Cu diffuses through NiSi under field conditions, as this may become a limiting factor to module reliability and lifetime.

Oxidation of Cu is another concern for module reliability and lifetime. Ag is resistant to oxidation at room temperature and elevated temperatures. This ensures a metallic, low-resistance front electrode after firing, which is carried out in air at about 750 °C. It also ensures long-term reliability of the module as the Ag electrode will not oxidize under field conditions. Cu readily oxidizes into highly-resistive semiconducting copper oxides. This is particularly true in tropical weathers as Cu oxidation is faster in a humid climate than in a dry climate. The common practice today is to deposit a protective layer over Cu in order to slow down its oxidation. The protective layer is typically Sn [2], which is also electroplated. The long-term effectiveness of the protective Sn layer over Cu oxidation has yet to be determined. It may be necessary to design a more airtight module for Cu electrodes. In addition, firing for Cu electrodes may have to be performed in an oxygen-free environment. On the other hand, the availability of Sn may become an issue as Sn has many applications beyond solar cells such as food cans, plumbing fixtures, solders, and fluorine-doped tin oxide as a transparent conducting oxide. The reserve of Sn on this planet is 4,900,000 metric tons and its annual production 230,000 metric tons/year [1]. In 2011, the consumption of Sn is estimated to be slightly above its supply [3].

The three-layer structure for the Cu electrode, i.e. Sn/Cu/NiSi, complicates the Cu metallization process and thus increases the cost. Al, on the other hand, allows a double-layer electrode, i.e. Sn/Al. Al can be in direct contact with Si without introducing defect states near the middle of the bandgap, eliminating the need for a barrier layer and the related concerns for module reliability. The oxidation of Al forms a dense insulating aluminum oxide (Al_2O_3) layer, which prevents further oxidation of the underlying Al. This eliminates the need for a protective layer over Al, while improving module reliability and lifetime. It also allows Al electrodes to be fired in air without vacuum or an inert ambient.

Al is a p-type dopant in Si, and diffusion of Al into the n-type emitter has to be avoided to prevent dopant compensation in the emitter. It is reminded that Al was the contact metal of choice in the semiconductor industry 50 years ago, on both n-type and p-type Si. The key is the firing temperature. At the current firing temperature, 750 °C, Al will certainly diffuse into Si in high concentration resulting in heavy p-type doping. However, if the firing temperature stays below 400 °C, Al diffusion into Si becomes negligible. Today's Al paste is designed for 750 °C firing, not suitable for 400 °C firing. This requires a new metallization process for the front Al electrode, in which the maximum process temperature is below 400 °C. If the Al back electrode on the p-type base is still fired at 750 °C, a

Table 6.3 Comparison of Cu and Al as the front finger electrode in wafer-Si solar cells

	Cu	Al
Resistivity	1.59×10^{-6} Ω-cm	2.82×10^{-6} Ω-cm
Oxidation resistance	Poor	Good
Effect in Si	Minority carrier killer	p-type dopant
Solderability	Good	Poor

The lower resistivity of Cu reduces resistive losses, while the better oxidation resistance of Al improves module reliability and lifetime

two-step firing process will have to be developed, i.e. the first firing at 750 °C for the back Al electrode on the p-type base and then the second firing below 400 °C for the front Al electrode on the n-type emitter. Such a two-step firing process is likely more costly than the current one-step firing process, but this is probably the price we have to pay for replacing Ag with Al in wafer-Si solar cells.

The higher resistivity of Al over Ag requires either a higher aspect ratio or a denser Al layer for the front electrode, which is a challenge for the screen printing process. As today's Al paste is unsuitable for the front electrode due to its high firing temperature, it is unclear at this time which metallization process will be employed for the front Al electrode, screen printing or physical vapor deposition [4] or electroplating? Another major issue with Al is its solderability. Both Ag and Sn are solderable, but not Al. In order to solder to Al, we have to break the Al_2O_3 layer which covers the Al electrodes. An alternative is to electroplate a thin layer of Sn over Al electrodes, just thick enough for soldering. This would add complexity, thus cost, to the Al metallization process. Table 6.3 summarizes the comparison between Cu and Al as the front finger electrode in wafer-Si solar cells.

6.1.2 Energy-Efficient Production of Si Wafers

The energy input for each step in wafer-Si cell and module manufacturing was estimated in Sect. 5.4. The energy input for polycrystalline-Si feedstock is between 140 and 220 kWh/kg, depending on whether the Siemens or the fluidized-bed process is employed for $SiHCl_3$ reduction. The energy input for Si wafers is as high as 1,070 kWh/kg for monocrystalline wafers, or as low as 490 kWh/kg for multicrystalline wafers. It is suggested in Sect. 5.4 that the high energy inputs for wafer-Si cells and modules will likely become a roadblock for terawatt-scale wafer-Si solar photovoltaics, as they will demand a prohibitive portion of the global electricity generation for terawatt-scale production of wafer-Si modules.

The energy-intensive steps in monocrystalline-Si cell and module manufacturing (Fig. 4.1), in order of their energy intensity, are:

1. The Siemens process at about 150 kWh/kg of Si produced;
2. The Czochralski process at about 100 kWh/kg of Si produced; and
3. The module fabrication process at about 230 kWh/kg of Si processed.

Table 6.4 Typical impurities and their representative concentrations in metallurgical-grade Si and target impurity concentrations for solar-grade Si [5]

Element	MG-Si (ppm)	SG-Si (ppm)	Redox pair	Standard reduction potential (V)
Si	2 N's	>6 N's	Si^{4+}/Si	−1.99
O	3,000	<10	$O_2/2O^{2-}$	0.00
B	40	<1	B^{3+}/B	−1.63
P	20	<5	P^{2+}/P	−1.27
C	600	<10	C^{4+}/C	−1.07
Fe	2,000	<10	Fe^{3+}/Fe	−0.81
Al	100–200	<2	Al^{3+}/Al	−2.23
Ca	500–600	<2	Ca^{2+}/Ca	−2.56
Ti	200	<1	Ti^{2+}/Ti	−1.81

The table also includes assumptive redox pairs for the impurities and their standard reduction potentials [7]

Although the number for the final module fabrication process appears the largest, it is behind Siemens and Czochralski processes in the actual energy intensity. This is because most of the polycrystalline-Si material after Siemens and most of the monocrystalline ingot after Czochralski are turned into saw dust during ingot wafering, which significantly drives up the actual energy inputs for Siemens and Czochralski processes on the basis of each kilogram of Si wafers produced.

The Czochralski process for monocrystalline-Si ingots has been largely replaced by the directional solidification process (Fig. 4.6), which reduces the energy input for ingot growth from about 100 kWh/kg to about 15 kWh/kg. Most of the energy input in the final module fabrication process comes from the Al frame, which not only seals the module but also provides mechanical support for the module. It is less likely that a substitute metal for Al can be found, which has to be light, less energy intensive, stable in all kinds of weather, and low cost. Innovative module designs are needed to reduce the Al consumption in modules.

For wafer-Si solar modules to reach a terawatt scale, the energy input for the Siemens or the fluidized-bed process has to be significantly reduced. These processes are employed to reduce purified $SiHCl_3$ to ultrapure polycrystalline Si, so the question becomes: is there another pathway to ultrapure Si from metallurgical-grade Si besides $SiHCl_3$? A positive answer relies on the development of an alternative purification process.

There are various impurities in metallurgical-grade Si. Table 6.4 lists typical impurities and their representative concentrations in metallurgical-grade Si [5]. The target impurity concentrations for solar-grade Si are also listed. A good purification technique has to be effective on all the impurities in metallurgical-grade Si. This excludes many physical and some chemical purification techniques, such as chemical treatment of the raw materials, impurity segregation between two phases, and chemical or gaseous treatment of Si melt [6], as they are often effective on a selected group of impurities.

A universal purification technique for all impurities has to rely on a universal property of every impurity. Distillation relies on the boiling point, a universal

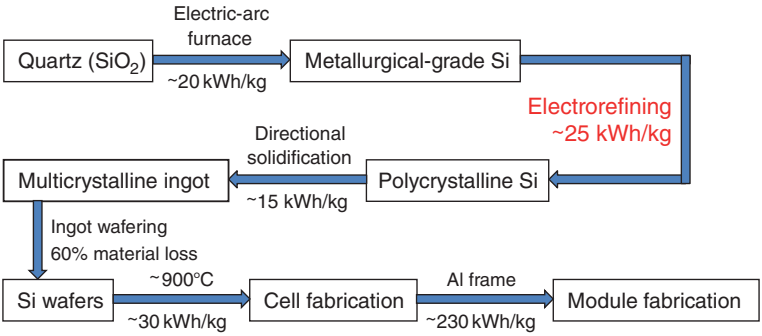

Fig. 6.1 A proposed process flow for multicrystalline-Si modules. The major change in this process flow as compared to the process flow in Fig. 4.6 is electrorefining, which is proposed to produce ultrapure polycrystalline Si directly from metallurgical-grade Si, bypassing $SiHCl_3$ distillation and fluidized-bed processes in Fig. 4.6

property, of all impurities. By controlling the evaporation and condensation temperatures in distillation, all impurities can be removed from $SiHCl_3$ leaving behind ultrapure $SiHCl_3$. A new purification technique to replace distillation will have to rely on a different but universal property of all impurities. One such universal property of all impurities is the standard reduction potential. As shown in Table 6.4, each impurity has a distinctive standard reduction potential [7], which suggests electrolysis as a potentially effective purification technique. With electrolytic purification, several steps in the current industrial process flow for wafer-Si modules would be eliminated and replaced by electrorefining, as shown in Fig. 6.1.

The advantages of electrolytic purification for ultrapure Si have long been recognized. In principle, each electron transfer in electrolysis leads to a chemical reaction, resulting in 100 % internal quantum efficiency for electrolysis. The overall efficiency of electrolysis is lower than 100 % due to resistive losses in the circuit but can still surpass 90 %. In contrast, the current industrial process flow for Si wafers relies heavily on thermal processes. In a thermal process, a large chunk of a material is heated to a high temperature in order to activate a tiny fraction of it for reaction. The activated fraction is proportional to $\exp(-E_a/RT)$, where E_a is the activation energy for the chemical reaction and R the gas constant. Therefore, electrolysis may hold the key to energy-efficient production of Si wafers.

Electrolytic purification of metallurgical-grade Si was first reported by Monnier et al. 50 years ago [8]. They employed a two-electrode electrolytic cell, with an anode and a cathode, for the experiment. Their objective was to produce semiconductor-grade Si directly from metallurgical-grade Si. Both metallurgical-grade Si and a molten alloy of metallurgical-grade Si and Cu were used as the anode. The electrolyte was silica (SiO_2) dissolved in cryolite, a mineral with the molecular formula of Na_3AlF_6. The highest purity they achieved was 4 N's, i.e. 99.99 % (the minimum purity for solar-grade Si is 6 N's or 99.9999 %). Since then

there have been many studies by over a dozen groups worldwide on electrolytic purification of metallurgical-grade Si. However, after 50 years of efforts by over a dozen groups, no one has succeeded in producing ultrapure Si of at least 6 N's by electrolysis [9]. It is reminded that electrolysis has been practiced for over 100 years in production and purification of many metals in our daily life, such as Al and Cu. The required purity of these metals is no more than 4 N's, which has been routinely produced on commercial scales by electrolysis. However, ultrapure materials by electrolysis remain an unanswered challenge for the electrochemical community.

The author recently published a thermodynamic analysis on impurity behavior in electrolysis [10], which reveals a fundamental flaw in all the previous efforts on ultrapure Si by electrolysis. All these studies employed a two-electrode electrolytic cell, with an anode and a cathode. Although most industrial electrolytic processes employ the two-electrode configuration, our analysis suggests that the thermodynamics for the two-electrode configuration prohibits any purification and only the kinetics allows some purification. This is why low purity is possible, but not high purity, by the two-electrode configuration. The root cause here is that two-electrode electrolysis does not allow the precise control of the potential applied to the anode or cathode. It actually controls the potential difference between anode and cathode. An analogy for this in distillation is that we would be allowed to control only the temperature difference between evaporation and condensation, but not the precise temperature for evaporation or condensation. This would not produce ultrapure $SiHCl_3$ as we all know.

Our analysis suggests that it is possible to obtain ultrapure solar-grade Si directly from metallurgical-grade Si in a three-electrode electrolytic cell with a working electrode, a counter electrode, and a reference electrode. The potential applied to the working electrode, including the magnitude and polarity, with respect to the reference electrode is the driving force for electrolytic purification. If the electrolytic process is performed under equilibrium, impurity segregation between working electrode and electrolyte is given by [10]:

$$E_{red} - E^{o}_{red} = \frac{kT}{zq} \ln\ k_o$$

where E_{red} is the reduction potential applied to the working electrode, E^{o}_{red} is the standard reduction potential for the impurity, k the Boltzmann constant, T the absolute temperature, q the electron charge, and z the oxidation state of the impurity. k_o is the impurity segregation coefficient between working electrode and electrolyte and is defined as:

$$k_o = \frac{C_{we}}{C_l}$$

where C_{we} is the impurity concentration in the working electrode and C_l is the impurity concentration in the electrolyte. If the electrolysis is under equilibrium, the equation above provides the exact conditions to achieve solar-grade Si directly from metallurgical-grade Si [10].

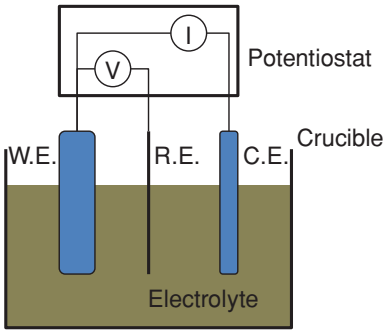

Fig. 6.2 A proposed three-electrode electrolytic process for solar-grade Si [10]. The potential applied to the working electrode (W.E.) is controlled with respect to the reference electrode (R.E.). Depending on the polarity of the applied potential, the working electrode may be the anode or cathode. The anode is metallurgical-grade Si and the cathode is purified Si

Figure 6.2 illustrates schematically a three-electrode electrolytic cell for solar-grade Si directly from metallurgical-grade Si. The actual electrolytic process in this cell is almost certainly to be more complicated than what the thermodynamic theory predicts. Many factors will play a role in the process. For example, there may be formation of various complexes in the electrolyte which are irreversible or cause incorporation of impurities into the purified Si. A significant overpotential is typically required to achieve a reasonable throughput in the process, which drives the process away from the thermodynamic analysis. Oxidation of Si leads to formation of insulating SiO_2 on the surface of the electrodes, which slows down and even stops the process. All these and other complicating factors have to be worked out for this electrolytic process to succeed.

The energy inputs for polycrystalline Si and multicrystalline-Si wafers shall be reduced to about 50 and 204 kWh/kg, respectively, if the energy input for electrolytic purification is 25 kWh/kg. The energy input for multicrystalline-Si modules from electrolytic purification shall be about 1.35 kWh/W_p. This is significantly lower than all the current processes (Table 5.5), resulting in an energy payback time of about 1 year. It is also noted that success in electrolytic purification of metallurgical-grade Si will add an alternative process to recycle wafer-Si cells.

6.1.3 Fast and Kerfless Cutting of Si Ingots

Slicing of Si ingots into wafers with a multiple-wire saw is an extremely slow process. It also turns about 60 % of the Si ingot material into waste. These factors drive up the cost and energy intensity of Si wafers significantly. The solar cell industry has been pushing for thinner wafers, but there is a tradeoff between thickness and mechanical strength of the wafer. As a result, wafer breakage in cell manufacturing goes up with thinner wafers. The current wafer thickness is between

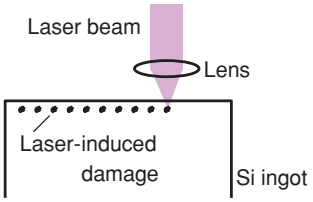

Fig. 6.3 A proposed laser wafering technique for Si ingots [12]. Reproduced with permission of IEEE. Focusing a laser beam below the surface and scanning it across the surface creates a layer of weakened Si. By changing the focal depth of the laser beam, multiple layers of weakened Si are produced. The weakened Si can be chemically etched off, producing multiple wafers simultaneously

180 and 200 μm, which has been stable for several years. Advanced and cost-effective wafer handling tools have to be developed for thinner wafers. Alternatively, a new wafering technique is highly desirable, which has to be fast and produce less waste. Laser-based processing is particularly promising for Si ingot wafering.

Laser wafering promises a narrow kerf of about 10 μm. This is much smaller than the 150-μm kerf by a wire saw and is achieved by focusing the laser beam to a diameter of about 10 μm. Laser wafering also introduces less damage to the Si wafer than the wire saw, resulting in a damaged layer of only a few micrometers instead of tens of micrometers. Overall, laser wafering has the potential to reduce kerf loss to about 20 μm, i.e. a 90 % reduction over the wire saw process. The powerful laser beam heats up the Si in the irradiated spot, leading to melting and evaporation of the Si material.

Laser cutting of Si wafers is a manufacturing process, but laser cutting of Si ingots has yet to be demonstrated. The difference is the thickness of the Si material to be cut. Si wafers are less than 1 mm thick, and the thickness of Si ingots is between 125 and 156 mm. In a deep kerf, the evaporated Si in the middle of the ingot has to travel a long distance between Si before reaching the edge of the ingot. This results in redeposition of evaporated Si inside the kerf, limiting the effectiveness of this technique. One modification to this technique is to couple the laser beam with a liquid jet [11]. The liquid contains a Si etchant, such as NaOH, which helps the removal of the molten or evaporated Si. Delivering the liquid to the bottom of a deep long kerf and getting it out of the kerf are some of the challenges. There is also a large amount of waste chemicals from the liquid which we have to deal with.

It is possible that laser wafering does not rely on material evaporation, but subsurface engraving in the Si ingot [12]. In this case, the energy of the photons in the laser beam is below the bandgap of Si, so they are typically not absorbed in the ingot. The technique relies on the nonlinear absorption coefficient of Si with light intensity. When the laser beam is focused at a spot below the surface of the ingot, the high light intensity causes significant absorption, which heats up the spot and creates a damaged or defective point in the ingot (Fig. 6.3). This spot would be chemically or mechanically weaker than the undamaged ingot. By scanning the

laser beam across the surface, a two-dimensional array of damaged spots is produced resulting in a weakened layer in the ingot. By changing the focal depth of the laser beam, multiple layers of weakened Si are produced in the ingot. The layers of weakened Si could be chemically etched off, producing multiple wafers simultaneously. The kerf loss for this technique is estimated to be about 20 μm, i.e. a 90 % reduction over the wire saw process [12].

Another interesting idea for Si cutting is Joule heating to create a narrow linear molten zone in a Si ingot [13]. This technique relies on an important property of Si, i.e. its resistivity decreases with temperature. When an electrical current flows through a Si ingot, it tends to concentrate along the straight path between the two electrical contacts, which is the path of least resistance. Joule heating increases the temperature along the path, thus reducing its resistivity. This further concentrates the current to the least-resistance path, which creates an even higher temperature along the path. With a sufficiently large current, this positive feedback creates a narrow straight molten zone in the Si ingot between the two contacts. The main advantage of this technique is its zero kerf loss, as molten Si does not evaporate but recrystallizes when the electric power is removed.

This technique may not be the best option for ingot wafering. The width of the molten Si zone by Joule heating is about 500 μm. It is hard to imagine that it can produce Si wafers of 200 μm thick or less when the "kerf" is much more than 200 μm. Potential contamination from the electrical contacts is also a concern, as the materials involved become really active at the melting point of Si, 1,420 °C. This technique, however, may be competitive in cutting the circular Si ingot from Czochralski into a quasi-square ingot, or the rectangular Si ingot from directional solidification into square blocks of 156 × 156 mm^2.

6.2 Terawatt Thin-Film Solar Photovoltaics

If, for whatever reason(s), wafer-Si solar cells do not reach a terawatt scale, thin-film solar cells have to take over the role if solar photovoltaics is going to be an important source of energy in our life. CdTe or CIGS is not capable of terawatt-scale deployment. Thin-film Si has the potential to reach a terawatt scale, if the scarce materials in thin-film Si solar cells are replaced with Earth-abundant materials. Alternatively, a new solar cell technology may emerge which employs Earth-abundant low-cost materials and largely solution-based fabrication processes.

6.2.1 Thin-Film Si Solar Photovoltaics

Figure 6.4 is a schematic of a thin-film Si p-i-n solar cell [14], where "i" stands for "intrinsic" or undoped. The p-i-n structure allows the potential gradient of the p-n junction to extend throughout the entire intrinsic Si absorber. This results in

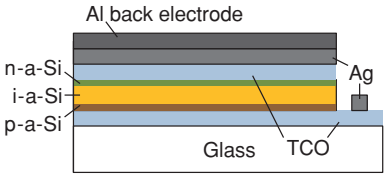

Fig. 6.4 Schematic of a thin-film Si p-i-n solar cell. The transparent conducting oxides have been traditionally ITO which has to be replaced with an Earth-abundant material. The Ag back reflector and front electrode have to be replaced with Al. Sunlight comes from the bottom, i.e. the glass side

immediate separation of photo-generated electron and hole pairs as soon as they appear in the absorber, as discussed in Sect. 3.2.2. The fabrication of this cell starts with a glass sheet coated with a transparent conducting oxide. A p-type Si layer of 20–40 nm, an undoped Si layer of about 1 μm, and an n-type Si layer of 20–40 nm are deposited sequentially in a multiple-chamber plasma-enhanced chemical vapor deposition system. The precursor for Si is SiH_4, and the precursors for p-type and n-type doping are diborane (B_2H_6) and phosphine (PH_3), respectively. Another layer of transparent conducting oxide, an Ag layer as the back reflector, and an Al layer as the back electrode are fabricated sequentially on top of the Si p-i-n structure by sputter deposition. After patterning of the multiple-layer stack to isolate individual cells, Ag electrodes are fabricated to the first transparent conducting oxide layer as the front electrode. Sunlight comes from the bottom, i.e. from the glass side.

There are several roadblocks and bottlenecks for the current thin-film Si cell technology to reach a terawatt scale. The cost for thin-film Si cells is high, due to the largely vacuum-based fabrication processes. The efficiency for thin-film Si cells is low, roughly about half of that for wafer-Si cells. More importantly, the current thin-film Si cells employ several scarce materials which have to be replaced with Earth-abundant materials. The transparent conducting oxides are traditionally ITO and the back reflector and front electrode are Ag. The reserves and annual productions of Ag and In are provided in Tables 5.3 and 5.4. As estimated in Sect. 5.2.4, the maximum possible wattage from thin-film Si as limited by In reserve is 404 GW_p, or about 0.13 % of the predicted 2100 energy demand. If an Earth-abundant substitute for In is developed, the maximum possible wattage from thin-film Si as limited by Ag reserve is 2.5 TW_p or about 0.78 % of the predicted 2100 energy demand.

Several candidates have been identified for an In-free transparent conducting oxide in thin-film solar cells, but their performance (sheet resistance and transmittance) is still inferior to ITO [14]. Zinc oxide (ZnO) is one of the top candidates, which is naturally n-type. Undoped ZnO is highly resistive and doping is required to reduce its resistivity into the low 10^{-4} Ω-cm range. n-type dopants in ZnO include group IIIA elements, Al, Ga, and In, for the Zn sublattice and group VIIA elements, fluorine and chlorine, for the oxygen sublattice. It is important that the dopant is Earth-abundant, which excludes Ga and In. It is also possible to codope ZnO with

a group IIIA element and a group VIIA element simultaneously, in order to further reduce its resistivity [15]. TiO_2 is another possible substitute for ITO, which meets the material abundance requirement. Fluorine-doped tin oxide (FTO) has been employed in commercial thin-film Si solar cells. The availability of Sn may become the roadblock for FTO, as the reserve of Sn is estimated at 4,900,000 metric tons [1].

The requirements for the substitute metal for Ag in thin-film Si solar cells include high reflectance, low resistivity, and material abundance. As shown in Tables 6.1 and 6.2, the only candidates for Ag are Cu and Al, based on resistivity and material abundance. If we take the reflectance into consideration, Al becomes the only suitable candidate for Ag as the back reflector. For the thin-film Si solar cell in Fig. 6.4, we can replace Ag by removing the Ag layer and increasing the thickness of the Al back electrode. Al does not reflect light as well as Ag, so there will likely be some optical losses on the backside. The front Ag electrode in Fig. 6.4 also needs to be replaced with Al.

A note by the author on March 23, 2014: In March 2014, the author visited a thin-film Si solar cell company in Hunan, China and would like to update the reader on the visit. The latest thin-film Si cell technology employs almost exclusively Earth-abundant materials. No In or ITO is to be found in the newest cell structure. The back reflector is no longer Ag. The front and back electrodes are no longer metallic. Ag is used only in the electrical leads of the module. The amount of Ag used in a module is minute and can be replaced by Cu. Thin-film Si is thus the only cell technology capable of terawatt-scale deployment today.

The recycling process for thin-film Si modules is not well established. There are currently no effective techniques to recycle the Al back electrode, transparent conducting oxide layer, or Si p-i-n stack in Fig. 6.4. Each of these layers is a few micrometers thick. This leaves only the Ag and front glass sheet for recycling. The Al back electrode can be etched off chemically. The Ag back reflector and front electrode can be chemically or electrolytically dissolved into a solution, in which the dissolved Ag can be electrolytically reduced to metallic Ag. The transparent conducting oxide layers and the Si p-i-n stack can be chemically etched off, leaving behind the front glass sheet for recycling.

6.2.2 Thin-Film Post-Si Solar Photovoltaics

There are multiple roadblocks and bottlenecks for wafer-Si solar cells, energy input, Ag electrode, ingot wafering, efficiency dispersion, among others. Thin-film Si solar cells also suffer from several roadblocks and bottlenecks, ITO, Ag back reflector, efficiency, cost, among others. If none of these two cell technologies reaches a terawatt scale, a new cell technology will have to be developed which employs Earth-abundant materials and largely solution-based fabrication processes. Even if wafer-Si or thin-film Si can reach a terawatt scale, a new terawatt-capable cell technology is still worth pursuing as it may turn out to be much more cost-effective than the current technologies. It is uncertain at this time whether the

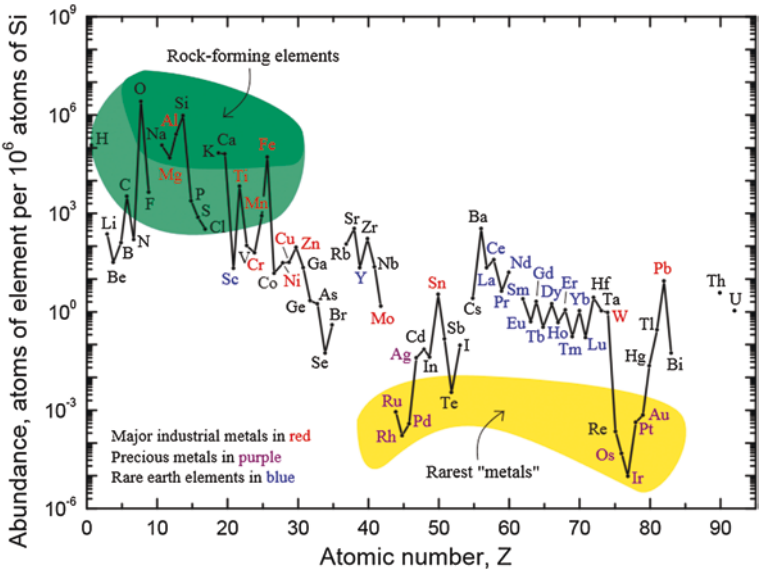

Fig. 6.5 Relative abundance of elements in the Earth upper continental crust as a function of atomic number [16], where mining is relatively easier than deep into the Earth crust or under the ocean. Light elements are typically more abundant than heavy elements with a few exceptions such as Pb and Ba

new cell technology will be based on similar device physics to today's commercial cell technologies, i.e. an inorganic semiconductor for light absorption and a p-n junction for charge separation. The discussion in this section assumes similar device physics for the new cell technology.

There are many required and desired properties for such a new cell technology, some of which are summarized in Tables 5.1 and 5.2. First of all, the raw materials for the semiconductor absorber in the new cell technology have to be Earth-abundant and low cost. Figure 6.5 illustrates the relative abundance of elements in the Earth upper continental crust [16], where mining is relatively cheaper than deep into the Earth crust or under the ocean. If we set the cutoff for material abundance at the level of Pb, a reduced periodic table for Earth-abundant elements is produced as shown in Table 6.5. By setting the cutoff at a different element, a slightly-different periodic table of Earth-abundant elements was produced by Alharbi et al. [17]. In general, light elements are more abundant than heavy elements, with a few exceptions such as Pb. Furthermore, the annual production of the raw materials limits the deployment rate of a cell technology. 60 TW_p steady-state installation and 25 years of module lifetime translate into a production rate of 2.4 TW_p/year for solar modules. Here we set the cutoff for annual material production at 100,000 metric tons/year, which eliminates all the 11 elements in italic type in Table 6.5. The data on annual material production comes from the U.S. Geological Survey [1].

Comparing the remaining elements in Table 6.5 with the requirements in Tables 5.1 and 5.2 eliminates more elements from the table. Group IA elements,

Table 6.5 A reduced periodic table of Earth-abundant elements in the upper continental crust, which are in bold type

IA	IIA	IIIB	IVB	VB	VIB	VIIB	VIII	VIII	VIII	IB	IIB	IIIA	IVA	VA	VIA	VIIA
H																
Li	*Be*											**B**	**C**	**N**	**O**	F
Na	**Mg**											**Al**	**Si**	**P**	**S**	Cl
K	**Ca**	*Sc*	**Ti**	*V*	**Cr**	**Mn**	**Fe**	**Co**	**Ni**	**Cu**	**Zn**	*Ga*				
Rb	**Sr**	*Y*	**Zr**	*Nb*												
	Ba	*											**Pb**			

*La, Ce, and Nd also make the cut for material abundance, but their productions are below 100,000 metric tons/year
The cutoff is set at the level of Pb. Earth-abundant elements are typically light elements with a few exceptions such as Pb and Ba

Table 6.6 Bandgap values of several possible binary semiconductors for a new terawatt-scale solar cell technology [17]

Semiconductor	α-Ca_3N_2	SnS	β-$BaSi_2$	CuP_2	Zn_3P_2	WS_2
Indirect bandgap (eV)		1.09	1.13	1.4	1.38	1.20
Direct bandgap (eV)	1.55	1.3	1.23	1.5	1.5	1.35

Their smaller indirect bandgap limits the open-circuit voltage in the cell and their larger direct bandgap reduces the absorption coefficient below the direct bandgap

sodium and potassium, react vehemently with water, and almost all of their compounds dissolve in water. They are certainly unsuitable as the absorber in solar cells, and thus eliminated in Table 6.5. Hydrogen is not known to form a semiconductor with any other element. The same is true for chlorine and fluorine. Almost none of their compounds with other elements is a semiconductor. They are all eliminated from our consideration. The final periodic table of Earth-abundant elements contains about 20 elements, with about 15 metals, which are suitable for a terawatt-scale solar cell technology. They are in bold type in Fig. 6.5.

Now the question becomes: how do we make semiconductors out of the remaining 20 or so elements in Table 6.5 and whether one of them would meet the remaining requirements in Tables 5.1 and 5.2? There is only one elemental semiconductor in Table 6.5, Si, so we have to look for a compound semiconductor for the new terawatt-scale cell technology. It is obvious that a compound between metals does not produce a semiconductor, so the compounds for us to look into are silicides, pnictides, and chalcogenides. Most carbides have bandgaps way above 1.5 eV.

An important factor in solar cell cost is the manufacturability of the semiconductor absorber, which impacts the yield. Although CIGS has a higher laboratory efficiency than CdTe (Fig. 2.1), the slower commercialization of CIGS than CdTe suggests a simple compound semiconductor with fewer components for the new terawatt-scale cell technology, as discussed in Sect. 5.1.3. For this reason our search for the terawatt-scale semiconductor absorber should first focus on binary silicides, pnictides, and chalcogenides, i.e. a compound between a metal and one of the group IVA, VA, or VIA elements in Table 6.5. If binary compounds do not pan out, our next focus should be ternary silicides, pnictides, and chalcogenides, which open up more possibilities. If possible, we should stay away from quaternary compounds.

Many of the possible binary semiconductors for terawatt solar photovoltaics are summarized in reference [17]. If we limit the choices to direct bandgap semiconductors, there is only one option for binary semiconductors from reference [17], i.e. calcium nitride (α-Ca_3N_2) (Table 6.6). Its bandgap is 1.55 eV direct, close to the upper limit for optimum bandgap (Fig. 3.7). Many Earth-abundant binary semiconductors have indirect bandgaps. If their indirect bandgaps are within the 1.1–1.5 eV optimum range and their direct bandgaps are also within this range, they may still work in thin-film solar cells. The larger direct bandgap provides a large absorption coefficient for thin-film solar photovoltaics, and the smaller indirect bandgap sets the open-circuit voltage of the cell. Table 6.6 includes four or five such binary semiconductors. Tungsten sulfide (WS_2) is on the borderline in terms of material abundance.

Let us further argue that among the binary semiconductors in Table 6.6, chalcogenides are most promising in producing low-cost solar cells, i.e. tin sulfide (SnS) and maybe WS_2. Among silicides, pnictides, and chalcogenides, the chemical bond in chalcogenides is the most ionic. The ionic bond allows chalcogenides to be synthesized into multicrystalline films by solution-based processes with excellent electrical properties, enabling low-cost high-efficiency solar cells as discussed in Sect. 3.1. Vacuum-based processes are often required for the synthesis of silicides, nitrides, and phosphides.

Besides the known binary semiconductors in Table 6.6, there may be new binary semiconductors out of Table 6.5 which meet all the requirements for terawatt solar photovoltaics. One example is copper sulfide (Cu_xS). When $x = 1.75$, the orthorhombic $Cu_{1.75}S$ is a thermodynamically stable phase with a direct bandgap of about 1.4 eV, as predicted by a first-principles study [18].

The candidates in binary semiconductors for a new terawatt-scale solar cell technology are limited, especially if we focus on solution-synthesizable chalcogenides. This fact has motivated efforts to find a ternary semiconductor, preferably a ternary chalcogenide, for terawatt solar photovoltaics. There are two generic approaches to a ternary semiconductor out of Table 6.5. One is to mix two metals (cations) into a silicide, pnictide, or preferably chalcogenide. The other is to mix two anions with a metal. Let us take pyrite (FeS_2) as an example, which has an indirect bandgap of 0.95 eV and a direct bandgap of 1.3 eV [17]. Two first-principles studies have been published recently, examining the bandgaps of ternary semiconductors based on FeS_2. Mixing an Earth-abundant metal in Table 6.5 into FeS_2 fails to produce a desired bandgap increase in FeS_2 [19]. Mixing FeS_2 with oxygen results in an indirect bandgap of 1.2–1.3 eV when 10 % of the sulfur atoms are replaced by oxygen [20], i.e. $FeS_{2-0.2}O_{0.2}$. None of these ternary semiconductors has the desired direct bandgap of 1.1–1.5 eV.

The author and his collaborators recently published their first-principles study on sulfurized hematite and proposed the first ternary semiconductor with a suitable direct bandgap for terawatt solar photovoltaics [21]. The ternary semiconductor starts with binary hematite (α-Fe_2O_3), which has an indirect bandgap of about 2.1 eV. When about 5.6 % of the oxygen atoms are replaced by sulfur, i.e. α-$Fe_2O_{3-0.167}S_{0.167}$, the bandgap becomes 1.45 eV direct, which is ideal for maximum efficiency. This is quite interesting as both α-Fe_2O_3 and FeS_2 have indirect bandgaps of 2.1 and 0.95 eV, respectively. Figure 6.6a illustrates the calculated bandgap as a function of sulfur concentration x in α-$Fe_2O_{3-x}S_x$. For $x = 0.167$, the corresponding bandgap is about 1.45 eV. Figure 6.6b shows the band structure for α-$Fe_2O_{3-0.167}S_{0.167}$, in which the maximum of the valence band coincides with the minimum of the conduction band, i.e. the bandgap is direct.

This concept of metal oxysulfide can be applied to other Earth-abundant metals. For example, the bandgap of cuprous oxide (Cu_2O) is 2.0 eV direct and that of cuprous sulfide (Cu_2S) is 1.2 eV indirect. By mixing Cu_2O and Cu_2S in proper ratios, bandgaps between 1.1 and 1.5 eV are achievable. If one of those bandgaps is direct, copper oxysulfide ($Cu_2O_{1-x}S_x$) becomes a semiconductor of interest for terawatt solar photovoltaics. A recent report investigated $Cu_2O_{1-x}S_x$ [22], although

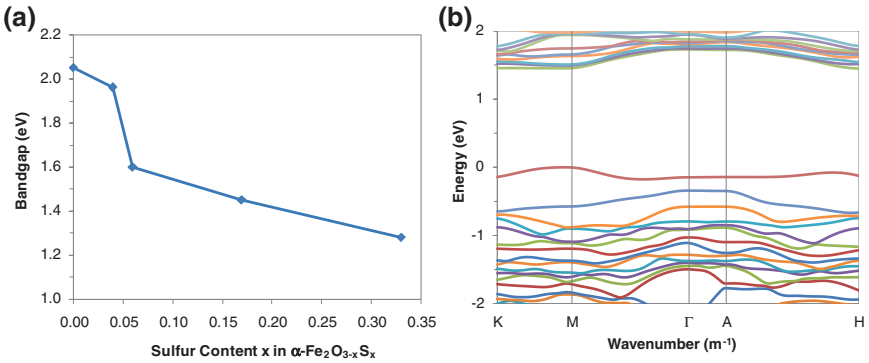

Fig. 6.6 First-principles study of α-$Fe_2O_{3-x}S_x$ [21]. **a** Calculated bandgap as a function of sulfur concentration x in α-$Fe_2O_{3-x}S_x$. At x = 0.167, the bandgap is about 1.45 eV. **b** Band structure for α-$Fe_2O_{3-0.167}S_{0.167}$. The maximum of the valence band is set at energy zero. The direct bandgap is at point M

it did not specify whether the bandgap is direct or indirect. Bandgap engineering in TiO_2 by mixing it with sulfur has also been reported [23], as the bandgap of TiO_2 is 3.3 eV direct and that of titanium disulfide (TiS_2) is 0.3 eV indirect.

Cost-effective doping techniques are likely needed for the Earth-abundant semiconductor absorber. If a p-n junction is employed in this semiconductor for charge separation, it requires both n-type and p-type of either this semiconductor or this semiconductor and another Earth-abundant semiconductor. Doping is also required to achieve an optimum resistivity in the semiconductor absorber for maximum efficiency. It is preferable to have the semiconductor absorber synthesized from solution, and doping could be incorporated into the solution-based synthesis process. In addition, all other materials in this new solar cell technology have to be Earth-abundant as well, i.e. they have to come out of Table 6.5. Other materials in thin-film solar cells include transparent conducting oxides and metallic electrodes. Some of the candidates for transparent conducting oxides are ZnO and TiO_2. Some of the candidates for metallic electrodes are Al and Ni.

6.3 Terawatt-Scale Storage of Solar Electricity

Storage of solar electricity is a cross-cutting roadblock for any cell technology. Without storage, the scale of grid-connected solar photovoltaics will likely be capped below 5 TW_p as estimated in Sect. 5.5.1. The amount of solar electricity for storage depends on our energy mix. For 30 % contribution from solar photovoltaics to our current global energy demand, the storage required is over 7×10^{10} kWh on a daily basis. This is equivalent to about 5 TW power output from storage for about 13 h a day. These numbers will likely go up multiple times, driven by factors such as increased global energy demands, unsuccessful solar-to-chemical conversion technologies, or local and global weather conditions.

For grid-connected solar photovoltaics, the storage takes in electricity from solar modules and outputs electricity to the grid, i.e. "electricity-in and electricity-out". The storage options for grid-connected solar photovoltaics were discussed in Sect. 5.5.1 [24], and the conclusion was that the capacity of each individual storage system on the grid has to be on the order of gigawatt. The storage technologies which have the potential to reach gigawatt scales include pumped hydropower, compressed air, and maybe batteries employing Earth-abundant materials. However, pumped hydropower and compressed air are limited by geological conditions.

It is important to remember that solar photovoltaics does not have be connected to the grid, i.e. they can be standalone or local-grid energy sources. In the U.S., electricity accounts for about 37 % of the energy consumption, out of which about 32 % comes from fossil fuels or nuclear power [25]. The remaining 5 % comes from hydropower, which is unlikely to be replaced by solar electricity. If the contribution from solar photovoltaics exceeds 32 % of our energy consumption, the excess solar electricity will have to be taken off the grid and converted into another form of energy. Failure to do so would cap the contribution from solar photovoltaics to 32 % of our energy consumption. In such cases, off-grid storage is required which takes into electricity and outputs fuel or heat, i.e. "electricity-in and something-else-out".

Off-grid storage takes in electricity and can output either fuel or heat, which opens up more possibilities for creative ideas. Fuel is a better option in general, as heat is more difficult to store and transport. There are different types of fuel the off-grid storage can produce. The fuel can be traditional, i.e. a hydrocarbon liquid which combusts with oxygen. The carbon in the fuel has to come from atmospheric CO_2. When the fuel burns, it releases CO_2 back into the atmosphere. This would provide a closed thus sustainable loop for carbon with zero net CO_2 emission. If the carbon is from fossil fuels, this fuel-producing process would not be sustainable. If the carbon comes from biomass, this planet would not be able to produce enough biomass for the demands [26]. Hydrogen is another possibility, which can be produced from water. If direct solar water splitting [27] does not work out, electrolysis of water [28], powered by solar electricity, is available. In a fuel cell, hydrogen recombines with oxygen to form water while generating electricity. Here hydrogen is the energy storage medium, which is in a closed loop with no CO_2 emission at all. Some of the difficulties with hydrogen include the risk of detonation when hydrogen is mixed with air. This risk adds restrictions to the transportation of hydrogen as a traffic accident may result in an explosion. It may also restrict hydrogen as a fuel in vehicles.

The fuel from off-grid storage does not have to be liquid or gaseous. It can be solid, but has to be Earth-abundant. Many metals in Table 6.5 are suitable as solid fuels, in addition to carbon and silicon. Solid carbon as a fuel is in line with the human history, in which biomass was the primary fuel for hundreds of thousands of years. The difference now is that the solid carbon as a fuel has to come primarily from atmospheric CO_2. This would make a closed loop for carbon with zero net CO_2 emission.

Metals can react with oxygen in the air to form oxides, in which energy is released. Combustion of a metal is difficult to handle as it involves extremely high temperatures above 2,000 °C. A safer and generic approach to release the energy

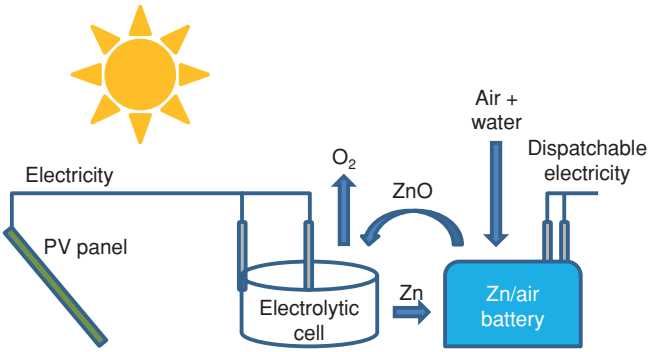

Fig. 6.7 A proposed Zn-ZnO cycle for storage of solar electricity. Zn rods are produced from ZnO through electrolysis powered by solar electricity. They are inserted into Zn-air batteries as the anode to generate electricity. The byproduct of the Zn-air battery, ZnO, is removed from the battery and transported back to Zn producers for recycling

stored in a metal is a metal-air battery, in which the metal reacts with oxygen in an aqueous electrolyte to become an oxide or hydroxide. Several metal-air batteries are under development, and Zn-air batteries are commercially available now. For a closed loop, the metal oxide or hydroxide has to be reduced back to pure metal by solar energy. Many metal oxides can be reduced to pure metals by electrolysis, and this is where solar electricity can be stored into a metal. For example, electrolytic production of Zn from ZnO is an industrial process, accounting for about 90 % of the Zn produced today at about 11,000,000 metric tons each year. Many metal hydroxides can be calcined to oxides at moderate temperatures for electrolysis.

One such closed energy loop for a Zn-ZnO cycle is illustrated in Fig. 6.7. Zn rods are produced from ZnO through electrolysis powered by solar electricity. They are transported to customers at different locations and inserted into Zn-air batteries as the anode to generate electricity. It is reminded that the Zn-air battery is recharged by replacing the Zn anode, not by providing electricity to the battery as in today's rechargeable batteries. The byproduct of the Zn-air battery, ZnO, is removed from the battery and transported back to Zn producers for recycling. This cycle is sustainable with no CO_2 emission and is in principle applicable to many other metals in Table 6.5.

There are 15 or so metals in Table 6.5 which can in principle serve as fuels in closed loops as illustrated in Fig. 6.7. A question comes up naturally, i.e. which metal has the best performance? By performance we mean that for a given amount of solar electricity we put in to produce a metal, how much energy can it release when it oxidizes? Table 6.7 lists Gibbs energies of formation for metal oxides [7], which are the maximum possible amounts of energy to be released when metals oxidize:

$$aM(s) + bO_2(g) \rightarrow M_aO_{2b}(s)$$

where M is a metal, and a and b account for the stoichiometry of its oxide. All the formation energies in Table 6.7 are negative, i.e. they all release energy when the metals oxidize. CO_2 and water (H_2O) are included in Table 6.7 as references. On

Table 6.7 Gibbs energies of formation for Earth-abundant metal oxides in Table 6.5. A figure of merit (FoM) is calculated for metals as solid fuels

Oxide	ΔG (kJ/mol)	Charge for reduction (C/mol)	FoM (J/C)	Redox pair	Standard reduction potential (V)
CO_2(g)	−394.4	385,940	1.02	C^{4+}/C	
H_2O(l)	−237.1	192,970	1.23	$H_2O/2OH^-$	−0.8277
CaO	*−603.3*	*192,970*	*3.13*	*Ca^{2+}/Ca*	*−2.868*
MgO	*−569.3*	*192,970*	*2.95*	*Mg^{2+}/Mg*	*−2.372*
SrO	*−561.9*	*192,970*	*2.91*	*Sr^{2+}/Sr*	*−2.899*
Al_2O_3	*−1,582.3*	*578,910*	*2.73*	*Al^{3+}/Al*	*−1.676*
ZrO_2	*−1,042.8*	*385,940*	*2.70*	*Zr^{4+}/Zr*	*−1.45*
BaO	*−520.3*	*192,970*	*2.70*	*Ba^{2+}/Ba*	*−2.912*
Ti_3O_5	*−2,317.4*	*964,850*	*2.40*	*Ti^{2+}/Ti*	*−1.628*
TiO_2	−888.8	385,940	2.30	Ti^{4+}/Ti	
SiO_2	−856.3	385,940	2.22	Si^{4+}/Si	
B_2O_3	−1,194.3	578,910	2.06	B^{3+}/B	
MnO	*−362.9*	*192,970*	*1.88*	*Mn^{2+}/Mn*	*−1.185*
Cr_2O_3	−1,058.1	578,910	1.83	Cr^{3+}/Cr	−0.744
Mn_3O_4	−1,283.2	771,880	1.66		
ZnO	**−320.5**	**192,970**	**1.66**	**Zn^{2+}/Zn**	**−0.7618**
Mn_2O_3	−881.1	578,910	1.52	Mn^{3+}/Mn	
Fe_3O_4	−1,015.4	771,880	1.32	Fe^{2+}/Fe	−0.447
Fe_2O_3	−742.2	578,910	1.28	Fe^{3+}/Fe	−0.037
MnO_2	−465.1	385,940	1.21	Mn^{4+}/Mn	
CoO	−214.2	192,970	1.11	Co^{2+}/Co	−0.28
Co_3O_4	−774.0	771,880	1.00	Co^{3+}/Co	
PbO	−188.9	192,970	0.98	Pb^{2+}/Pb	−0.1262
Pb_3O_4	−601.2	771,880	0.78	Pb^{4+}/Pb	
Cu_2O	−146.0	192,970	0.76	Cu^{+}/Cu	0.521
CuO	−129.7	192,970	0.67	Cu^{2+}/Cu	0.3419
PbO_2	−217.3	385,940	0.56	Pb^{4+}/Pb	

Assumptive redox pairs for metal oxides and their corresponding standard reduction potentials [7] are included

the other hand, the amount of electrical charge required to reduce 1 mol of a metal oxide to metal can be calculated from the stoichiometry of the oxide under the assumption of 100 % internal quantum efficiency, which is listed in column 3 of Table 6.7. The figure of merit for a metal as a fuel is thus defined as:

$$FoM(\mathrm{J/C}) = \frac{Gibbs\ Energy\ of\ Formation\ (\mathrm{J/mol})}{Minimum\ Charge\ for\ Reduction\ (\mathrm{C/mol})}$$

It indicates that for a fixed amount of charge supplied in electrolysis, how much energy the metal can release during oxidation, which is in column 4 of Table 6.7.

Carbon and hydrogen are not the best candidates in terms of their performance in the proposed energy loop. Many metals would have far better performance than carbon and hydrogen. Ca has the best figure of merit in Table 6.7, which is about a factor of three over carbon and hydrogen. The metals in italic type in Table 6.7 all

have good figures of merit. However, the italic metals have their standard reduction potentials more negative than that of H_2O [7]. The standard reduction potential for the following reaction is −0.8277 V versus the standard hydrogen electrode:

$$2H_2O(l) + 2e^- \rightarrow H_2(g) + 2OH^-(l)$$

This fact prevents electrolytic reduction of the italic metal oxides in aqueous electrolytes, as gaseous hydrogen would be produced instead of pure metals. In fact, many of the italic metals are produced from their oxides electrolytically in molten salts, which require high temperatures between 500 and 1,000 °C. For high-temperature electrolysis, either concentrated solar power or part of the electricity from solar modules has to be used to heat up the electrolytic cell, resulting in a more complicated, thus more costly, electrolytic system. We are in favor of room-temperature electrolysis for the closed energy loop in Fig. 6.7, which eliminates all the italic metals in Table 6.7.

For the following metal oxides in Table 6.7, TiO_2, SiO_2, B_2O_3, and Cr_2O_3, there are currently no industrial electrolytic processes to produce metals from these oxides. For the next metal oxide, Mn_3O_4, we are not aware of Mn-air batteries. Unless a practical Mn-air battery is developed, Mn does not make a closed energy loop and thus is unsustainable as a fuel.

Now we come down to Zn as the best-performance solid fuel, which is in bold type in Table 6.7. Most of the technologies required for the Zn-ZnO cycle are commercially available, including room-temperature electrolytic production of Zn from ZnO and Zn-air batteries, although the infrastructure for such an energy loop has yet to be established. The figure of merit for Zn, 1.66, is far better than carbon or hydrogen for the proposed energy loop. Zn rods are safe to store and transport to different locations. They would be inserted into Zn-air batteries to deliver electricity whenever needed. Through this Zn-ZnO loop, solar electricity would become dispatchable, meaning that it is delivered on demand.

References

1. U.S. Geological Survey (2013) Mineral commodity summaries. Available at http://minerals.usgs.gov/minerals/pubs/mcs/2013/mcs2013.pdf
2. Russell R, Tous L, Philipsen H, Horzel J, Cornagliotti E, Ngamo M, Choulat P, Labie R, Beckers J, Bertens J, Fujii M, John J, Poortmans J, Mertens R (2012) A simple copper metallization process for high cell efficiencies and reliable modules. In: Proceedings of the 27th European photovoltaic solar energy conference and exhibition, Frankfurt, pp 538–543
3. U.S. Geological Survey (2013) 2011 Minerals yearbook. Available at http://minerals.usgs.gov/minerals/pubs/commodity/myb/
4. Kessler M, Munster D, Neubert T, Mader CP, Schmidt J, Brendel R (2011) High-efficiency back-junction silicon solar cell with an in-line evaporated aluminum front grid. In: Conference record of the 37th IEEE photovoltaic specialists conference, Seattle, pp 1085–1090
5. Sarti D, Einhaus R (2002) Silicon feedstock for the multi-crystalline photovoltaic industry. Sol Energy Mater Sol Cells 72:27–40
6. Braga AFB, Moreira SP, Zampieri PR, Bacchin JMG, Mei PR (2008) New processes for the production of solar-grade polycrystalline silicon: a review. Sol Energy Mater Sol Cells 92:418–424

7. Haynes WM (2013) CRC handbook of chemistry and physics, 94th edn. CRC Press, Boca Raton
8. Monnier R, Giacometti JC (1964) Recherches sur le raffinage electrolytique du silicium. Helv Chim Acta 47:345–353
9. Cai J, Luo X-T, Haarberg GM, Kongstein OE, Wang S-L (2012) Electrorefining of metallurgical grade silicon in molten $CaCl_2$ based salts. J Electrochem Soc 159:D155–D158
10. Tao M (2013) Impurity segregation in electrochemical processes and its application to electrorefining of ultrapure silicon. Electrochim Acta 89:688–691
11. Fell A, Mayer K, Hopman S, Kray D (2009) Potential and limits of chemical enhanced deep cutting of silicon with a coupled laser-liquid jet. J Laser Appl 21:27–31
12. Bowden S, LeBeau J (2012) Laser wafering. In: Conference record of the 38th IEEE photovoltaic specialists conference, Austin, pp 1826–1829
13. Vallera AM, Alves JM, Serra JM, Brito MC, Gamboa RM (2007) Linear electric molten zone in semiconductors. Appl Phys Lett 90:232111-1-3
14. Fortunato E, Ginley D, Hosono H, Paine DC (2007) Transparent conducting oxides for photovoltaics. MRS Bull 32:242–247
15. Zhou B (2013) Codoped zinc oxide by a novel co-spray deposition technique for solar cell applications. PhD dissertation, Arizona State University
16. U.S. Geological Survey (2002) Rare earth elements—critical resources for high technology. Available at http://pubs.usgs.gov/fs/2002/fs087-02/
17. Alharbi F, Bass JD, Salhi A, Alyamani A, Kim H-C, Miller RD (2011) Abundant non-toxic materials for thin film solar cells: alternative to conventional materials. Renew Energy 36:2753–2758
18. Xu Q, Huang B, Zhao Y, Yan Y, Noufi R, Wei S-H (2012) Crystal and electronic structures of Cu_xS solar cell absorbers. Appl Phys Lett 100:061906-1-3
19. Sun R, Ceder G (2011) Feasibility of band gap engineering of pyrite FeS_2. Phys Rev B 84:245211-1-7
20. Hu J, Zhang Y, Law M, Wu R (2012) Increasing the band gap of iron pyrite by alloying with oxygen. J Am Chem Soc 134:13216–13219
21. Xia C, Jia Y, Tao M, Zhang Q (2013) Tuning the band gap of hematite α-Fe_2O_3 by sulfur doping. Phys Lett A 377:1943–1947
22. Meyer BK, Merita S, Polity A (2013) On the synthesis and properties of ternary copper oxide sulfides ($Cu_2O_{1-x}S_x$). Phys Status Solidi RRL 7:360–363
23. Umezawa N, Janotti A, Rinke P, Chikyow T, van de Walle CG (2008) Optimizing optical absorption of TiO_2 by alloying with TiS_2. Appl Phys Lett 92:041104-1-3
24. International Renewable Energy Agency (2012) Electricity storage—technology brief. Available at http://www.irena.org/DocumentDownloads/Publications/IRENA-ETSAP%20Tech%20Brief%20E18%20Electricity-Storage.pdf
25. U.S. Energy Information Administration (2011) Annual energy review. Available at http://www.eia.gov/totalenergy/data/annual/index.cfm
26. Lewis NS (2007) Powering the planet. MRS Bull 32:808–820
27. Fujishima A, Honda K (1972) Electrochemical photolysis of water at a semiconductor electrode. Nature 238:37–38
28. de Levie R (1999) The electrolysis of water. J Electroanal Chem 476:92–93

Chapter 7
Final Remarks

This book intends to provide a more comprehensive picture about solar photovoltaics. It includes the physics for solar photovoltaics and the manufacturing processes for wafer-Si solar cells and modules, although the discussions are a little superficial. The book also attempts to examine some of the long-term and big-picture issues with solar photovoltaics, beyond the widely-discussed topics of efficiency and cost. These issues include availability of raw materials, availability of electricity, storage of solar electricity, and recycling of solar modules. For wafer-Si solar cells and modules, the book breaks down the major contributors to the overall cost such as energy input, ingot wafering, Ag front electrode, and cell efficiency dispersion. It is important to remember that solutions for many of these issues, long-term or short-term, require major technological innovations.

Based on the quantitative analysis in the book, most of the current commercial solar cell technologies, wafer Si, CdTe, or CIGS, is incapable of reaching a terawatt scale without major technological breakthroughs. They suffer from natural resource limitations which are hard showstoppers. It is unlikely that CdTe and CIGS technologies will ever become a noticeable source of energy in our life, although they are, and will remain, commercially successful for decades to come. This is because the semiconductor absorber in these technologies contains elements which are extremely scarce on this planet. Although the semiconductor absorber in wafer-Si and thin-film Si technologies is Earth-abundant, these solar cells often require natural resources of limited supply in their structures or manufacturing processes, such as In, Ag, and electricity. It is important to remember that resource limitations are an inevitable aspect for solar photovoltaics, and quite possibly for many other renewable energy technologies, due to the scale required for any tangible impact.

The book points out three solar cell technologies which have the potential to reach terawatt scales. They are:

1. Wafer-Si solar cells;
2. Thin-film Si solar cells; and
3. Earth-abundant silicide, pnictide, or chalcogenide solar cells.

M. Tao, *Terawatt Solar Photovoltaics*, SpringerBriefs in Applied Sciences and Technology, DOI: 10.1007/978-1-4471-5643-7_7, © The Author(s) 2014

Two of them, wafer Si and thin-film Si, are current commercial technologies, but major modifications have to be made to their structures and/or manufacturing processes for them to reach terawatt scales. The third technology is a new cell technology which has yet to be developed. This new cell technology has to employ Earth-abundant materials throughout its structure, and its manufacturing processes have to be resource-efficient including electricity, water, and chemicals. The following is a summary of the strategic research directions, as concluded in this book, for the three cell technologies to achieve low cost, high efficiency, and most importantly, terawatt-scale deployment.

Wafer-Si solar cells dominate today's market with about 90 % of the market share. It may stay this way for the foreseeable future with its many advantages: high efficiency, mature technology, low entry barrier, relatively low cost, large market share, among others. The strategic research directions proposed in the book for terawatt-scale wafer-Si solar photovoltaics include:

1. Energy-efficient purification of metallurgical-grade Si for solar-grade Si;
2. Substitution of Ag front electrode with Cu or Al;
3. Kerfless and fast cutting of Si ingots for wafers;
4. Recycling of Si, Ag, and Cu from end-of-life modules;
5. Cell and module efficiency uniformization during manufacturing;
6. Improvement of module degradation and lifetime; and
7. Terawatt-scale storage of solar electricity.

The future of thin-film Si solar cells is less certain. It is currently losing its market share due to its low efficiency and high cost. If wafer-Si solar cells do not reach a terawatt scale, thin-film Si is currently the only technology capable of terawatt-scale deployment. The proposed strategic research directions for terawatt-scale thin-film Si solar photovoltaics include:

1. Reduction of manufacturing costs through solution-based fabrication processes;
2. Improvement of cell efficiency;
3. Recycling of end-of-life cells and modules;
4. Improvement of cell and module lifetime; and
5. Terawatt-scale storage of solar electricity.

If neither wafer-Si nor thin-film Si works out, a new solar cell technology has to be developed with only Earth-abundant materials throughout its structure. It is unclear what material system this new cell technology will be based on or if the device physics in the new cell technology will be similar to today's commercial cell technologies, i.e. an inorganic semiconductor for light absorption and a p-n junction for charge separation. Nevertheless, this book suggests a few strategic research directions for the new cell technology if it is similar to today's commercial cell technologies:

1. Development of an Earth-abundant binary or ternary semiconductor with a 1.1–1.5 eV direct bandgap as the absorber;
2. Development of solution-based synthesis and doping techniques for the absorber;

3. Development of an Earth-abundant transparent conducting oxide including its synthesis and doping techniques;
4. Identification of a metal or metals as the electrodes and development of cost-effective metallization processes;
5. Improvement of cell efficiency;
6. Recycling of end-of-life cells and modules;
7. Improvement of cell and module lifetime; and
8. Terawatt-scale storage of solar electricity.

There are multiple technical approaches we can envision for each of the research directions listed above. The book presents, based on the best judgment of the author, several technical approaches for some of these research directions. With the limited knowledge and experience of the author, the proposed technical approaches are inclined towards terawatt-scale wafer-Si solar photovoltaics and post-Si thin-film solar photovoltaics. All the proposed technical approaches are based on similar device physics to today's commercial solar cell technologies. It is quite possible that new device physics may prevail in future solar cell technologies. New device physics, such as those "third-generation concepts" [1], opens up so many possibilities for innovative ideas potentially leading to quantum leaps in solar photovoltaics. However, it becomes practically impossible to predict the future of new physics based solar photovoltaics as there are so many uncertainties at this time for new solar photovoltaic physics. One thing clear from this book is that any new solar photovoltaic physics will have to employ Earth-abundant materials and be resource-efficient, or it will not make a real impact.

Terawatt-scale storage of solar electricity is a cross-cutting issue which enables any terawatt-capable solar cell technology to actually reach a terawatt scale. Storage of solar electricity can be grid-connected or off-grid. Off-grid storage allows solar photovoltaics to become the main source of energy in our life, exceeding 30 % of our future energy demands. The significance of off-grid storage shall become obvious if none of the alternative technologies for solar energy utilization, such as solar-to-chemical conversion or concentrated solar power, reaches a terawatt scale. The book proposes a closed energy loop based a metal–metal oxide cycle for off-grid storage. The metal generates electricity in a metal-air battery and converts itself to an oxide. The metal oxide is electrolytically reduced to metal through solar electricity. A Zn–ZnO cycle is suggested for this energy loop due to its potential performance, process simplicity, and technical readiness.

Reference

1. Conibeer G (2007) Third-generation photovoltaics. Mater Today 10:42–50

Index

M. Tao, *Terawatt Solar Photovoltaics*, SpringerBriefs in Applied Sciences and Technology, DOI: 10.1007/978-1-4471-5643-7, © The Author(s) 2014